“Variation of stable silicon isotopes: Analytical developments and applications in Precambrian geochemistry”

Dissertation
zur Erlangung des Grades

“Doktor
der Naturwissenschaften”

am Fachbereich Chemie, Pharmazie und Geowissenschaften
der Johannes Gutenberg-Universität
in Mainz

Kathrin Abraham
geb.: 23.05.1980 in Nürnberg

Mainz den, 30.03.2010

Dekan:

1. Berichterstatter:

2. Berichterstatter:

Tag der mündlichen Prüfung: 28.05.2010

Preface

This doctoral thesis was performed as cooperation between the University of Mainz and the Royal Museum for Central Africa, Belgium.

Section I: Introduction

Section II: $\delta^{30}Si$ and $\delta^{29}Si$ Determinations on USGS BHVO-1 and BHVO-2 Reference Materials with a New Configuration on a Nu Plasma Multi-Collector ICP-MS

(Kathrin Abraham, Sophie Opfergelt, François Fripiat, Anne-Julie Cavagna, Jeroen T.M. de Jong., Stephen F. Foley, Luc André and Damien Cardinal)

Geostandards and Geoanalytical Research, 2008.

Section III: Coupled silicon-oxygen isotopic evidences for the origin of silicification in mafic volcanic rocks of the Barberton Greenstone Belt, South Africa

(Kathrin Abraham, Axel Hofmann, Stephen F. Foley, Damien Cardinal, Chris Harris, Matthias Barth, Luc André)

Submitted to Earth and Planetary Science Letters.

Section IV: Potential changes in the source of Granitoids in the Archaean: the Si isotope perspective

(Kathrin Abraham, Axel Hofmann, Stephen F. Foley, Damien Cardinal, Luc André)

Submitted as extended Abstract, 5th International Archaean Symposium.

In all cases, sample preparation, isotope (except of oxygen), trace element and further analytical work, data evaluation and interpretation as well as writing of the manuscripts were performed by the first author. Besides publications in peer-reviewed journals, results of the thesis were presented talks and poster presentations at several international conferences and workshops (Related publications).

Summary

The work presented in this thesis predominantly deals with bulk-rock measurements of silicon stable isotopes on a Multi Collector-ICP-MS. Analyses were performed in cooperation with the Royal Museum for Central Africa, Belgium. In addition to measurements on analytical rock standards, silicon isotopes were used as geochemical constraints on mechanisms of silicification (a prevalent process of silica-enrichment on the Precambrian seafloor) and on the petrogenesis of granitoids within the Archaean 3.55 to 3.22 Ga Barberton Granite Greenstone Terrain (BGGT) in South Africa. The PhD-thesis also presents standard geochemical element analyses, including X-ray fluorescence (major elements) and laser ablation-ICP-MS (trace elements), both measured at the Institute of Geosciences, University of Mainz, Germany.

The PhD-thesis is subdivided into four major sections. **Section I** gives a general introduction, including the variability of silicon isotope values exhibited by terrestrial rocks, the general geology of the BGGT and the silicon isotope analysis procedure. **Section II** focuses on the development on a new method for Si isotope analysis and on the determination of silicon isotope values in basalt standards. **Section III** uses coupled silicon/oxygen isotopes to investigate the mechanisms controlling Archaean silicification. **Section IV** characterizes the changes of Archaean granitoids though time in the light of silicon isotopes.

Section I: Introduction

Section I addresses the basic concepts of stable isotope variations for the general reader. In addition, it describes in detail the geology of the study area and familiarizes to the process of Precambrian silica formation. Furthermore, it is intended to provide an introduction to the analytical methods and the geochemistry of silicon isotopes as a non-traditional stable isotope system.

Section II: $\delta^{30}Si$ and $\delta^{29}Si$ Determinations on USGS BHVO-1 and BHVO-2 Reference Materials with a New Configuration on a Nu Plasma™ Multi-Collector ICP-MS

The first objective of this section describes how the first analysis of $\delta^{30}Si$ on a conventional Nu Plasma™ Multi-Collector ICP-MS instrument can be enabled by the elimination of $^{14}N^{16}O$ interference overlying the ^{30}Si peak. The determination of $\delta^{30}Si$ was rendered possible owing to new instrumental upgrades that facilitate the application of a higher mass resolution.

The careful characterisation of appropriate reference materials is indispensable for the assessment of the accuracy of a measurement. The determination of U.S. Geological Survey (USGS) reference materials represents the second objective of this section. The analysis of two Hawaiian standards (BHVO-1 and BHVO-2) demonstrates precise and accurate $\delta^{30}Si$ determinations and provides cross-calibration data as a quality control for other laboratories.

Section III: Coupled silicon-oxygen isotopic evidences for the origin of silicification in mafic volcanic rocks of the Barberton Greenstone Belt, South Africa

In contrast to the modern Earth, silicification of near-surface layers, including chert formation, were widespread processes on the Precambrian ocean floor, and demonstrate the ubiquity of extreme silica mobilization in the early Earth. Section III outlines the investigation of silicon and oxygen isotopes on three different stratigraphic sections of variably silicified basalts and overlying bedded cherts from the 3.54 Ga, 3.45 Ga and 3.33 Ga Theespruit, Kromberg and Hooggenoeg Formations, respectively. Silicon isotopes, oxygen isotopes and the variable SiO_2-contents demonstrate a positive correlation with silicification intensity in all three sections, with varying gradients of $\delta^{30}Si$ vs. $\delta^{18}O$ arrays for different sections.

Seawater has been regarded as the most likely source of silica for the silicification process. Calculations show that classical water-rock interaction can not influence the silicon isotope variation due to the very low concentration of Si in seawater (49 ppm). The data are consistent with a two end-member component mixture between basalt and chert. Our data confirm a secular increase in chert isotope composition. Possible factors that could account for different gradients of $\delta^{30}Si$ vs. $\delta^{18}O$ are changes of seawater isotope signature, the water temperature or secondary alteration.

Section IV: Potential changes in the source of Granitoids in the Archaean: the Si isotope perspective

Sodic tonalite-trondhjemite-granodiorite (TTG) intrusive units make up large components of the Archaean crust. In contrast, today's continental crust is more potassic in composition (GMS group: granite-monzonite-syenite). Processes that lead to this changeover from "sodic" to "potassic" crust are the subject of Section IV.

Silicon isotope measurements were combined with major and trace element analyses on different generations of TTG and GMS group intrusive units from 3.55 to 3.10 Ga from the study area. $\delta^{30}Si$-values show a slight temporal increase during different pluton generations, with sodic intrusive units demonstrating the lowest Si-isotope composition.

The small increase in silicon isotope composition with time might be due to different temperature conditions in the source of granitoids, with Na-rich, light $\delta^{30}Si$ granitoids emerging at higher temperatures. A similarity in $\delta^{30}Si$ between Archaean K-rich plutons and Phanerozoic K-rich plutons is confirmed.

Zusammenfassung

Die vorliegende Dissertation behandelt die Gesamtgesteinsanalyse stabiler Siliziumisotope mit Hilfe einer „Multi Collector-ICP-MS". Die Analysen fanden in Kooperation mit dem „Royal Museum for Central Africa" in Belgien statt. Neben der Charakterisierung von Gesteinstandards, wurden die Siliziumisotope verwendet, um die Mechanismen

der Silizifizierung (ein häufiger Prozess der Siliziumanreicherung am Präkambrischen Ozeanboden) und die Granitoidpetrogenese an Gesteinen des Archaischen, 3.55 bis 3.22 Milliarden Jahre alten „Barberton Granite Greenstone Terrain“ (BGGT) in Südafrika geochemisch nachzuvollziehen. Die Dissertation befasst sich zudem mit Standardprozeduren der geochemischen Analyse, namentlich Röntgenfluoreszenzanalyse (Hauptelemente) und Laser Ablations ICP-MS (Spurenelemente), beide durchgeführt am Institut für Geowissenschaften in Mainz, Deutschland.

Die Dissertation ist unterteilt in vier Kapitel. **Kapitel I** stellt eine generelle Einführung dar, welche die Siliziumisotopenverteilung an terrestrischen Gesteinen, eine Beschreibung der Geologie des BGGT und das Verfahren der Siliziumisotopenanalyse beinhaltet. **Kapitel II** erörtert die Entwicklung einer neuen Methode zur Siliziumisotopenanalyse und die Bestimmung der Siliziumisotopie an Basaltstandards **Kapitel III** befasst sich mit kombinierter Sauerstoff-/Silizium- Isotopenanalyse, um die Mechanismen der Silizifizierung im Archaikum zu untersuchen. **Kapitel IV** charakterisiert anhand der Siliziumisotopie die zeitliche Veränderung Archaischer Granitoide.

Kapitel I: Einführung

Kapitel I behandelt die Grundprinzipien der stabilen Isotopenvariation. Des Weiteren, soll dieses Kapitel eine Einführung in die Analysemethoden und die Geochemie der Siliziumisotope als ein nicht traditionelles stabiles Isotopensystem geben. Ferner beschreibt es die Geologie des Arbeitsgebietes im Detail und macht den Leser mit dem Prozess der präkambrischen Siliziumbildung vertraut.

Kapitel II: Bestimmung von δ^{30}Si und δ^{29}Si an USGS BHVO-1 und BHVO-2 Referenzmaterialien mit einer neuen Konfiguration an einer Nu Plasma™ „Multi-Collector ICP-MS“.

Einer der Schwerpunkte dieses Kapitels beschreibt die erstmalige Analyse des δ^{30}Si –Wertes an einem konventionellen Nu Plasma™ „Multi-Collector ICP-MS“ Instrument, durch die Eliminierung der den ^{30}Si “peak” überlagernden $^{14}N^{16}O$ Interferenz. Die Analyse von δ^{30}Si wurde durch technische Modifikationen der Anlage erreicht, welche eine höherer Massenauflösung ermöglichten.

Die sorgsame Charakterisierung eines adäquaten Referenzmaterials ist unabdingbar für die Abschätzung der Genauigkeit einer Messung. Die Bestimmung der „U.S. Geological Survey“ Referenzmaterialien bildet den zweiten Schwerpunkt dieses Kapitales. Die Analyse zweier hawaiianischer Standards (BHVO-1 and BHVO-2), belegt die präzise und genaue δ^{30}Si Bestimmung und bietet Vergleichsdaten als Qualitätskontrolle für andere Labore.

Kapitel II: Kombinierte Silizium-/Sauerstoffisotope zur Untersuchung der Entstehung der Silizifizierung vulkanischer Gesteine des „Barberton Greenstone Belt", Südafrika.
Im Gegensatz zu heute, war die Silizifizierung der Oberflächennahen Schichten, einschließlich der „Chert" Bildung, weitverbreitete Prozesse am präkambrischen Ozeanboden. Diese Horizonte sind Zeugen einer extremen Siliziummobilisierung in der Frühzeit der Erde. **Kapitel II** behandelt die Analyse von Silizium- und Sauerstoffisotopen an drei unterschiedlichen Gesteinsprofilen mit unterschiedlich stark silizifizierten Basalten und überlagernden geschichteten „Cherts" der 3.54, 3.45 und 3.33 Mill. Jr. alten Theespruit, Kromberg und Hooggenoeg Formationen. Siliziumisotope, Sauerstoffisotope und die SiO_2-Gehalte demonstrieren in allen drei Gesteinsprofilen eine positive Korrelation mit dem Silizifizierungsgrad, jedoch mit unterschiedlichen Steigungen der $\delta^{30}Si$-$\delta^{18}O$ -Verhältnisse.

Meerwasser wird als Quelle des Siliziums für den Silizifizierungsprozess betrachtet. Berechnungen haben gezeigt, dass eine klassische Wasser-Gestein Wechselwirkung die Siliziumisotopenvariation nicht beeinflussen kann, da die Konzentration von Si im Meerwasser zu gering ist (49 ppm). Die Daten stimmen mit einer Zwei-Endglieder-Komponentenmischung überein, mit Basalt und „Chert" als jeweilige Endglieder. Unsere gegenwärtigen Daten an den „Cherts" bestätigen einen Anstieg der Isotopenzusammensetzung über der Zeit. Mögliche Faktoren, die für unterschiedliche Steigungen der $\delta^{30}Si$-$\delta^{18}O$ Verhältnisse verantwortlich sein könnten sind Veränderungen in der Meerwasserisotopie, der Wassertemperatur oder sekundäre Alterationseffekte.

Kapitel IV: Potentielle Variationen in der Quellregion archaischer Granitoide: die Si-Isotopen Perspektive.
Natriumhaltige Tonalit-Trondhjemit-Granodiorit (TTG) Intrusiva repräsentieren große Anteile der archaischen Kruste. Im Gegensatz dazu ist die heutige Kruste kaliumhaltiger (GMS-Gruppe: Granit-Monzonite-Syenite). Prozesse, die zu dem Wechsel von natriumhaltiger zu kaliumhaltiger Kruste führten sind die Thematik des **Kapitels IV.**

Siliziumisotopenmessungen wurden hier kombiniert mit Haupt- und Spurenelementanalysen an unterschiedlichen Generationen der 3.55 bis 3.10 Mill. Yr. alten TTG und GMS Intrusiva aus dem Arbeitsgebiet. Die $\delta^{30}Si$-Werte in den unterschiedlichen Plutonit Generationen zeigen einen leichten Anstieg der Isotopie mit der Zeit, wobei natriumhaltige Intrusiva die niedrigste Si-Isotopenzusammensetzung aufweisen.

Der leichte Anstieg in der Siliziumisotopenzusammensetzung über die Zeit könnte auf unterschiedliche Temperaturbedingungen in der Quellregion der Granitoide hinweisen. Die Entstehung von Na-reichen, leichten $\delta^{30}Si$ Granitoiden würde demnach bei höheren Temperaturen erfolgen. Die Ähnlichkeit der $\delta^{30}Si$-Werte in archaischen K-reichen Plutoniten und phanerozoischen K-reichen Plutoniten wird ebenfalls deutlich.

Contents

Section I

Introduction

Chapter 1

1. General overview

This chapter summarizes the principles of isotope fractionation and the terrestrial variation of silicon and oxygen isotopes.

1.1. The superficial silica cycle

Silicon (Si) belongs to the third period and the fourth family of the periodic table. It is not found in its atomic state on Earth, but rather in combination with oxygen as a silicate ion (SiO_4). Si has only one valence (4+, tetravalent).

Silicon is the second most abundant element (after oxygen) in the Earth's crust, making up 27 % of the lithosphere by mass. It is a major constituent of rocks (igneous, sedimentary rocks and soils) given that the vast majority of the common rock forming minerals are silicates. Furthermore Si biomineralized into amorphous silica in plants and silica-secreting organisms: e.g. marine diatoms contributed to 45 % of total Phanerozoic marine primary production. The exposing of the rocks to the hydro- and atmosphere represents an interface to the whole Earth´s surface environment. Weathering of primary silicate minerals accounts for 45 % of the total content of dissolved major and minor elements in river water (Stumm and Wollast, 1990). Furthermore, dissolved silicon fluxes from rivers constitutes 85 % of the Si supply to the oceans (Treguer et al., 1995).

Due to the chemical similarity of Si and C (both having four bonding electrons), the global Si cycle is closely related to the C cycle and therefore of fundamental interest for climate, as Si regulates the atmospheric greenhouse gas CO_2, through the consumption by a combined silicate weathering and carbonate precipitation (Berner, 1997). However, silicon is less reactive than carbon and the cycle of silicon differs from the cycles of carbon, nitrogen and sulphur in that, for instance, silicon does not have a gaseous phase.

The Precambrian geochemical silica cycle is only poorly investigated (Siever, 1992; Perry and Lefticariu, 2003; Maliva et al., 2005). However, the Precambrian ocean differs from the Phanerozoic in that the devoid of silica-secreting organisms (for example, diatoms, radiolarians) leads to silica saturation. Precambrian seawater Si contents range between 60 and 120 ppm (e.g. Siever, 1992; Morris, 1993), as a function of temperature and pH. This implicates a residence time of 105 years in the Precambrian ocean. In contrast, the Si precipitation by diatoms leads to very low Si concentrations in the modern ocean of 1 ppm or less (e.g. Siever, 1992; Perry and Lefticariu, 2003) with longer residence times of ~1.5 kyr.

1.2. Theory of stable isotope geochemistry

1.2.1. Stable isotopes

Isotopes of an element differ by reason of divergent number of neutrons (*n*) and same number of protons (*z*) and electrons (*e*) in their mass numbers (*m*). Stable isotopes experienced neither a radioactive decay nor a radiogenic growth. There are eighty-three naturally occurring elements that are not radioactive or that yield half lives long enough to be considered stable; thereof three-quarters have two or more isotopes. The number of stable isotopes for the naturally occurring elements tends to increase with increasing atomic number. E.g. elements yielding a low atomic number like H or C have low numbers of stable isotopes (in this case only two), contrary Sn with a high atomic number of 79 has 10 isotopes.

For light elements, most of isotopic data are reported in "delta notation", where the isotopic composition is cast as the deviation (in parts per thousand or "per mil") of an isotopic ratio relative to the same ratio in a standard:

$$\delta = ((R_{sample}/R_{standard})-1)*1000$$

Whereby R denotes the ratio of the heavy (generally rare) over the light (generally more abundant) isotope. In the case of Silicon isotopes: Si has three stable isotopes: ^{28}Si, ^{29}Si and ^{30}Si with the relative abundances of 92.23 %, 4.67 % and 3.10 %, respectively (Faure and Mensing, 2005), R is denoted as $^{30}Si/^{28}Si$ and thus the delta value is described as $\delta^{30}Si$. This leads to a consistent nomenclature, where the positive delta value ($\delta>0$ corresponds to a relative enrichment in the heavy isotope in comparison to the reference standard (heavier signature, higher $^{30}Si/^{28}Si$), while a negative delta value ($\delta<0$) means a depletion in heavy isotope compared to the reference material (lighter signature, lower $^{30}Si/^{28}Si$). Commonly the units for δ are noted using the per mil sign (‰).

Because of their mass differences, stable isotopes react unequally to physical, chemical or biological processes. Thereby the variations in the relative quantities of heavy or light isotopes provide the foundation for the field of stable isotope geochemistry. Every isotope is characterized by its own vibration energy and capacity of movement depending on its mass: lighter isotopes and molecules containing light isotopes of one element react faster then heavy isotopes or isotopically heavy molecules. As a result of this difference in mass-dependent behaviour during physicochemical processes, *isotope fractionation* arises.

The isotope fractionation between two phases and temperature (T) is described by a simple relation:

$$1000 \ln \alpha = A / T^2 + B$$

The fractionation factor, α, is the ratio of isotope ratios in two phases:

$$\alpha_{A-B} = \frac{R_A}{R_B} = \frac{10^{-3}\delta_A + 1}{10^{-3}\delta_B + 1}, (A, B = components)$$

Logarithmized it can be converted into:

$$\ln \alpha_{A-B} = \ln(10^{-3}\delta_A + 1) - \ln(10^{-3}\delta_B + 1)$$

For δ-values smaller than 10‰ an approximation can be written:

$$\ln(10^{-3}\delta + 1) \approx 10^{-3}\delta$$

Consequently it results that for e.g.: δ= 10‰:

$$\ln(10^{-3} * 10 + 1) = \ln(1.010) = 0.00995 \approx 0.010$$

Therefore this may be written as:

$$\ln \alpha_{A-B} \approx 10^{-3}(\delta_A - \delta_B)$$

The isotope fractionation between two phases is often reported as:

$$\Delta_{A-B} = \delta_A - \delta_B$$

Therefore:

$$\Delta_{A-B} = \delta_A - \delta_B \approx 1000 \ln \alpha_{A-B} = \frac{A}{T^2} + B$$

This can be converted to T:

$$T = \sqrt{A/(\Delta_{A-B} - B)}$$

In general, there are two main types of isotope fractionation: (i) equilibrium and (ii) kinetic isotope fractionation (Young et al., 2002).

1.2.2. Equilibrium fractionation

Equilibrium fractionation describes a fractionation, whereby the reacting phases are maintained in equilibrium and the reaction runs in two directions (bi-directional). Equilibrium fractionation is denoted as a quantum-mechanical phenomenon, mainly driven by vibrational motions of the molecules, depending on the bond-strength of the atomic mass. Considering a diatomic gas molecule, the zero-point energies differ for variable atom masses, as do the vibration energies, being lower for heavier isotopes. For this reason, a higher energy is needed to dissociate the heavy molecules.

There are a number of factors controlling the sign and magnitude of isotopic exchange at equilibrium. Qualitative rules for the equilibrium fractionation are given by O´Neil (1986) and Schauble (2004):

(i) Equilibrium isotopic fractionation decreases as temperature increases, roughly in proportion to $1/T^2$. Thereby exceptions can occur, if the fractionation is very small or the element of interest is bonded directly to hydrogen in one phase.

(ii) The isotopic fractionation is largest with low atomic mass (light elements) and large relative mass difference ($\Delta m/m$) between rare and abundant isotope, where Δm denotes the unit mass difference and m is the average mass of the isotopes of that element.

(iii) Heavy isotopes of an element will tend to be concentrated in substances with the highest bond-strength, whereby the magnitude of the fractionation is proximate proportional to the stiffness of the bond. Bond stiffness is greatest for short, strong chemical bonds, which generally occur by high oxidation state, low coordination number, bonding of elements near the top of the periodic table, high covalent character and low spin electronic configuration for transition elements.

For example, an ionic bond with a low ratio of ionic radius to charge is characterized by high vibration mode and has a tendency to enrich the heavy isotope. E.g., in the mineral quartz, the high charged and small Si^{4+} bonds on oxygen, whereas the oxygen is bonded in magnetite to the less charged Fe^{2+} and Fe^{3+}. For this reason, quartz yields the highest and magnetite the lowest ^{18}O.

The fact that silicon has only a single predominant oxidation state in nature facilitates the circumstances. Furthermore, it is known that the isotopic fractionation of main group lithophile metals like Li, Mg, Si and Ca are more likely to reflect changes in the coordination number.

1.2.3. Kinetic fractionation

Kinetic fractionation is characterized by a reaction, which runs in one direction (unidirectional), is fast and incomplete, such as diffusion or evaporation (Melander and Saunders, 1980; Hoefs, 1997). This fractionation process describes a chemical reaction, which does not achieve equilibrium. The lighter isotope will usually be preferentially concentrated in the reaction products, because of the bonds involving light isotopes in the reactants being more easily broken. In general kinetic fractionation is characterized by different translational motion of the molecules in a phase. Due to higher mobility (and higher average velocity) of the light molecules, the reaction product is enriched in the light isotope. Therefore the light isotopes are more reactive, diffuse faster or are preferentially in the gas phase on a liquid/gas phase transition, whereas the heavy isotopes are more stable and preferentially stay in the initial reservoir

An interesting example of a kinetic effect is the fractionation of O isotopes between liquid water and vapour. The resulting fractionation of isotopic water molecules is a direct consequence of the effect of the masses of isotopic molecules on their velocities. The lightest molecule ($^{1}H_{2}{}^{16}O$) evaporates preferentially due to the higher velocity at higher rates than the heaviest water molecule ($D_{2}{}^{18}O$). Therefore water vapour is depleted in D and ^{18}O relative to the liquid and enriched in isotopically lighter water molecules

Kinetic fractionation encompasses a number of distinct fractionation mechanisms and show similar qualitative behaviour in isotope exchange like equilibrium fractionation. However, they are more difficult to describe with a list of applicable rules. Generally kinetic isotope fractionation occurs in conjunction with low-temperature chemical processes (biological mediated reactions, e.g. photosynthesis, bacterial reduction). The magnitude of fractionation is commonly larger in kinetic reactions than for equilibrium reactions. However, generally it does not decrease in magnitude with increasing temperature in the same way that equilibrium fractionations do. Furthermore, kinetic fractionations usually depend on many variables (reaction rates and the presence of exchange catalysts) in addition to temperature.

1.3. Silicon stable isotopes and the terrestrial/extraterrestrial $\delta^{30}Si$ variation

1.3.1. Silicon stable isotopes

Silicon (z = 14, atomic mass = 28.0855) has three stable isotopes: ^{28}Si (27.976927), ^{29}Si (28.976495) and ^{30}Si (29.973770) with the relative abundances of 92.23%, 4.67% and 3.10%, respectively (Faure and Mensing, 2005). The relative mass differences are 7.8 (^{30}Si, ^{28}Si) and 3.5 (^{29}Si, ^{28}Si). In addition, silicon has a radioactive isotope ^{32}Si of

cosmogenic origin with a half-life of 140 ± 6 years. The silicon isotope composition of a sample is expressed using the δ-notation as δ^{30}Si and δ^{29}Si in parts per thousands relative to the international standard NBS-28 (chapter MC-ICP-MS).

$$\delta^{30}Si = \left[\frac{\left(\frac{^{30}Si}{^{28}Si} \right)_{sample}}{\left(\frac{^{30}Si}{^{28}Si} \right)_{NBS28}} - 1 \right] * 1000 \qquad \text{or} \qquad \delta^{29}Si = \left[\frac{\left(\frac{^{29}Si}{^{28}Si} \right)_{sample}}{\left(\frac{^{29}Si}{^{28}Si} \right)_{NBS28}} - 1 \right] * 1000$$

It is common practice in isotope-geochemistry to describe isotope variations in terms of their mass-dependent fractionations in a three-isotope space (plot of δ^{29}Si versus δ^{30}Si, Fig 1). The mass-dependent fractionations are obliged to fall on a straight line within the δ^{29}Si-δ^{30}Si-space. Until now, there are no mass-independent isotope fractionations found on terrestrial material, thus every fractionation of Earth's samples is supposed to be dependent only on the masses of the isotopes and should plot on this correlation curve. Any deviations from this line might indicate a non-mass dependent isotope effect (Clayton et al., 1973). For example, inherited anomalies of extraterrestrial SiC grains in meteorites do not fit on the mass dependent Si isotope fractionation array (Stone et al., 1991). Those anomalies are assumed to have emerged during presolar nucleosynthesis (Zinner et al., 1989).

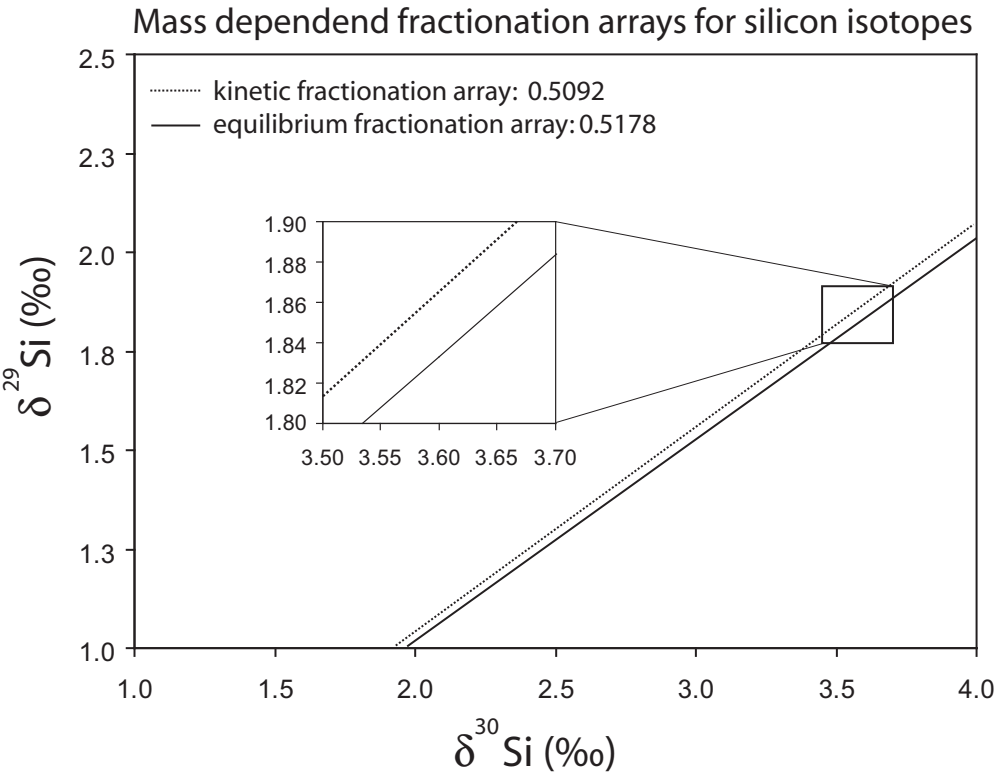

Fig 1: The mass-dependent fractionation slopes for Si. The slopes of β_{Kin} = 0.5092 (for Si atoms) and β_{equ} = 0.5178 only differ slightly.

Mass fractionation laws for equilibrium and kinetic processes differ (Fig 1). This is due to the fact that kinetic fractionation is often described using effective masses, whereas equilibrium exchange is purely a quantum phenomenon that depends on the atomic masses alone (Young et al., 2002). In practice, kinetic fractionation produces curves in three-isotope space that have smaller slopes than those produced by equilibrium exchange (where $\delta^{29}Si$ is the ordinate and $\delta^{30}Si$ is the abscissa). Following Young et al., 2002 the slopes β of the mass fractionation curves can be calculated with exact atomic masses of: ^{28}Si (27.976927), ^{29}Si (28,976495) and ^{30}Si (29,973770).

Kinetic $$\beta_{kin} = \frac{\ln(m_1 / m_2)}{\ln(m_1 / m_3)}$$

Equilibrium $$\beta_{equ} = \frac{(1/m_1 - 1/m_2)}{(1/m_1 - 1/m_3)}$$

With $m_1 = ^{28}Si$, $m_2 = ^{29}Si$ and $m_3 = ^{30}Si$, the different slopes can be calculated: $\beta_{equ} = 0.5178$ for equilibrium fractionation and $\beta_{kin} = 0.5092$ for Si atoms and $\beta_{kin} = 0.505$ for SiO_2 molecules for kinetic fractionation (Fig. 1). However the level of precision in the current technology of Si isotope analytic is not sufficient to distinguish both mass fractionation laws over limited ranges in isotopic composition. Therefore the mass fractionation line is more used as a data quality indicator, since unresolved interferences or problems in the Si isotope analysis should cause isotope ratios to be shifted away from the expected terrestrial mass-dependent fractionation.

Before the measurement of $\delta^{30}Si$ was possible on a conventional Nu Plasma™ mass spectrometer (chapter 1.4), a simplified mass-dependent fractionation law, based on an approximation valid for small ranges of isotopic fractionation (Johnson et al., 2004) was used to convert the analysed $\delta^{29}Si$ in $\delta^{30}Si$. Following an equilibrium or kinetic mass dependent fractionation, $\delta^{30}Si = \delta^{29}Si * 1.93$ or $\delta^{30}Si = \delta^{29}Si * 1.96$ was used, respectively.

1.3.2. Terrestrial/extraterrestrial silicon isotope fractionation

Total range of terrestrial silicon isotope fractionation is small in comparison to common other light elements ($\delta^{30}Si$ = -5.7‰ to +6.1‰, Basile-Doelsch et al., 2005; Ding et al., 2005a). The distribution of Silicon isotopes in various reservoirs is shown in Fig. 2.

Fig 2: Main terrestrial and extraterrestrial silicon isotope reservoirs

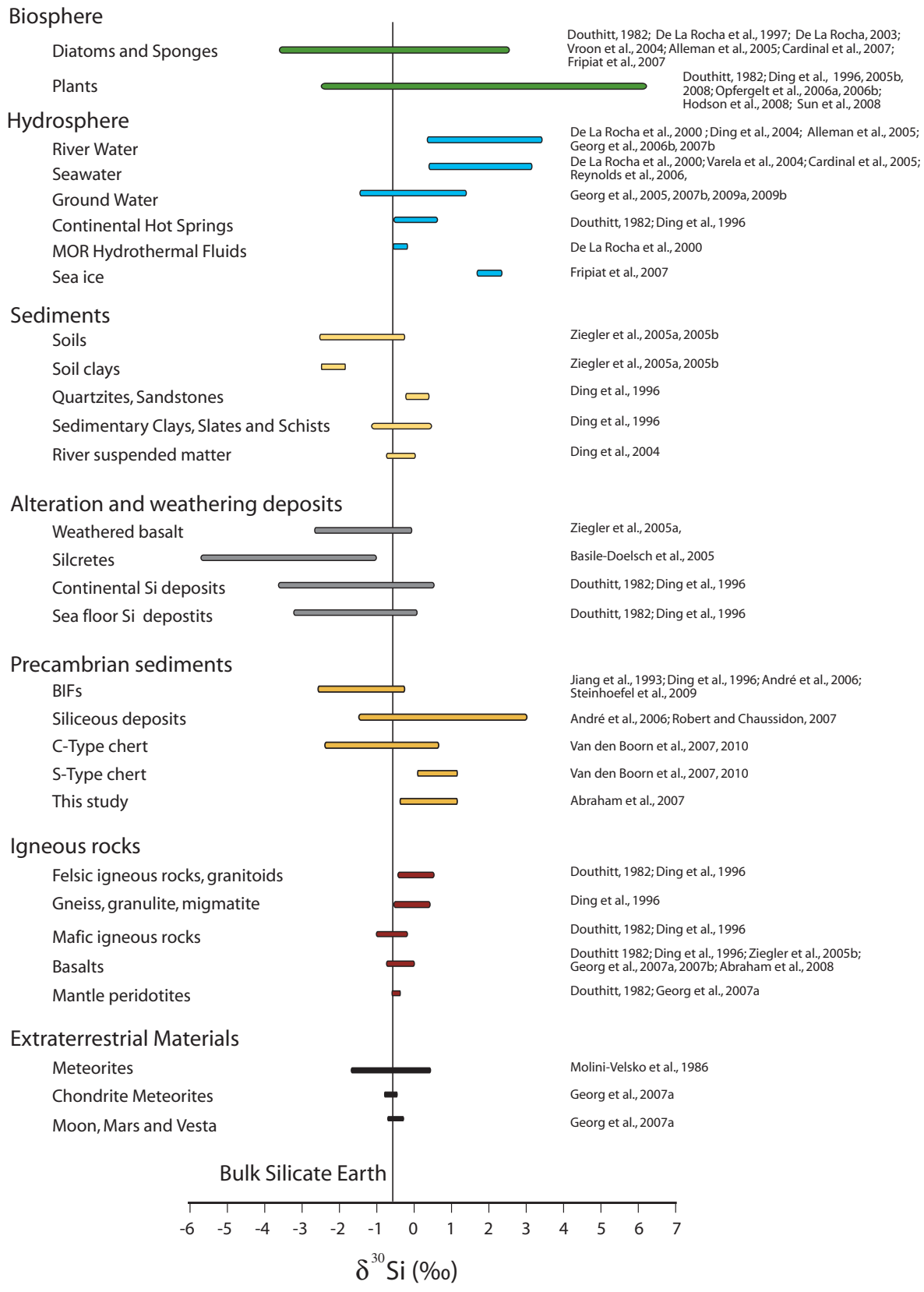

First investigations of stable silicon isotopes can be dated back to the 1950s (Reynold and Verhoogen, 1953; Allenby, 1954). However, due to the severity of Si purification methods and the poor analytical precision and accuracy accomplishable at that time, the reliability of these first results is doubtful. In subsequent studies, analytical precision was improved by the introduction of new analysis methods e.g. using isotope ratio mass spectrometry (IRMS, Tilles, 1961; Douthitt, 1982; Molini-Velsko et al., 1986; De La Rocha et al., 1996), culminating in the onset of MC-ICP-MS in the mid 1990s (for details see Chapter 4.2.). Until now more than 100 articles on Si stable isotopes were published, whereby the majority of these articles emerged in last years, illustrating the increased interest on this research field on the basis of the ability to determine smaller isotope variations. Whereby, the two most comprehensive and most frequently referred studies are the publication of Douthitt (1982) and a book of Ding (1996). However, most articles cover analytical methods and fractionation in natural systems and only few publications about experimental or theoretical approaches on the dimension of isotope fractionation exist (Georg et al. 2007b; Méheut et al., 2007, 2009).

Extraterrestrial mass-independent Si fractionation has a much larger range than the fractionation on Earth. Such "isotopic anomalies" may result from incomplete homogenization of isotopically very diverse nucleousynthetic components within the solar system. E.g. refractory calcium-aluminium-rich inclusions (CAIs) in primitive meteorites and presolar circumstellar SiC (silicon carbide) grains possess widespread Si anomalies in the magnitude of tens to hundreds of permil (Ding et al., 1996; Lugaro et al., 1999; Shahar and Young, 2007; not shown in the Fig 2). In contrast, the small range of isotopic compositions for chondrites and basaltic achondrites from Mars and Vesta implicate that the solar system is close to being isotopically uniform. Consequently, meteorites are regarded as representative for the Solar Nebular reservoir (Molini-Velsko et al., 1986) and can be used to deduce the isotope composition of the total Earth (average δ^{30}Si of meteorites: -0.58 ± 0.06‰, with ±1 standard deviation, s.d., Georg et al., 2007a).

Endogenous rocks range from -1.1‰ to +0.7‰ (Douthitt, 1982; Ding et al., 1996). Due to a compositional overlap of mantle and mantle-derived mafic rocks with the average ^{30}Si/^{28}Si ratio of bulk meteorites the silicon isotope fractionation during partial melting is expected to be small (Douthitt, 1982; Ding et al., 1996; Georg et al., 2007a). In addition the fractionation between silicate minerals in igneous rocks (Feldspar-Hornblende, Quartz-Feldspar, and Feldspar-Pyroxene) generates only small fractionations of 0.2-0.5‰ (Ding et al., 1996). A difference in δ^{30}Si exists between the total Earth (-0.58‰) and the Bulk Silicate Earth (BSE = -0.38‰, average of lherzolites and mantle-derived mafic rocks, Georg et al., 2007a). These data and data of lunar rocks (similar compositions like BSE; -0.31‰) gave rise to

the assumption that silicon was incorporated into the Earth´s core prior to lunar formation, with the core representing a light isotopic complementary reservoir to the slightly heavier BSE (Georg et al., 2007a, Fitoussi et al., 2009). This supposition was endorsed by density functional perturbation theory calculations (Baroni et al., 2001; Gonze et al., 2002) of metal and silicate partitioning.

In general, suggested on theoretical calculations (Grant, 1954), the silicon equilibrium isotope fractionation is correlated with the SiO_2-content (the silicon rich phase is enriched in ^{30}Si with respect to the silicon depleted phase) and the degree of polymerization. Furthermore, experimental observations substantiate a heavier isotope signature with progressed magmatic differentiation (Douthitt, 1982; Ding et al., 1996). This can be found as well in natural systems, since felsic igneous rocks (~0‰) are isotopically heavier than their mafic counterparts (-0.3‰). Anyway, a first-principles approach on equilibrium isotopic fractionation of oxygen and silicon for several minerals, displaying various degree of polymerization of silicate units (Méheut et al., 2009), indicate that the fractionation factor of Si in equilibrium does not strictly follow the polymerisation degree of silicate tetraeder, as previously suggested by Grant (1954).

Exogenous rocks show much larger range than endogenous rocks, since water-rock interaction induces significant isotope effects. The disintegration of igneous rocks by *weathering* induces the production of secondary minerals bearing lighter $\delta^{30}Si$ such as *clays* (Douthitt, 1982; Ding et al., 1996; De La Rocha et al., 2000; Ziegler et al., 2005a, 2005b; Opfergelt et al., 2008, 2010) and *silcretes* (Douthitt, 1982; Ding et al., 1996; Basile-Doelsch et al., 2005). Thereby, the newly formed minerals are ^{30}Si-depleted with respect to the precursor rock. Coevally, the dissolved Si in the interacting fluid is left behind enriched in ^{30}Si. Clays are only slightly isotopically lighter, with a $\delta^{30}Si$ ranging from -2.3‰ to +0.1‰. Based on chemical precipitation experiments the silica and clay fractionation is expected to be -0.3‰ to -3.8‰ lighter than the initial water (Ding et al., 1996; Ziegler et al., 2005b). Whereby, for example, the equilibrium isotope fractionation at 100°C is calculated to be $\Delta^{30}Si = 1.12‰$ between quartz and kaolinite and $\Delta^{30}Si = 3.69‰$ between quartz and lizardite (Méheut et al., 2007, 2009). Silcretes represent the most ^{30}Si-depleted pool analyzed so far, with $\delta^{30}Si$ down to -5.7‰ (in the range of -5.7 to -1.6‰), thereby the quartz cement of silcretes is -2.4‰ more negative than the water (Basile-Doelsch et al., 2005). The large isotopic shift observed in silcretes can be explained by repeating dissolution and precipitation events of quartz. In contrast, the isotope composition of *clastic sediments* (schist, slate, sandstone and quartzite) is not very different from igneous rocks. Thus, it was assumed that the decomposition of silicate does not yield any significant Si

isotope effect (Ding et al., 1996), which was disproved by Ziegler et al. (2005b) and Demarest et al. (2009) for incongruent dissolution.

Si is present as a solute in ***aquatic systems***. It occurs mostly (~95%) as the undissociated monomeric silicic acid $Si(OH)_4$ (Treguer et al., 1995). The Si isotope fractionation during precipitation of solid material is likely to follow the rules of kinetic isotopic fractionation, according to the preferential precipitation of the dissolved $^{28}Si(OH)_4$, leaving the residual solution enriched in $^{30}Si(OH)_4$ (Ding et al., 1996). Due to this fractionation, different silicon isotope reservoirs emerge: the dissolved Si in rivers and seawater is ^{30}Si-enriched ($-0.8‰<\delta^{30}Si<+3.4‰$) compared to Si in endogenous rocks ($-1.1‰<\delta^{30}Si<+0.7‰$). This global enrichment is counterbalanced by the pool of secondary Si-bearing phases (biogenic silica, clays, quartz) which represents the ^{30}Si-depleted reservoir ($-5.7‰<\delta^{30}Si<+2.6‰$) (Basile-Doelsch, 2006).

The dissolved Si is distributed in several pools: *fresh water (lake and river)* ranges from +0.4‰ to +3.4‰ (De La Rocha et al., 2000; Ding et al., 2004; Alleman et al., 2005; Georg et al., 2006a, 2007c) and *seawater* ranges from +0.6‰ to +3.1‰ (De La Rocha et al., 2000; Varela et al., 2004; Cardinal et al., 2005), with a mean value of +1.1‰ (De La Rocha et al., 2000; Ding et al., 2004). In contrast, few data from *hydrothermal* brines on mid-ocean ridge settings display slightly negative δ^{30}Si (Douthitt, 1982; De La Rocha et al., 2000; Ding et al., 1996). Their derived precipitates and associated siliceous deposits form continental hot springs yield even lighter δ^{30}Si values (Douthitt, 1982; Ding et al., 1996). The positive Si isotope budget of the ocean is mainly influenced by drainage of the δ^{30}Si-enriched river water and the preferential removal of the light isotopes by biomineralization δ^{30}Si in g*roundwater* ranges from -1.42‰ to +1.34‰ (Georg et al., 2006b, 2007c, 2009a, 2009b).

The production of ***biogenic silica*** by biomineralization induces a range of isotope variations of 9.8‰, which represents the largest range of δ^{30}Si observed in nature, comparing to the whole terrestrial isotope fractionation range determined so far (11.8‰). During biomineralization, it is a common feature that the produced biogenic silica yields isotopically lighter signature by discrimination against heavy Si isotopes during Si uptake and/or precipitation, as explained above. Silicon is often an essential element in *plants* which precipitate as opal amorphous particles, phytoliths, isotopically lighter than the Si source (Ding et al., 2005b; Opfergelt et al., 2006a, 2006b, 2008; Engström et al., 2007). In addition, silicon is an important component of the *marine biogenic matter*. Some marine organisms have strict Si requirements to grow. Diatoms - a major group of phytoplankton, build their amorphous silica with δ^{30}Si lighter

than the surrounding waters - (De La Rocha et al., 1997; Alleman et al., 2005; Cardinal et al., 2007; Reynolds et al., 2006; Fripiat et al., 2007), as sponges (De La Rocha, 2003). There are other silica mineralizing groups such as silicoflagellates and radiolarian which utilize $Si(OH)_4$ to build up their skeleton composed of opal but their isotopic fractionation is unknown. This pool of silica secreting organisms represents by far most important sink of Si in Phanerozoic oceans. The most ^{30}Si-depleted biogenic silica has been measured in sponges with a δ^{30}Si of -3.7‰ (Douthitt, 1982; De La Rocha, 2003).

Precambrian deposits differ from Palaeozoic, since they do not originate from a biogenic process. Cherts in Banded Iron Formations (BIF´s) yield negative δ^{30}Si values (Ding et al., 1996; André et al., 2006; Steinhoefel et al., 2009). Other Precambrian siliceous deposits exhibit a wider range, including positive δ^{30}Si values (this study, Robert and Chaussidon, 2006; van den Boorn et al., 2007, 2010). Van den Boorn et al. (2007, 2010) subdivides Precambrian cherts in silicified precursor rocks (S-cherts) and chemical precipitates (C-cherts).

Chapter 2

2. Geological context

The Barberton Granite Greenstone Terrain (BGGT, 3.55 – 3.22 Ga) is situated in the eastern part of the Kapvaal Craton, South Africa and Swaziland (Brandl et al., 2006; Lowe and Byerly, 2007, Fig 4). It consists of mainly two components: the NE-SW striking supracrustal succession of the Barberton Greenstone Belt (BGB) and associated intrusive granitoid suites, which are surrounding and intruding the BGB (Viljoen and Viljoen 1969; de Ronde and de Wit, 1994; Lowe and Byerly, 1999). The intrusive units can be grouped into two major types of igneous rocks (Lowe and Byerly, 2007): The TTG group (trondhjemite-tonalite-granodiorite) and the GMS group (granite-monzonite-syenite). The former has, despite high silica content, a predominance of plagioclase over alkali feldspar, whereas in the latter plagioclase is subordinate to alkali feldspar. The latter group was determined by de Wit (1998) as the granodioritic–granitic–monzogranitic (GGM) series.

2.1. The stratigraphic units of the Barberton Greenstone Belt

The BGB includes volcanic, sedimentary, and shallow-level intrusive rocks. De Wit et al. (1992) regarded the BGB to consist of two distinct tectono-stratigraphic terrains, the northern Barberton greenstone terrain and southern Barberton greenstone terrain, whereas Lowe (1994, 1999) considered it to consist of several smaller (four or five) tectono-stratigraphic blocks, which become progressively younger towards the north.

The BGB can be divided into three main lithostratigraphic units: from base to top, 1) the *Onverwacht Group*, a lower predominantly volcanic sequence, composed largely of mafic to ultramafic rocks, with subordinate felsic volcanic flow units and tuffs, 2) the *Fig Tree Group*, a middle volcaniclastic and quartz-poor succession and 3) the *Moodies Group*, an upper quartzose terrigenous unit (Lowe and Byerly, 1999, 2007).

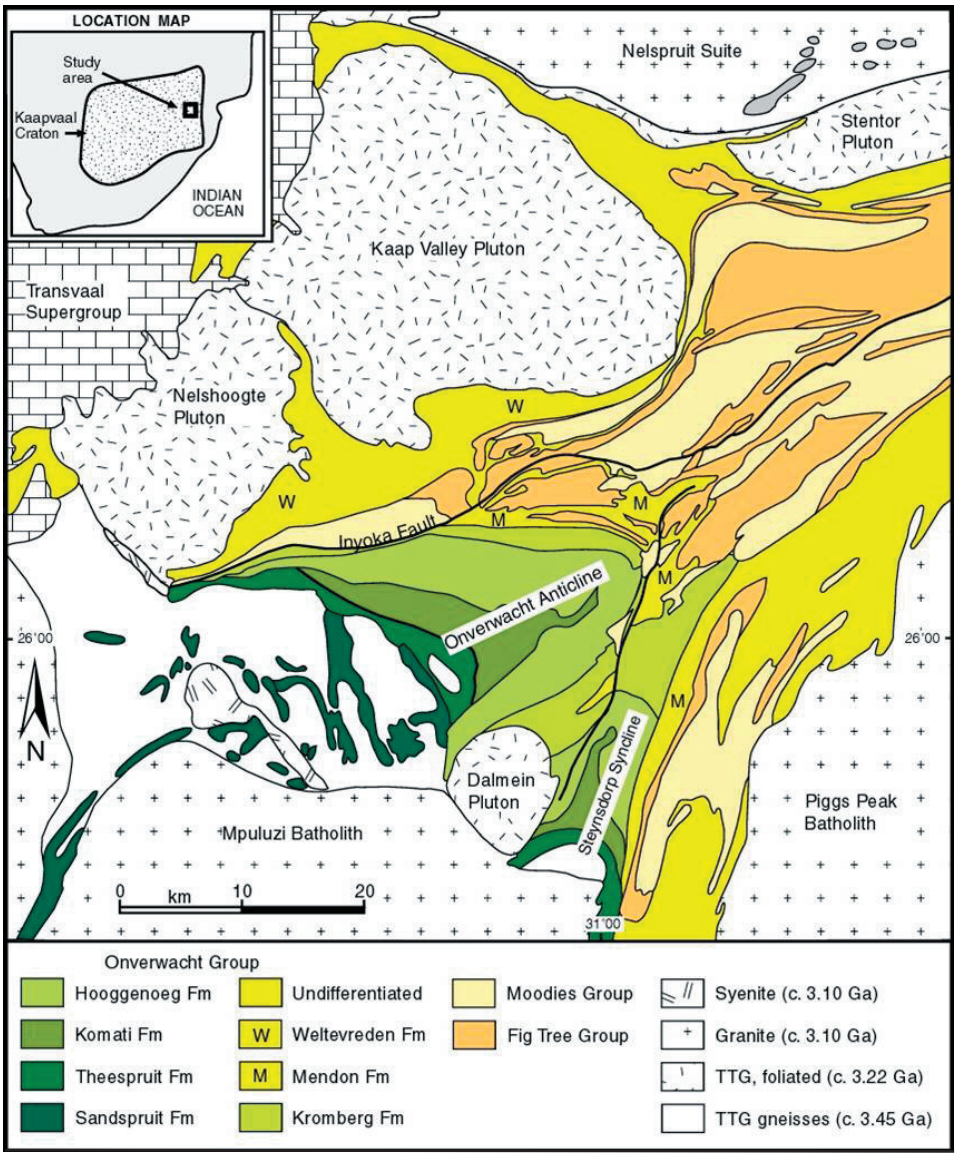

Fig. 4. Geological map of the south-western part the Barberton Greenstone Belt and surrounding TTG plutons (BGGT, modified from Kamo and Davis, 1994; Lowe and Byerly, 1999).

The *Onverwacht Group* includes ultramafic and mafic volcanic rocks (komatiites, komatiitic basalts, basalts), with minor dacitic volcanic rocks. Both are mostly interbedded with thin, commonly silicified sedimentary units, assumed to have formed in a deep to shallow marine environment during breaks in volcanic activity. The stratigraphic thickness of the Onverwacht group ranges from 1 km in the western and northern edge (~3330 to ~3240 Ma) to more than

10 km in the southern part (3547 to ~3260 Ma, Lowe and Byerly, 2007). The Onverwacht Group can be broadly subdivided into a lower ultramafic unit and an upper mafic to felsic unit, separated by a prominent unit of chert, known as Middle Marker (Viljoen and Viljoen, 1969). The lower and upper units are each composed of three formations, namely Sandspruit, Theespruit, Komati and Hooggenoeg, Kromberg and Mendon formations (Viljoen and Viljoen, 1969; Lowe and Byerly, 1999). The Onverwacht Group was named by Hall (1918) for outcrops of mafic volcanic rocks on farm Onverwacht 733JT in the southern part of the BGB. The *Fig Tree Group* (~3260 to 3225 Ma) characterizes a transitional unit up to 1800 m in thickness. It comprises of interlayered volcaniclastic strata, which can be regarded as the final stage of eruptive activity in the greenstone belt volcanism. The *Moodies Group* (post-3225 Ma) has a stratigraphic thickness of up to 3000 m and comprises of chert-clast conglomerate and coarse, quartzose and feldspathic sandstone, which are derived from erosion of uplifted plutonic rocks and underlying greenstone units.

2.2. The structural evolution of the Barberton Granite Greenstone Terrain

The structural evolution of the BGGT has been addressed by many authors (e.g. Ramsay, 1963; Anhaeusser, 1976, 1983; de Wit et al., 1983, 1987; Kamo and Davis, 1994; Lowe, 1999; Brandl et al., 2006; Lowe and Byerly, 2007). The BGGT formed between 3510 Ma and 3110 Ma. The main deformation events (D1-D5) coincide with peaks of magmatic activity at 3550 Ma, 3450 Ma, 3250-3220 Ma and 3100 Ma and reflect the episodic evolution of the BGGT (Kamo and Davis, 1994; Lowe, 1999; Lowe and Byerly, 2007). The crustal history and the most important deformation events (D1-D3) and are described more in detail here.

Pre-D1-Deformation

Evidence exists for a pre-Onverwacht Group crustal history, which is poorly constrained at present. Some data suggest (Kisters and Anhaeusser, 1995, Kröner et al., 1996; Kisters et al., 2003) that even older tectono-magmatic cycles may have preceded the D1-Deformation due to the formation of foliation and gneissic textures in the Steynsdorp Pluton (3509 ± 8/7 Ma) and faulting, folding, and structural repetition of several felsic volcanic rocks of the 3531 ± 10 Ma (Armstrong et al., 1990) and 3511 ± 3 Ma (Kröner et al., 1992) Theespruit formation, in the Onverwacht and Steynsdorp Anticlices.

The oldest rocks (trondhjemitic gneisses) so far recognized in the Kaapvaal Craton are located in the Ancient Gneiss Complex (AGC) with zircon ages up to 3644 ± 4 Ma (Compston and Kröner, 1988; Kröner et al., 1989; 1996), providing evidence for early development of crust in this region. In general, the AGC has been widely regarded as a possible basement on which the greenstone volcanics were deposited (Hunter, 1974; Kröner and Todt, 1988).

It is generally accepted that early mafic to ultramafic Onverwacht volcanism (3472 to 3458 Ma) took place in extensional oceanic, oceanic plateau or island arc settings, due to the resemblance with Phanerozoic ophiolite-like sequences. However, divergent opinions exist about the exact plate tectonic setting.

Deformation 1

D1 represents the earliest well-documented deformation event in the BGB. According to de Ronde and de Wit (1994), the D1 event was associated with thrust faulting, which was restricted to the southern part of the BGB. In particular, in the range between 3445 ± 4 and 3416 ± 7 Ma (de Ronde and de Wit, 1994), newly formed Onverwacht oceanic rocks were delaminated at an intra-oceanic subduction-like environment onto an active arc-like terrain (de Wit et al., 1987; de Ronde and de Wit, 1994; Cloete, 1999). This deformation event culminated in felsic magmatic activity of the trondhjemitic suite (e.g. Stolzburg and Theespruit Plutons).

Deformation 2

The second accretion event (D2) probably extended from about 3230 to 3225 Ma and represents the first regional and perhaps the main deformational event in BGB history (de Ronde and de Wit, 1994, Lowe, 1999). It was associated with the deposition of the Fig Tree Group in an island arc setting from ca. 3258 ± 3 Ma on (de Ronde and de Wit, 1994; Byerly et al., 1996) and its subsequent deformation. The D2-Deformation represents a major period of convergent tectonism, with collisional suturing (de Wit, 1991; de Ronde and de Wit, 1994) and the amalgamation of the BGB and AGC terrains. In detail, this event was widely regarded as having involved the amalgamation and suturing of an older terrain in the SE (~3445 Ma) with the younger post-3330 Ma terrain to the NW. The suture is commonly considered to occur along the Saddleback-Inyoka fault (de Ronde and Kamo, 2000; Anhaeusser, 2006). The collision events coincide with intrusions of the TTG-granitoids, e.g. the Nelshoogte Pluton (3236 ± 1 Ma, de Ronde and Kamo, 2000) and the Kaap Valley Pluton (3228 ± 1 Ma, Kamo and Davis, 1994). Associated with the intrusion is an amphibolite facies overprint (=peak metamorphism) at ca. 3230 Ma in the southern and northern part of the BGB

in the region of the Granitoid-Greenstone contact. The P-T-conditions are 650-700 °C at ca. 8 to 11 kbar (Dziggel et al., 2002). In the centre of the BGB a lower degree of metamorphism has been documented.

Deformation 3

Post-Fig Tree deformations are less well clarified in the BGB, partly owing to the cease of magmatism in Fig Tree time. However, the D3 deformation is accompanied by the intrusion of GMS granitoids, such as Nelspruit Batholit (3106 ± 3 Ma Kamo and Davis, 1994). The D3-event is basically characterized by strike-slip and thrust faults. The D3-shear zones were interpreted as a consequence of a transtensional deformation-event (de Ronde and de Wit, 1994; Kamo and Davis, 1994). Subsequent to the amalgamation, the deformation was accompanied by the deposition of rocks of the Moodies Group. The thick Moodies sequence appears to have been accumulated in a number of separate basins, which were formed in part in extensional settings (Lowe, 1994, 1999; Kisters et al., 2003) and in part during thrusting (Heubeck and Lowe, 1994, 1999).

2.3. Evolution of the Barberton Granite Greenstone Terrain

The evolution of the continental crust of the BGGT can be summarised in terms of three evolutionary stages (Lowe, 1999; Lowe and Byerly, 2007):

1) The main tectono-stratigraphic units formed through magmatic accretion (3550 Ma, probably 3700 Ma to 3230 Ma), in which at least four and possibly more cycles of magmatic episodes were involved over an interval of 320 Ma. The formation of each cycle comprises a) an initial period of ultramafic and mafic volcanism, followed by b) a felsic magmatic stage during which the mafic and ultramafic volcanic sequence was intruded by TTG plutons and covered by comagmatic dacitic to rhyolitic volcanic rocks
2) Deformation, shortening, amalgamation and suturing of tectono-stratigraphic units to form a larger, quasi-continental block (~ 3230-3216 Ma).
3) Underplating, late intracrustal melting and post-kinematic potassic plutonism cause thickening and stabilization of the crust (~ 3216-3100 Ma).

In the context of this thesis, the rock samples investigated arise from 3 different sections (Theespruit, Hooggenoeg and Kromberg formation, (Section III) of variably silicified volcanic rocks with bedded cherts on top, from the Onverwacht Group. Furthermore, nine intrusive units (from TTG to GMS group) have been sampled (in detail described in Section IV).

Chapter 3

3. Precambrian silica formation

The Precambrian geochemical silica cycle is only poorly investigated, since only few authors dealt with the research of this topic (e.g. Siever, 1992; Perry and Lefticariu, 2003; Maliva et al., 2005). Two main types of large scale silica mobilization are evidenced in Archaean supracrustal sequences: (1) prevalent silica-rich rocks (cherts) associated with Banded Iron Formations and (2) conspicuous silica impregnation of various greenstone suites.

3.1. The formation and geochemistry of Precambrian cherts

Archaean cherts represent the oldest remnants of sedimentary deposition. For this reason they comprise precious information about the ambient conditions on the early Earth.

Major interest in Precambrian cherts arises from the exquisite preservation of assemblages of microfossils. Cherts can preserve the chemical properties of microorganisms and their morphological outlines. For this reasons cherts are our most direct evidence of life forms as old as 2,000 Myr (Barghoorn and Tyler, 1965; House et al., 2000) and perhaps much older (Awramik et al., 1983; Schopf, 1993, and references therein; Schopf et al., 2002).

The most important aspect of the study of Precambrian cherts derives primarily from the fact that they have potential to preserve a record of the isotopic signature and therewith important information of ancient conditions, most notably the seawater temperature. Due to the fact that chert is high resistant to metamorphic processes and accompanied dissolution and re-crystallization reactions (Knauth, 2005), their $\delta^{18}O$ values have been used to trace ocean paleotemperature in which they are assumed to be in equilibrium, whereby the equation $1000\ln\alpha_{chert\text{-}water} = 3.09*10^{6}T^{-2}-3.29$ (with α = oxygen isotope fractionation factor; Knauth and Epstein, 1976) gives the temperature dependence. However, this further means that either the surface temperature or the isotopic composition of the precipitating fluid (seawater) must be known to determine the other, which leads to controversial discussions.

Chert is a chemically precipitated sedimentary rock, which is basically composite of silica (~ 90 %) under diverse crystalline forms: microcrystalline quartz (microquartz), chalcedonic silica, megaquartz and detrital quartz. Other constituents are impurities, such as phyllosilicates, carbonates, iron oxides, and carbonaceous matter (Folk, 1980; Knauth, 1994; Lowe, 1999; Perry and Lefticariu, 2003).

The formation of Phanerozoic deep sea cherts is very well constrained. The diagenetic maturation sequence is the following: soluble opal-A (siliceous ooze) converts diagenetically

over a period of 10^3 (Bohrmann et al., 1994) to 10^7 years to opal-CT (porcelanite, solubility 25–60 ppm; Kastner et al., 1977; Siever, 1992) and finally to chalcedony or cryptocrystalline quartz/chert (Perry and Lefticariu, 2003). The presence or absence of clay minerals and the temperature during diagenesis are influencing the rate of the conversion of the phases. Under special circumstances chert can obviously be formed directly form opal-A, if the concentration of silica remains below the solubility of opal-CT (Knauth, 1994).

Contrary, the formation of Precambrian chert is not very well investigated. It is generally thought that chert formed initially as amorphous silica (Hesse, 1989; Knauth, 1994; Hattori et al., 1996). In contrast to the recent cherts, Precambrian cherts show no evidence of opal CT as a precursor of microquartz. Rather, it has been suggested that the precursor of Precambrian chert could have been amorphous silica gel (Hesse, 1989; Knauth, 1994), whereby the complete dissolution and re-precipitation to microquartz leaves no visible track in the rock. Sorption of silica on iron oxides, clay minerals, or organic matter may have played a role in the nucleation and/or precipitation (Perry and Lefticariu, 2003, Konhauser et al., 2007; Delstanche et al., 2009). It has also been claimed that cherts can precipitate directly as quartz (Mackenzie and Gees, 1971; Simonson, 1987; Winter and Knauth, 1992; Knauth, 1994) without any silica precursor. Another possibility for the chert formation is the replacement of primary carbonates by silica (Walker, 1960; Knauth, 1979; Lougheed, 1983). In that case, nevertheless, the first precipitated silica form is opal CT (Knauth, 1979; Hesse, 1989; Knauth, 1994) and microquartz generates by the dissolution of it in mixed waters, supersaturated with respect to quartz and undersaturated with respect to carbonate (Knauth, 1979).

The main Phanerozoic chert types also occur in Precambrian strata, with the obvious exception of cherts related to organisms that had not evolved. Some differences between Precambrian and typical Phanerozoic cherts are recognized: for example, the timing of silicification differs, since it occurs early in the Precambrian and close to the sediment-water interface (e.g. early diagenetic peritidal cherts with microfossils), whereas in the Phanerozoic cherts silicification arises typically after some burial (Maliva et al., 2005). In addition, the location of chert formation changes form peritidal and shallow shelf environments in the Precambrian to a deep ocean environment nowadays.

The provenance of silica (direct precipitation from sea-water or leached volcanic rocks) still remains subject of debate (Buick and Dunlop, 1990; Nijman et al., 1999a; Kato and Nakamura, 2003; Knauth and Lowe, 2003; Van Kranendonk, 2006). Given that silica secreting organisms were absent in the Precambrian (Siever 1992; Maliva et al., 2005), the vast bulk of Precambrian chert was presumably derived from abiogenic precipitation. Therefore

the formation of chert could be a result of silica supersaturated seawater. Weathering of continental crust and the alteration of volcanic glasses could provide the required amount of dissolved silica to supersaturate seawater.

However, the term "chert" comprises not only chemical precipitates, but as well rocks, which are converted entirely to quartz (silicified or "chertified" rocks). Only the texture remains witness of the precursor rock, since after their formation those rocks consist of nearly 100% SiO_2. In the Swaziland Supergroup many cherts were formed by silicification of virtual every primary sediment and igneous rock type, including volcaniclastic and pyroclastic deposits, terrigenous detrital layers and biogenic sediments (Lowe, 1999).

3.2. Nature and depositional environments of Precambrian silicification

In contrast to the modern Earth, silicification of near-surface layers was a widespread process on the Precambrian ocean floor and can be regarded as a typical process for ocean floor alteration in the very early Earth. Silica alteration zones are a conspicuous feature of Archaean greenstone belt type localities all over the world (e.g. Pilbara, Australia, Kitajima et al., 2001; Oliver and Cawood, 2001; Terabayashi et al., 2003; Van Kranendonk and Pirajno, 2004; and Barberton, South Africa, Paris et al., 1985; Lowe and Byerly, 1986; Duchac and Hanor, 1987; Hanor and Duchac, 1990; Hofmann, 2005; Hofmann and Bolhar, 2007; Hofmann and Wilson, 2007; Hoffmann and Harris, 2008).

In general, silicification alters the rocks and thereby virtually entirely converts them to silica. The precursor rocks can only be recognized by remnants of sediment structures or pseudomorphs. By the replacement of volcanogenic sediments (DiMarco and Lowe, 1989a; Sugitani et al., 1996, 1998; Lowe, 1999; De Vries, 2004; Orberger et al., 2006), the sediment structures are casually preserved, therefore they still conclude volcanic detritus as lapilli or provide evidence for re-working of sediments in a shallow marine environment (DiMarco and Lowe, 1989b; Nijman et al., 1999b; De Vries, 2004). Evaporatic precursors are commonly identified by preserved silicified pseudomorphs of carbonate, gypsum and/or nahcolite and/or by remains of these precursor minerals (Buick and Dunlop, 1990; Sugitani et al., 1998; Lowe and Fisher Worrell, 1999).

The more frequent occurrence of silicification zones in ancient times can likely be attributed to different temperature and silica solubility conditions prevalent in the early Earth: The temperature of the ocean is supposed to have been hotter in the Archaean (around 70 °C) than on the modern Earth (Knauth and Lowe, 2003; Robert and Chaussidon, 2006) and Eoarchaean seawater was enriched in silica - the dissolved silica concentrations may have risen to levels close to or at saturation with respect to amorphous silica (Siever, 1992),

corresponding to about 2-3 $mmol^{-1}$ (Gunnarson, 2000). Additionally, the hydrothermal influx was assumed to be high in the Archaean (Siever, 1992) and owing to higher heat flow and thus higher degree of partial melting at mid ocean ridges (Nisbet et al., 1993; Kent et al., 1996; Foley et al., 2003) the Archaean oceanic crust was probably thicker than during the Proterozoic.

The origin of silicification in the Barberton area (Swaziland, South Africa) is unclear, however, leading to different hypotheses: Due to the high silica content of the rocks in the alteration zones early workers regarded some of these rocks to consist of felsic volcanics, a hypothesis that was later rejected. De Wit (1982) and Pearton (1982) have described these rocks as green quartz-carbonate schists formed by cataclastic metamorphism. Subsequent workers realized that such zones are formed by silica metasomatism of komatiitic volcanic rocks (Lowe and Byerly, 1986; Duchac and Hanor, 1987). For the metasomatism mechanisms Lowe and Byerly (1986) have suggested subaerial weathering. In contrast, Hanor and Duchac (1987) and Hanor and Duchac (1990) prefer the theory that silicification was initiated by hydrothermal seafloor alteration, which seems to represent the most likely explanation. Hydrothermal vents percolate the ocean seafloor basalts and cement them with varying degrees of silica. Thereby the deposition of silica is associated with leaching of other components out of the primary basaltic rock. The recently proposed model endorses the view of a low-temperature (100-150 °C) seafloor hydrothermal process for the silicification. Hydrothermal activity is dedicated to high heat flow in pre-Mesoarchaean times, resulting in the establishment of shallow subseafloor convections cells and a diffuse upflow of hydrothermal fluids over broad ranges (Hofmann, 2005; Hofmann and Bolhar, 2007; Hofmann and Wilson, 2007; Hoffmann and Harris, 2008).

3.3. The Precambrian Si isotope record

The origin of silica in the Precambrian ocean is controversial (Maliva et al., 2005). Generally, the silicic acid input into the ocean involves three pathways (Treguer et al., 1995): 1) Chemical weathering of sedimentary and crystalline rocks by CO_2-charged waters and transport by river runoff (climate-depending); 2) Aeolian erosion and transport. 3) Weathering of submarine basalt (low or high temperature alteration) and transfer by hydrothermal fluids

The study on modern hydrothermal brines indicate negative Si isotope signature (Douthitt, 1982; Ding et al., 1996; De La Rocha et al., 2000). Modern river systems, reveal slightly positive values (mean $\delta^{30}Si = +0.8‰ \pm 0.1‰$ ($(\pm 1\sigma_{SD})$ Georg et al., 2006b, 2007b. Generally it is assumed that the pathways were not differently to nowadays, except that there was presumably a higher hydrothermal flux during the Precambrian (Bau and Möller, 1993).

However, one pivotal discrepancy exists: as mentioned above, silica must have been close to or at saturation in the Precambrian ocean (Siever, 1992, Chapter 3.2). Anyway, it is not clear which mechanisms buffered or regulated the concentrations of silica in Precambrian sweater. In general, the silica solubility is a function of temperature, pressure (=water depth), PH, pCO_2 (higher partial pressure of CO_2 results in increased acidity), and exchange reactions with silicate minerals. Depending on these parameters the dissolved silica concentration in Precambrian seawater was assumed to reach 60 ppm (Siever, 1992; Simonson and Hassler, 1996) to 120 ppm (Morris, 1993). In contrast, predominantly biological controlled modern oceans yield very low silica concentration of ~1 ppm (Siever, 1992; Perry and Lefticariu, 2003), which is regarded to be steady-state in that the flux of silica into the oceans is balanced by its rate of removal, with an overall residence time of ~15,000 years (Treguer et al., 1995).

Cherts in BIFs yield negative $\delta^{30}Si$ values in the range of about -2.5‰ to -0.5‰. Their silica has been interpreted to be of hydrothermal origin (Ding et al., 1996; André et al., 2006; Steinhoefel et al., 2009). In contrast to the redox-sensitive element Fe, Si precipitation is independent from an oxidant and potentially occurred in the whole water column. Other Precambrian cherts exhibit a wider range, including positive $\delta^{30}Si$ values. They furthermore can be sub-divided into C-type and S-type cherts (van den Boorn et al., 2007, 2010). C-type cherts are described as cherts formed by orthochemical deposition of silica, whereas S-type cherts are interpreted to represent silicified precursor rocks (volcanogenic sediments). C-cherts are more depleted in their silicon isotope composition ($\delta^{30}Si$ = -2.4‰ to +0.6‰) than S-cherts ($\delta^{30}Si$ = +0.1‰ to +1.1‰) and cover a wider range. Generally, a rough classification for the origin of silica in chert can be performed by the distinction of two different fluid isotope signatures, since the seawater yields a positive and the hydrothermal fluid a negative Si isotope signature. However, positive values may reflect as well elevated temperatures of the seawater or the influence of a continental source (Robert and Chaussidon, 2006; De La Rocha et al., 2005; van den Boorn et al., 2007). Using the (1) hydrothermal silica source and the (2) seawater silica source in conjunction with the (3) Al_2O_3 content (as indicator for volcanogenic material) the two chert types can be distinct from each other by arraying two different lines in a three end-members component plot (van den Boorn et al., 2007). In a more detailed study of van den Boorn et al. (2010) the source of silica and the geological setting are specified. They conclude that the extreme isotope variability in C-cherts reflects a combination of seawater mixing and fractionation by conductive cooling of hot hydrothermal fluids, whereas, the scarcity of isotopically depleted S-cherts suggests that ambient seawater was the main source. The two different chert types are

generated on different geological settings: chemical cherts are deposited in deeper parts of the ocean, where the strongly ^{30}Si-depleted hydrothermal signatures are retained and S-cherts are generated in shallow and tidally influenced settings where hydrothermal signatures are largely lost due to more intensive mixing with seawater. Section III gives further description about the silica source and the mechanisms of silicification.

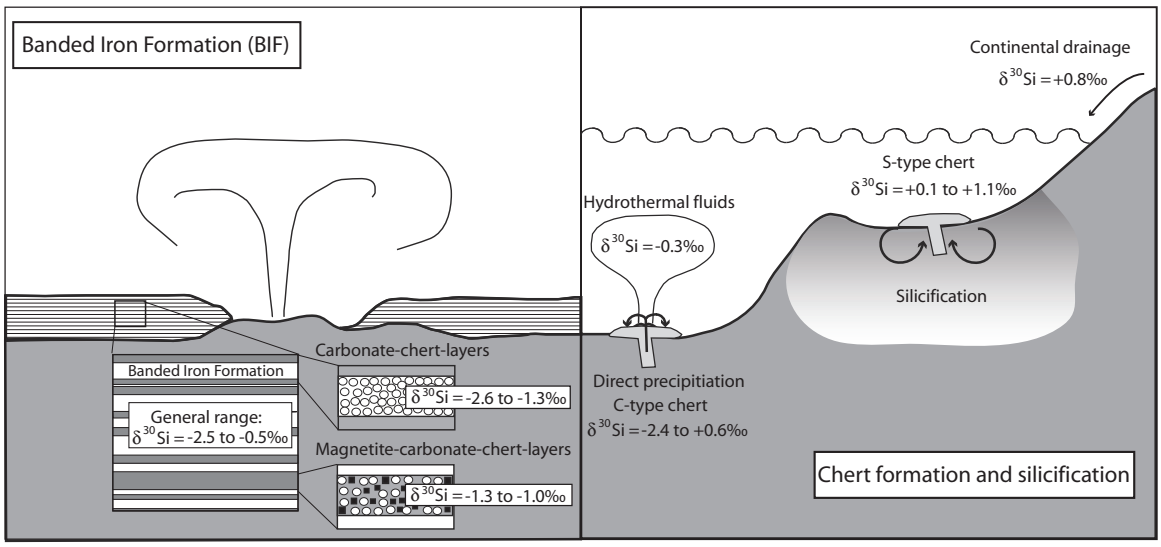

Fig 4: Illustration of the Precambrian superficial silica cycle, showing the presumed reservoirs at this time. Data adapted from André et al., 2006; van den Boorn et al., 2007, 2010 and Steinhoefel et al., 2009.

Futhermore, section III discusses the application of oxygen isotopes in cherts as a direct paleothermometer. In this respect, Robert and Chaussidon (2006) have proposed to use Si isotope record in cherts as an indirect palaeotemperature indicator. Their proposal was based on an isotopic mass balance for the seawater isotope composition. Thereby the Si inputs (alteration of oceanic crust and continents) into the ocean are assumed to be equal to the Si output fluxes. *output 1* (f) describes the precipitation of amorphous silica in sediments, directly from the seawater and *output 2* (1-f) characterizes the hydrothermal silicification of the crust). The fraction of silica of percolating fluids en route to the surface (1-f) depends on the temperature difference between the temperature in the hydrothermal fluid (T_{HYD}) and the temperature in the seawater (T_{SW}). Assuming the T_{HYD} as constant, their mass balance equation describes the seawater temperature dependence on different portions of interacting Si fractions (when (f) is high than (1-f) is low and vice versa), reflecting different δ^{30}Si values in the cherts. In detail, meaning the lower the seawater temperature, the higher the amount of Si sequestered by silicification (1-f) and consequently the higher the ^{30}Si in cherts. Concluding, the observed trend towards higher δ^{30}Si values from 3.5 Ga could therefore be interpreted as reflecting a progressive decrease in ocean temperature of approximately the same order of magnitude as that discerned from the chert δ^{18}O record.

Chapter 4

4. Mass spectrometric analyses of silicon isotopic abundances

4.1. Si sample preparation

All sample preparation steps were carried out in a clean environment. There are two different preparation procedures applied during this thesis, namely *acid attack* and *alkaline attack*.

The former method was used only for the preparation of secondary Si isotope reference materials Diatomite and Big Batch. Thereby about 800 µm silicate powder was directly diluted with HCl (~1 mol l^{-1}) and HF (~2.3 mol l^{-1}). The *acid attack* is described in more details in Cardinal et al., 2003.

The latter method (*alkaline attack*) was applied on both rock samples and standards. 5mg of rock/sample grinded powder was fused with 30mg of $LiBO_2$ flux in covered platinum crucibles at 1000°C for one hour. The major advantage of the alkaline fusion is first that the rock/sample powder is melting at lower temperatures since the solidus curve is lowered by reason of the flux and second that the sample is more easily dissolvable in form of the glassy bed and only weakly acid solutions are needed. After the fusion step, the fusion bead in the crucible was dissolved in double distilled 5% HNO_3 under magnetic stirring overnight.

In order to obtain a pure Si enriched solution, the silicon needs to be separated from the chemical matrix. This purification is essential, because it minimizes the effects of mass bias drift and interferences during MC-ICP-MS analysis (see below). Separation of Si from the ambient medium can be achieved using the triethylamine molybdate method (*TEA-Moly*, De La Rocha et al., 1996). Alternative purification methods involve ion-chromatographic separations of Si, with anion- (Engström et al., 2006) and cation-exchange resins (Georg et al., 2006a; van den Boorn et al., 2006, 2010). During ion exchange chromatography, the stationary phase interacts with analyte ions of opposite charge, so that cation-exchange chromatography retains positively charged cations because the stationary phase is a negatively charged ion and vice versa. Neutrally charged ions are not retained. Dissolved silicon occurs in solution neutrally (H_4SiO_4) or negatively charged (H_3SiO_4). Thus, making Si exchangeable with the anion resin it needs to be converted to a negative charged form SiF_6^{2-}. In this case the silicon is loaded on the anion resin. In contrast, at cation-exchange chromatography the neutrally or negatively charged silicon can be separated by retaining all other positively charged ions of the sample matrix.

The *TEA-Moly* method was applied for this thesis. Thereby Si is separated from an aqueous solution by precipitation as silicomolybdate complexes. Under acidic conditions the ammoniummolybdate tetrahydrate salt forms with the sample silica a silicomolybdic complex $SiMo_{12}O_{40}^{-4}$, which precipitates as a yellow thriethylamine silicomolybdate in the presence TEA hydrochloride (De Freitas et al., 1991). The precipitation is operating best with a Si concentration between 10 µMSi and ~200 µMSi, therefore sample digestion solution was diluted with pure water to about 100µMSi. The volume of *TEA-Moly* reagent is 60 % of the diluted sample volume. The *TEA-Moly* reagent has to be prepared at least few days in advance and must be stored darkly. It is produced by the dissolution of 16g ammonium molybdate and 29.2g thriethlyamoniumchloride with 48 ml of concentrated hydrochloric acid. This intermixture was then filled up to 2 litres with pure water.

After 2 days storing in the dark to allow the reagent in excess to entirely react with Si, the resulting precipitate is insoluble in water and can be separated by filtration through a 0.4µm polycarbonate membrane. Both the membrane and the precipitate are then dried and combusted in Pt crucibles in a furnace at 1000°C in order to remove organic compounds (including membrane) and the excess Mo (De La Rocha et al., 1996). The left over is a white fine-grained powder of cristobalite and tridymite polymorphs (De La Rocha et al., 1996), which was transferred in polypropylene vials and dissolved in dilute suprapur HF-HCl mixture.

Si concentrations were measured twice by inductively coupled plasma atomic emission spectrometry (ICP-AES): first, after the fusion step to check recovery and second after the Si-purification in order to check for the pureness of the silica dissolution regarding other major elements and Mo-contaminants.

ICP-AES analyses were performed on an Iris Advantage (Thermo Jarell Ash Corporation) at the MRAC in Tervuren. ICP-AES is a type of emission spectroscopy that uses the inductively coupled plasma to produce excited atoms and ions that emit electromagnetic radiation at wavelengths characteristic of the electron configuration of a particular element. The intensity of this emission is representative of the concentration of the element within the sample. The internal standards Y and Au are used in order to correct for the instrumental drifts and matrix effects. The blank level is measured in pure water and a blank of alkaline attack. The calibration was performed using pure artificial Si and multi-element artificial solutions (0.1, 0.5, 1, 5 and 10 ppm) and highly diluted natural rock standard materials, prepared by alkaline fusion with the same sample/rock ratio (limestone CCH, shale SGR-1, gabbro JGb-1, granodiorite JG-1a and basalt BHVO).

4.2. Analysis of silicon isotopic abundances

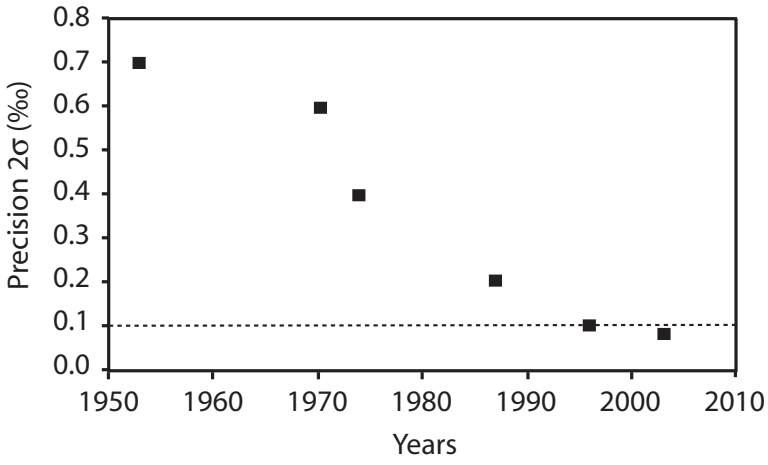

Fig 5: Improvement of the precision for Si isotope analysis in chronological order.

The main topic of this section is to describe the development of silicon isotope analysis. The first mass spectrometric analyses of silicon isotope signatures can be dated back to the 1950's (Reynolds and Verhoogen, 1953; Allenby, 1954; Tilles, 1961). Over a half century, the gas source isotope ratio mass-spectrometry (IRMS) was the predominant technique for silicon isotope measurements, reaching a satisfactory precision in the mid-90's only (0.1 to 0.2 ‰). The common aspect of the preparation method for IRMS analysis is to convert the samples into gaseous SiF_4 previous to the measurement. The beneficial of SiF_4 is its stability under laboratory conditions and no requirements for isotope corrections, since fluorine has only one stable isotope. The SiF_3^+ ion intensities at m/z 85, 86 and 87 are then monitored on the IRMS. The most common methods for SiF_4 preparation are: 1) BaSiF6 decomposition (Reynolds and Verhoogen, 1953), 2) direct fluorination method using F_2 + HF as fluorination reagent (Taylor and Epstein, 1962) and 3) direct fluorination method using BrF_5 as a fluorination reagent (Clayton and Mayeda, 1963). The latter one is the most widely used protocol (Douthitt, 1982; De La Rocha et al., 1996, 2000; Ding et al., 2004, 2005a). The precision (2σ) on IRMS analysis improved during the time from 0.7‰ (Reynolds and Verhoogen, 1953), to 0.6‰ (Epstein and Taylor, 1970) to 0.4‰ (Clayton et al., 1974) and 0.1‰ (De La Rocha et al., 1996). The use of a fluorination line is however very hazardous since Fluor gas is extremely explosive which explains why few laboratories were equipped which such device. Interestingly, Brzezinski et al. (2006) developed a new method which does not require an explosive gas to be measured by IRMS.

Another alternative is the measurement by secondary ion mass spectrometry (SIMS), which allows in-situ analysis on a small spatial scale and without complex sample preparation.

However, measurements with SIMS show limitations in precision 2σ = 0.75‰) Huneke et al. 1983; Zinner et al., 1987; Basile-Doelsch et al., 2005; Robert and Chaussidon, 2006). Thereby the poor precision can be partially counterbalanced by a high number of replicates since measurements are very fast.

The advent of MC-ICP-MS has made analysis of isotope ratios more precise and accurate on comparable low time demands, furthermore the sample preparation with hazardous gases can be avoided. In addition the capability to replicate measurements leads to an increase in precision.

4.3. General concepts of the analysis of silicon isotopes on MC-ICP-MS

The first studies demonstrating that MC-ICP-MS analysis can be applied for silicon isotopes on a Nu Plasma™ instrument were De La Rocha (2002) in wet plasma (2σ = 0.18‰) and Cardinal et al. (2003) in dry plasma (2σ = 0.10‰) conditions. Others followed later (Engström et al., 2006; Georg et al., 2006a; van den Boorn et al., 2006; Chmeleff et al., 2008) on different MC-ICP-MS instruments: Nu 1700, Finnigan Neptune and Nu Plasma™ (Table 1). The method used for Si isotope measurements is a refined method, adapted from the method of Cardinal et al., 2003 developed at the Royal Museum for Central Africa (Tervuren), Belgium and described more in detail in Chapter 4.5.

Author	MC-ICP-MS	External doping	Plasma	Resolution	Si required (µg)	Precision (±1σ)
De La Rocha, 2002	Nu Plasma	–	wet	low	~160	0.09 for $\delta^{29}Si$
Cardinal et al., 2003	Nu Plasma	Mg	dry	low	2	0.04 for $\delta^{29}Si$
Engström et al., 2006	Neptune	Mg	wet	high	20	0.25 for $\delta^{30}Si$
Georg et al., 2006a	Nu 1700	–	dry	high	2	0.07 for $\delta^{30}Si$
Van den Boorn et al., 2006	Neptune	–	dry	medium-high	4	0.18 for $\delta^{30}Si$
Chemeleff et al., 2008	Neptune	–	dry	medium	50	0.12 for $\delta^{30}Si$
This study (Part II)	Nu Plasma	Mg	dry	medium	4	0.07 for $\delta^{30}Si$

Table 1: Detailed listing of the analysis of Si isotopes on a MC-ICP-MS

The most common reference standards used for silicon isotope analyses are NBS-28 (RM#8546), Rose Quartz, and IRMM 018. NBS-28 and Rose Quartz standards consist of quartz sand. The acronym NBS stands for *American national bureau of standards*, the institute changed its name to *National Institute for Standards and Technology* (NIST). IRMM 018 is a silica standard from the *Institute of Reference Materials and Measurements* (IRMM). So far, the published absolute isotope compositions of these standards are not well constrained (Reynolds et al., 2006).

However, the NBS-28 silica sand standard is isotopically homogeneous and certified for oxygen isotope composition and therefore should be used as the primary reference material for Si isotopic measurements (Carignan et al., 2004). The first isotopic compositions on Earth samples (Douthitt, 1982) and most samples before 1982 have been analysed relative to the CalTech Rose Quartz Standard (RQS) and not to the international standard NBS-28. The direct comparison between data reported to RQS and NBS was questioned, since the $\delta^{30}Si$ of RQS has been estimated to have an offset to NBS-28, namely lighter ($\delta^{30}Si = -0.28 \pm 0.18‰$; Molini-Velsko et al., 1986) and heavier ($\delta^{30}Si = +0.24 \pm 0.15‰$; Robert and Chaussidon, 2006). However, it has recently been shown by Georg et al. (2007a) that RQS is isotopically similar to NBS-28 ($\delta^{30}Si$ vs. NBS =-0.02‰), which permits direct comparison of $\delta^{30}Si$ values analysed by both standards.

The precision and accuracy of isotope ratio measurements by plasma source-mass spectrometry techniques are affected by **mass bias** (loss of the lighter isotopes) and **matrix effects** (spectral and non-spectral type):

4.3.1. Mass bias

A significant feature of plasma source mass spectrometry is the large instrumental mass bias (mass discrimination), which can be described in short as "*the mass fractionation introduced by the mass spectrometer*" (Albarède et al., 2004). Mass bias is generated at the plasma interface and the transfer optics and is related to the preferential focusing and transmission of heavier isotopes into the mass spectrometer. Thus lighter isotopes are predominantly lost, resulting in a positive deviation in the measured isotope ratio (higher $^{30}Si/^{28}Si$). A variety of phenomena occur to create mass bias: 1) mass dependent ionization, 2) hydrodynamic entrainment by the expanding Ar atoms in the plasma interface, 3) space-charge effects within the zone of electrical acceleration caused by repulsive forces acting with the ion beam and 4) chromatic aberrations in the electrostatic sector (Albarède et al., 2004). In addition, sample matrix, plasma instability or sample gas flow rate are affecting the instrumental mass bias and handicap the measurement. The mass bias varies with the mass of the element and is for light elements much larger (>15 %/atomic mass unit) due to the higher fractionation potential than for high-mass elements (0.5 to 1.5 %/amu, Rehkämper et al., 2004). In contrast to Thermo Ionization Mass Spectrometry, the amplitude of mass discrimination in ICP-MS is greater, although it is considered to possess better temporal stability, as the sample is introduced continuously into the plasma. In order to obtain precise and accurate analyses, the large mass bias (often more than 10 times greater than the isotopic fractionation of stable isotopes in nature) requires a control during isotope ratio measurements.

Thereby it can be distinguished between ***short-term drift*** and ***long-term drift*** corrections:

Short-term drift correction is applied to overcome the instantaneous mass discrimination. A common procedure for the short-term drift correction of the effects of instrumental mass bias are internal and external normalization, which describe an isotopic normalization by a ratio of either the same or a different element, respectively. However, internal normalization cannot be used in general for stable isotope ratio measurements, because it eliminates both instrumental and natural mass fractionations. A further technique, the double spike technique is inapplicable for silicon isotopes, as well, since the technique can only be applied to elements with four stable isotopes (Albarède and Beard, 2004), e.g. typically Fe isotopes. All procedures have in common that they employ either a linear, power or exponential law correction to overcome the mass bias. The choice among these laws will depend on which law best reproduces the true isotopic composition. Detailed studies of corrections schemes have shown that the power law and particularly the exponential law are preferable for the correction of larger mass fractionation effects (Russell et al., 1978; Wasserburg et al., 1981; Hart and Zindler, 1989). The basic principal of external normalization is that a solution is spiked with an external element, with a known (or constant) isotopic composition, with a molar mass as close as possible to the studied element. The mass bias measured for the element of known isotopic composition can be used to correct the measured isotopic composition of the analyte and determine its true unknown isotopic composition. Cardinal et al. (2003) showed that in case of silicon isotopes, Mg can be used as an external element (the reference standard SRM 980). The Mg concentration is adjusted to allow an intensity ratio Si:Mg ~ 1:1. Si isotope ratios are then corrected employing the exponential mass bias law with a fractionation factor (f_{Mg}) determined from the analyzed $^{25}Mg/^{24}Mg$ ratio:

$$f_{Mg} = \frac{\ln\left[\left(^{25}Mg/^{24}Mg\right)_{true}/\left(^{25}Mg/^{24}Mg\right)_{measured}\right]}{\ln\left[\left(mass\,^{25}Mg\right)/\left(mass\,^{24}Mg\right)\right]}$$

Assuming that the ratio between fractionation of Si and the fractionation of Mg is constant during one analytical session (fSi/fMg = constant), the Si isotopic measurements can be corrected by this equation:

$$\left(^{29}Si/^{28}Si\right)_{true} = \left(^{29}Si/^{28}Si\right)_{meas} \times \left(mass\,^{29}Si / mass\,^{28}Si\right)^{f}$$

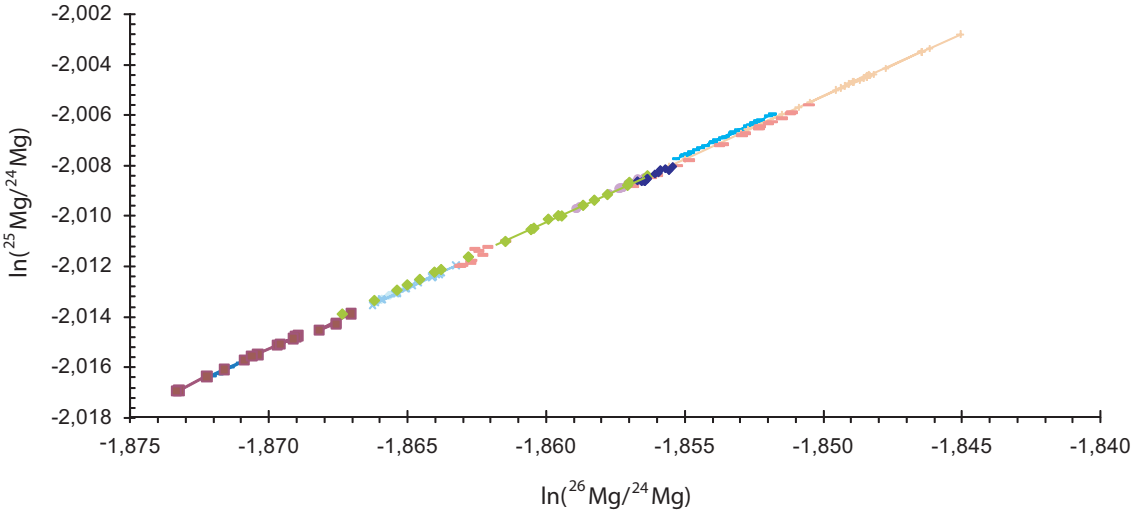

Fig 6. Mass bias fractionation line: Mg vs. Mg isotopes (slope = 0.51; Galy et al., 2001). Different symbols illustrate different analytical sessions.

On an experimental long-term plot, it can be seen that all different analytical sessions (Fig 6, data from the period of October 2008 to June 2009) plot on the mass bias fractionation line with a constant slope of ~0.51, which is very similar to the slope obtained by Galy et al. (2001) of 0.5180 ± 0.0004; n ~ 167. This lies between a pure thermodynamic (0.5210) and kinetic mass-dependent fractionation (0.5105). In a similar way, a mass bias fractionation line for Mg and Si has to be developed for the standards on a daily basis (Fig 7). This mass bias fractionation line indicates that no change of fSi/fMg appears during the day:

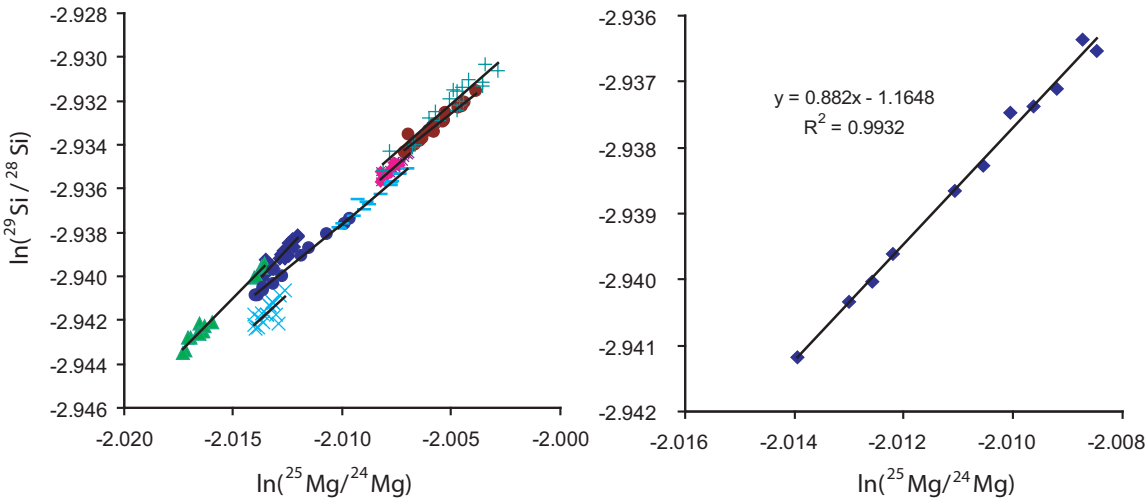

Fig 7. Mass bias fractionation line: Mg vs. Si isotopes (theoretical slope = 0.86); a) Control of the standards on one analytical session. b) Variation of the slope between different analytical sessions.

$$slope = \frac{\ln(Mass^{29}Si / Mass^{28}Si)}{\ln(Mass^{25}Mg / Mass^{24}Mg)} = 0.859$$

The slope can vary from one session to another up to ± 25% (e.g. 0.81 ± 0.03 to 1.08 ± 0.03, Cardinal et al., 2003).

A further implicit requirement is that during analyses of each sample and bracketing standards mass bias is relative stable with same mass bias behaviour.

Long-term drift corrections are used to adjust the long-term drift over time of the isotope ratios. These not-instantaneous changes in mass discrimination are corrected by alternating standard and sample measurements, termed the *standard bracketing method*. Thereby the long-term instrumental mass bias of an unknown sample is interpolated between the biases inferred from two standard runs, one preceding and one following the sample analysis. Advantageous is the fact that standard bracketing partly cuts out the Si blank and interferences, since both impact standard and sample uniformly. This requires that sample and standard solutions yield identical composition (acid content, Si/Mg ratios and sample matrix) and an intensity ratio close to unity. Due to the fact that one sample measurement is enclosed by two standards, delta value is calculated by the mean of the sample relative to each standard.

4.3.2. Matrix effects

Matrix effects can be classified into ***spectral*** (isobaric) and ***non-spectral*** types: The former characterize interferences, whereas the latter are associated with changes in the sensitivity of an analyte due to presence of other elements.

Spectral matrix effects**:** The high ionization efficiency of the ICP causes ionizing of almost every element entering the plasma, which results in mass interferences with the element of interest. The interferences can be divided in: 1) molecular interferences (such as $^{14}N^{16}O^{+}$ at ^{30}Si), 2) elemental isobaric interferences (such as ^{54}Cr at ^{54}Fe) and 3) double charged interferences (such as $^{58}Fe^{2+}$ at ^{29}Si, Table 2). Simply eliminating all the foreign elements by a chemical purification protocol is one way to overcome the interferences (thereby mainly doubly charged species can be removed). But not all interferences are originated from the sample matrix, but emerge as well in the ionization source (compounds of argon, nitrogen and atmospheric gases).

Table 2: List of potential interferences on the Si isotopes (after Engström et al., 2006).

Isotope	Hydrides	Nitrogen based	Carbon based	Doubly charged
^{28}Si		$^{14}N^{14}N^{+}$	$^{12}C^{16}O^{+}$	$^{56}Fe^{2+}$
^{29}Si	$^{28}Si^{1}H^{+}$	$^{14}N^{14}N^{1}H^{+}$	$^{12}C^{16}O^{1}H^{+}$	$^{58}Fe^{2+}$
		$^{15}N^{14}N^{+}$	$^{12}C^{17}O^{+}$	$^{58}Ni^{2+}$
			$^{13}C^{16}O^{+}$	
^{30}Si	$^{29}Si^{1}H^{+}$	$^{14}N^{16}O^{+}$	$^{13}C^{17}O^{+}$	$^{60}Ni^{2+}$
		$^{14}N^{15}N^{1}H^{+}$		
		$^{14}N^{14}N^{2}H^{+}$		

Therefore, another strategy to cope with polyatomic interferences is the use of a desolvating nebulizer, which produces dry plasma with low oxide and hydroxide formation. However, by reason of the use of nitrogen gas in the desolvating system to optimize signal stability and sensitivity or ubiquitous presence of trace N_2, nitrogen-based interferences occur, which overlap significantly with the silicon beams ($^{14}N_2$, the ^{28}Si peak, $^{14}N_2{}^{1}H$, $^{15}N^{14}N$ for the ^{29}Si peak and $^{14}N^{16}O$ for the ^{30}Si peak). Other usual method to suppress polyatomic interferences is the use of collision cells or chemical reaction cells. However, given that both have potential to break Ar-based molecular interferences, which are not overlapping with silicon peaks, they are not in common use for silicon isotope analysis.

The most elegant and straightforward way to overcome the problem of spectral overlap is high mass resolution. The resolution, *R*, of a mass spectrometer is its capability to differentiate between masses and is usually defined as: $R=m/\Delta m$ where m stands for the nominal mass of the first peak and Δm represents the mass difference between two adjacent peaks (Montaser, 1998; Vanhaecke and Moens, 2004), where a higher value of the resolution (R) indicates a better separation of the peaks. The definition for Δm is different for different varying types of resolutions: The 10% valley rule (Fig 8a) said resolution is measured for two neighbouring peaks if their overlap (depth of the "valley" between the two peaks) is at 10% of the peak height (for peaks of equal signal intensity). However, given that in reality the height of the peak is rarely identical, an alternative definition is more useful. The "peak width definition" is applied on a single peak (Fig 8b). Δm is derived from the peak width at the points in the profile that correspond to 5% of the height. In case of pseudo-high resolution (see below) both definitions cannot be applied. Here the resolving power $R(5,95\%) = m/\Delta m^* = m/(m(5\%)-m(95\%))$ is defined as the difference between the masses, where the analyte intensity amounts to 95 % and 5% of maximum signal intensity (Weyer and Schwieters, 2003, Fig 8c). The resolving power exceeds the resolution by a factor of two or more. In order to enhance the mass resolution it is normally necessary to reduce

the width of the ion beam, by mechanically shorten the width of the source entrance slit (in between the accelerating optics and the mass analyzer) and/or of the collector defining slit (in between the mass analyzer and the detector). However, the implementation of high resolution is not achieved without compromise, sensitivity and transmission will decrease as resolution is increased, as well a change in peak shape from flat-topped or trapezoidal into rather triangular.

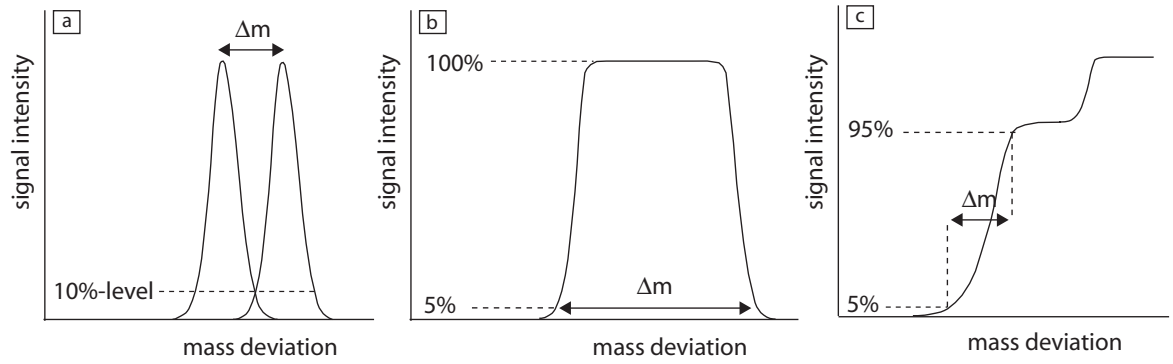

Fig 8: Different calculations of mass resolution: R=m/Δm. a) Definition of Δm by the 10% valley rule applied on two neighbouring peaks with equal signal intensity b) Definition of Δm at full high mass resolution and c) "pseudo" high mass resolution.

At *low resolution* all slits are set to maximum. It is clear that in this mode an isobaric interference cannot be separated from the analyte beam (Fig 9). *True high resolution* can be achieved with a narrow entrance slit and a narrow collector slit. This slit setting leads to the complete resolution of the interferences from the peaks (the peak is separated into two peaks, one analyte peak and the interference). This method is applied when interferences occur on both, high and low mass side. However, at true high resolution the sensitivity and peak shape are mostly poor. Flat-topped peaks are required for precise measurement, given that due to small fluctuations in the mass calibration, magnet field or the ICP source only a small dislocation of the data acquisition point leads to severely affection of the precision, if the peak shape is not flat (Weyer and Schwieters, 2003).

If the interferences occur only on one side of the peak, then *pseudo-high resolution* is the best suitable method. Most interfering species are polyatomic interferences, which are mostly located on the higher mass side of the peak of interest, owning to the systematic of the nuclear mass defect in the low mass range. At *pseudo-high resolution* only a reduction in the source slit is adjusted to give spatially resolved beams at the collector, however, instead of narrowing the collector slit in order to allow only one beam at a time to enter the Faraday cup, the interfering beam is simply clipped on one side of the collector, while the analyte beam is collected. Therefore only one side of the collector slit is used to image the mass

spectrum and so the interference does not enter the collector at the measured mass. A wider collector slit then the ion beam profiles in the focal plane, results in a poorer mass resolution with wider peaks widths in a mass scan (the ion peak appears as one peak, although the mass resolution in the entrance slit is high). Although the two beams are not fully resolved, in this method one side of the peak is free of interfering beams and the flat section of the spectral peak is maximized.

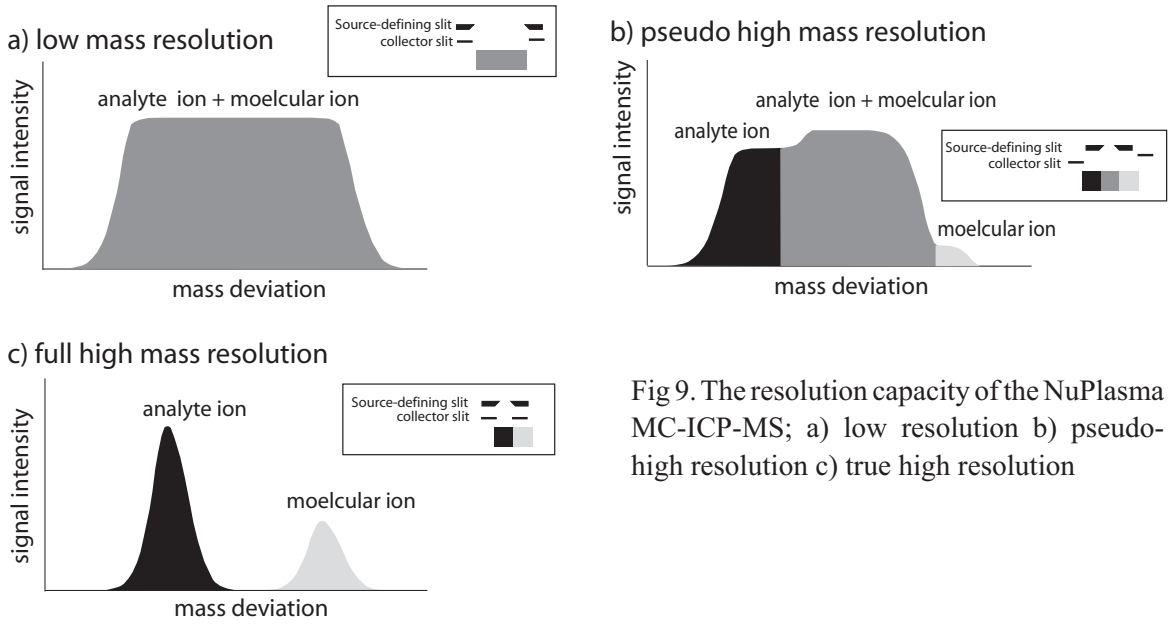

Fig 9. The resolution capacity of the NuPlasma MC-ICP-MS; a) low resolution b) pseudo-high resolution c) true high resolution

The determination of Si isotope ratios via MC-ICP-MS requires high resolution since all three Si beams (^{28}Si, ^{29}Si and ^{30}Si) are affected by polyatomic interferences. The interferences on ^{28}Si and ^{29}Si are less problematic; the most significant interference appears on the ^{30}Si peak. A resolution of R = 1238 is needed to separate $^{14}N^{16}O$ from the ^{30}Si peak (Reed et al., 1994), thus under low resolution only the measurement of $\delta^{29}Si$ was possible on a standard NuPlasma™ (Cardinal et al., 2003; Alleman et al., 2005; Cardinal et al., 2005; André et al., 2006; Opfergelt et al., 2006a, 2006b). On a Finnegan Neptune the analysis of all three isotopes was enabled with pseudo-high resolution (van den Boorn et al., 2006). The Nu 1700 instrument is the only MC-ICP-MS that is able to fully resolve the $^{14}N^{16}O$ interference on ^{30}Si, since it offers a high-resolution capacity. Due to the large geometry, the mass resolution is enhanced from almost 400 to 10,000 and can be set at ~ 2000 for Si isotopes (Georg et al., 2006a). The feasibility to analyze all three stable Si isotopes represents an important improvement in the fractionation behaviour of the silicon isotope record, since e.g. it is possible then to apply a three-isotope plot to check the quality of data; it also improves the sensitivity to differentiate different Si isotopic compositions. Chapter 5 describes how the analysis of $\delta^{30}Si$ on a standard NuPlasma™ was rendering possible under partly true high resolution and partly pseudo-high

resolution, due to an upgrade of the instrument. This method was again refined and analyses are only pseudo-high resolution, like on a Finnigan Neptune.

Non-spectral matrix effects are largely associated with changes in sensitivity and mass bias due to the presence in the solution of third elements (contaminants, acid matrix…) relative to the analyte. This affects the ionization and transmission of the analyte elements, which results in instrumental mass bias and inaccurate values. In order to avoid those matrix effects the purification of the sample solution prior to the mass spectrometric analysis is mandatory as well as the use of same acid content in samples and bracketing standards. For the analysis of silicon isotopes the sample solution was chemically purified during the wet-chemical procedure using TEA-moly co-precipitation (Chapter 4.1). Every Si sample solution was checked by ICP-AES for the purpose of checking that no other contaminant was present in a significant amount (Si to other element ratios >50).

4.4. Major principles of MC-ICP-MS

This chapter is devoted to the fundamental principles of multi-collector inductively coupled plasma mass spectrometer (MC-ICP-MS).

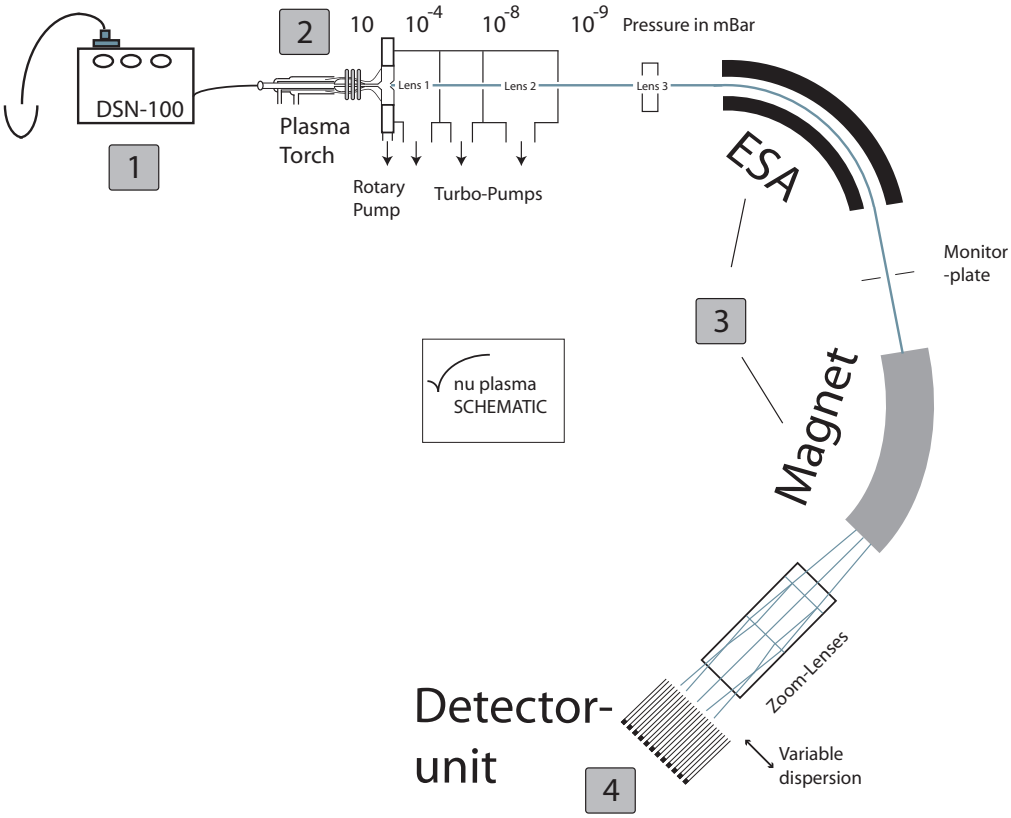

Fig 10. Schematic overview of a Nu Instrument NuPlasma mass spectrometer, with the four main parts, in detail described by Belshaw et al. (1998) and Young et al. (2002).

The MC-ICP-MS device utilised for this thesis is a standard Nu Plasma™ MC-ICP-MS built by Nu instruments (Wrexham, UK), described in details by Belshaw et al. (1998) and Young et al. (2002). The MC-ICP-MS consists of four main parts: 1) the sample-introduction system, 2) the ion source, 3) the mass analyser and 4) the detection unit.

1) The sample is most commonly introduced in liquid form in the introduction system of the MC-ICP-MS system. The general function of the introduction system is to convert the liquid into an ideal aerosol with small particles and narrow (i.e. homogeneous) size distribution that allows complete atomization and ionization in the plasma discharge. The introduction system used for this thesis was the CETAC (Omaha, NE, USA) Aridus™ (I and II) desolvating nebuliser equipped with a PFA (Perfluoroalkoxy) microconcentric nebuliser (Elemental Scientific Inc., Omaha, NE, USA) and a PFA spray chamber (heated to 105°C). In the nebuliser, the liquid is disintegrated into an aerosol by action of the mechanical forces of a gas flow. Thereby the typical running uptake was 100µl min^{-1}. Afterwards the solution is transferred into the spray chamber. The spray chamber´s main functions are 1) heating of the solution, thereby causing the evaporation of the solvent to gain a fine-droplet aerosol and a narrower size distribution and 2) rendering a droplet selection (separate the solvent form the analyte). In the next step, the aerosol emerging from the spray chamber is dried on a heated (160°C) desolvation membrane, which consists of hydrophobic and semi-permeable PTFE Teflon. The desolvation membrane reduces solvent derived oxide, hydride and carbide polyatomic isobaric interferences (H_2O, CO_2, O_2 and N_2). In more details, a counter flow of Argon (sweep gas) assimilates and transports the solvent molecules away from the aerosol. This greatly enhances the sensitivity compared to wet plasma conditions, where the matrix components in the solvent compete for ionisation energy in the plasma (De La Rocha, 2002). Once the aerosol is “in shape” and dried, it is injected through the plasma torch into the plasma, where the ionisation occurs. In spite of potential Si contamination (1-5%), an alumina injector (Glass Expansion™) was utilized.

2) The general function of the ion source is to convert the analyte aerosol into a stream of positively charged ions. Argon is used as an ionization gas since the argon plasma is a highly efficient ionizing source. Essentially, argon can ionize most of the elements of the periodic table that yield an ionization potential smaller than that of argon (15.76 eV).

The inductive coupled plasma is produced as follows: A load coil surrounding the top end of the torch is connected to a radio frequency generator. When RF power is applied on the load coil, high frequency oscillating current induces an intense electromagnetic field, which has a power of about 1300 W. A high voltage ignition spark applied to the gas causes some electrons to be stripped of from their argon atoms. These electrons are accelerated in the magnetic field and collide with other ground state argon atoms. This results in a cascade reaction and leads to the collision induced ionisation of the argon gas. Finally, the argon gas is breaking down into atomized Ar neutral species, positive Ar ions, and electrons, forming the inductively coupled plasma discharge. The Ar plasma is operating at high temperatures of >5000 K. The sample aerosol injected into the plasma experiences different steps of chemical and physical alteration: *desolvation* (dehydration of aqueous material, producing a solid material), *vaporization* (conversion of solid particles into a gas), *atomization* (transformation of the gas into an atom) and *ionization* (production of positively charged ions). After the ions are generated in the plasma, they pass through the interface region. The interface consists of two metallic cones (sampler and skimmer cone, usually made of nickel) with small orifices in the centre. The role of the interface region is to transport the ions from the plasma (atmospheric pressure, 760 Torr), to the mass spectrometer analyzer region (10^{-6} Torr). The drop in pressure creates an expansion of the plasma into the interface region, therefore only about 1 % of the ions actually arrive at the mass analyser. Consequently, the ion beam needs to be steered into the mass analyzer by several focusing optical lenses. In addition the lenses have to maintain the composition and electrical integrity of the ion beam. Thereby the first acceleration potential is about 4kV.

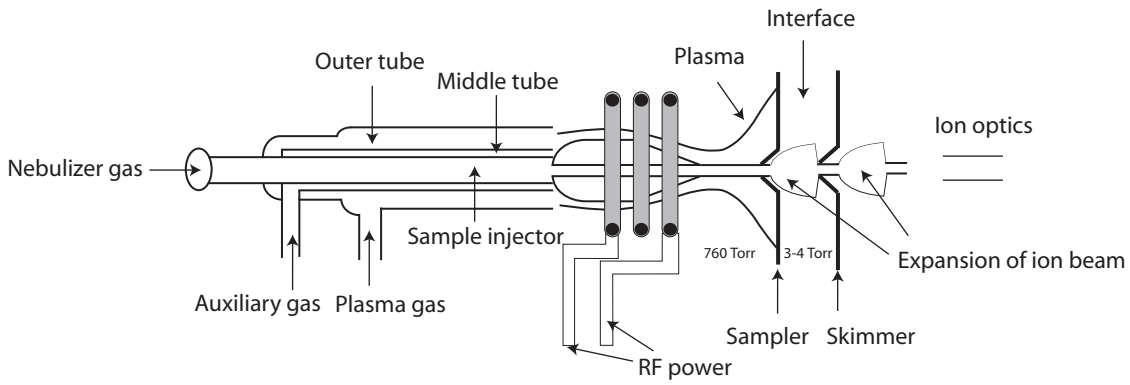

Fig. 11: schematic overview of the plasma interface

3) The mass spectrometer has a forward Nier-Johnson geometry (the electrostatic analyser (ESA) is positioned before the mass separation device). Ions entering the double focusing mass spectrometer yield a broad kinetic distribution (typically 0.5 to 5 eV for the Nu Plasma™) and have to be focused in the ESA in terms of their kinetic energy. Thereby slow ions are more deflected than fast ions. A large energy spread of the ions would lead to different velocities of the ions, meaning that they would use different trajectories, despite same mass to charge ratios. Therefore all ions arriving at the mass analyser need to be corrected for the energy spread and need to have same kinetic energies. The mass separation of the ions is achieved within a magnetic field. The adjacent isotopes are deflected (*Lorenz* force) in a fast scanning laminated magnet due to their m/z ratio (m = mass; z = charge), whereby the faster ions with a low m/z ratio are more deflected than the heavier ions with a high m/z ratio.

4) In a single isotope collector each isotope of interest is measured sequentially in a single fixed detector, by varying the magnetic field strength. The multi-collector enables to measure the isotopes simultaneously in up to sixteen fixed or variable detectors. Given that the ion beam generated by ICP-sources is subject to fluctuations of its intensity and the beam intensity is the direct measure of the analyte concentration, those fluctuations in intensity can limit the precision of the analysis. The simultaneous measurement of a multi-collector arrangement can compensate the intensity fluctuations, because they affect all isotopes simultaneously. The detector array of the Nu Plasma™ consists of 12 fixed sapphire/ceramic Faraday collectors with fixed 2.5 mm spacing between them on the mass focal plane as well as three fixed dynode electron multiplier ion-counting systems. A Faraday cup is a metal conductive cup designed to catch charged particles in vacuum; it contains an electrode at ground potential attached to a resistor. When the ion beam hits the Faraday cup positively charged ions are neutralised by inducing a flow of electrons through the resistor. The resulting current can be measured to determine the number of electrons hitting the cup. In contrast to Faraday cups, electron multipliers are designed to detect lower currents. Contrary to the Finnigan Neptune, where the detectors needs be moved along the focal plane to the position of the ion's trajectory, the Nu Plasma™ yields a variable dispersion zoom optic device, which enables the detectors to remain in fixed positions. In detail, the quadrupole lenses, which are positioned between the magnet and the detector, act as a zoom lens that focuses the ion beam optimally into the

collectors. Si isotopes with an m/z of 28, 29 and 30 are collected in the detector L4, Axial and H5 and Mg isotopes with an m/z of 24, 25 and 26 are analysed in L5, Axial and H6, respectively. Both elements are analysed in dynamic mode meaning that Si isotopes and Mg isotopes are actually not measured simultaneously but with 5' offset (Cardinal et al., 2003).

4.5. Details on silicon isotope analysis following Cardinal et al., 2003 and the new method

The basic concept of the method used for Si isotope measurements was developed by Cardinal et al., 2003. The details about the method and the difference to the method described in section II (Chapter 5) are explained in this section.

Samples are prepared according to the procedure described above and measured in HF/HCl solution matrix. The running concentrations following Cardinal et al. (2003), are around 1 ppm Si and 0.5 ppm Mg. The measurements take place under dry plasma condition and dynamic mode (2 cycles: alternately Si and Mg, with 3 blocks of 20 measurements of 5 seconds each). The sensitivity is about 6 V for 1 ppm ^{28}Si and 0.5 ppm ^{24}Mg. The measurement takes place under low resolution mode; therefore the peak shape is flat-topped. Blank solutions (HCl-HF of 0.7-1.2 mM) are checked between each sample analysis and should yield a signal less than 1% on the measured Si intensity and less than 0.1% on the measured Mg intensity, which is below 50 mV and 5 mV, respectively.

Owing to low resolution mode ($\sim m/\Delta m = 300$), the isobaric interference of $^{14}N^{16}O$ on ^{30}Si can not be resolved. The gas flows are adjusted to minimize the $^{14}N_2$ and $^{14}N_2{}^1H$ interferences on ^{28}Si and ^{29}Si, respectively. The interference should be insignificant relative to the Si signal. For a signal of 6 V on ^{28}Si, a 2-6 mV interference and for a 300 mV signal on ^{29}Si, a 0.5 mV interference have been shown empirically to be negligible, whereas a 5 mV interference relative to the ^{30}Si signal is not insignificant and leads to inaccurate values. No detectable interferences are seen on Mg isotopes. The results are expressed as $\delta^{29}Si$ relative to NBS 28 ($\pm 0.08‰ \pm 2\sigma$). Corrections of instrumental mass bias (long-term and short-term corrections are described in Chapter 4.3.1).

The refined method, fully described in section II, is basically the same than the method of Cardinal et al. (2003), except for:

The dynamic mode of altering Si and Mg measurements is changed from 3 blocks of 20 measurements to 4 blocks of 15 measurements, to gain one peak centring at the beginning of each block on ^{30}Si, as well. Analysis was performed under high resolution (entrance slit at

medium resolution and narrow collector slit with: $m/\Delta m = 1200$). A new vacuum rotary pump was installed (Big 80), causing a better vacuum and partly compensating the loss of sensitivity due to the entrance slit setting at medium resolution. The sample and standard solutions (1.7 to 2.2 ppm Si/ 0.9 to 1.1 ppm Mg) were measured with a sensitivity of ~ 7/2ppm on ^{28}Si with blank acid smaller than 50mV. The results are expressed as $\delta^{30}Si$ vs. NBS28 ± 0.07‰ and $\delta^{29}Si$ vs. NBS28 ± 0.04‰.

Section II

Analytical development of silicon isotopes and the determination of rock reference materials

Chapter 5

δ^{30}Si and δ^{29}Si Determinations on USGS BHVO-1 and BHVO-2 Reference Materials with a New Configuration on a Nu Plasma™ Multi-Collector ICP-MS*

Abstract

We report silicon isotopic determinations for USGS rock reference materials BHVO-1 and BHVO-2 using a Nu Plasma™ multi-collector (MC)-ICP-MS, upgraded with a new adjustable entrance slit, to obtain medium resolution, as well as a stronger primary pump and newly designed sampler and skimmer cones ("B" cones). These settings, combined with the use of collector slits, allowed a resolution to be reached that was sufficient to overcome the $^{14}N^{16}O$ and $^{14}N_2$ interferences overlying the ^{30}Si and the ^{28}Si peaks, respectively, in an earlier set-up. This enabled accurate measurement of both $\delta^{30}Si$ and $\delta^{29}Si$. The δ-value is expressed in per mil variation relative to the NBS 28 quartz reference material. Based on data acquired from numerous sessions spread over a period of six months, we propose a recommended average $\delta^{30}Si$ of -0.33 ± 0.05‰ and -0.29 ± 0.11‰ ($2\sigma_{SEM}$) for BHVO-1 and BHVO-2, respectively. Our BHVO grand mean silicon isotope composition ($\delta^{30}Si$ = -0.31 ± 0.06‰) is significantly more negative than the only published value for BHVO-2, but is in very good agreement with the recently established average value of ocean island basalts (OIB), confirming the conclusion that the OIB reservoir has a distinct isotopic composition from the solar reservoir as sampled by chondrites.

*Adapted from: Abraham, K., Opfergelt, S., Fripiat, F., Cavagna, A-J., de Jong, J.T.M., Foley, S.F. André, L., Cardinal, D. 2008. $\delta^{30}Si$ and $\delta^{29}Si$ Determinations on USGS BHVO-1 and BHVO-2 Reference Materials with a New Configuration on a Nu Plasma Multi-Collector ICP-MS. Geostandards and Geoanalyitcal Research, 32, 193-202.

5.1. Introduction

During the last decade, there has been renewed interest in the measurement of silicon (Si) isotope variations in water and biological samples because of the importance of Si in global biogeochemical cycles through its incorporation in diatoms (e.g., De La Rocha et al., 1998; Varela et al., 2004; Cardinal et al., 2005, 2007; Alleman et al., 2005; Fripiat et al., 2007) and its pathways in plants (Ding et al., 2005b; Opfergelt et al., 2006b). Interest has been recently extended to water-rock interaction and core formation processes focused on various mineral and rock samples: clays (Ziegler et al., 2005a, 2005b), cherts (André et al., 2006, Robert and Chaussidon 2006), silcretes (Basile-Doelsch et al., 2005), metabasalts (André et al., 2006), metasediments (André et al., 2006), and basalts, lherzolites and meteorites (Georg et al., 2007a).

Naturally occurring mass fractionation processes between aquatic dissolved Si and biological/mineral Si-rich phases are generally limited (max. 1.5‰, Alleman et al., 2005; Opfergelt et al., 2006b; Méheut et al., 2007; Georg et al., 2006b, 2007b) producing rather small variations in the relative abundances of the three naturally occurring stable isotopes (^{28}Si, ^{29}Si and ^{30}Si). Improved gas source isotope ratio measurement (IRMS) techniques (Brzezinski et al., 2006) and the advance of MC-ICP-MS now provide the required precision to constrain aquatic and biological systems. This has been confirmed recently by an inter-laboratory Si isotope comparison of three pure silica reference materials (Carignan et al., 2004; Reynolds et al., 2007): (1) IRMM-018 (a SiO_2 reference material); (2) Big Batch (an artificial SiO_2 material) and (3) a diatomite sample (natural opal sample). These comparisons demonstrated that published $\delta^{30}Si$ data can be reliably compared between laboratories within 0.2‰ precision for pure silicon materials.

Chemically more complex specimens such as soils and rocks require appropriate analytical dissolution and elemental separation/purification procedures, which may differ between laboratories. As yet, there are no cross-calibration data available to assess the accuracy of the whole Si isotopic analytical procedure on these matrices. So far only two U.S. Geological Survey (USGS) reference materials AGV-2 (andesite, Oregon) and BHVO-2 (Hawaiian basalts) have been analysed for Si isotopes (van den Boorn et al., 2006). Their $\delta^{30}Si$ measurements (at -0.01 ± 0.24‰ and -0.09 ± 0.31‰, 2σ, respectively) fall outside the 95% confidence intervals of representative rocks from the basaltic rock range of upper mantle lherzolites ($\delta^{30}Si$ = -0.37 ± 0.10‰, n = 4, 2σ, Georg et al., 2007a), terrestrial mafic and ultramafic igneous rocks ($\delta^{30}Si$ = -0.4‰, Douthitt, 1982), ocean island basalts (OIB)

($\delta^{30}Si$ = -0.37 ± 0.14‰, n = 5, 2σ, Georg et al., 2007a) and bulk Iceland basalt value ($\delta^{30}Si$ = -0.35 ± 0.10‰, n = 2, 2σ, Georg et al., 2007b). The compilation with Douthitt Si rock data needs no correction, since the Caltech Rose Quartz reference material is shown to be similar to NBS 28 (Georg et al., 2007a). These differences may reflect either analytical artefacts or natural variations that are known to affect other trace or isotopic ratios in andesitic or basaltic rocks. The first aim of this contribution is to answer this question by providing additional measurements on both BHVO-1 and BHVO-2 OIB reference materials using a different sample preparation and analytical methodology.

One of the largest drawbacks in MC-ICP-MS analysis is the occurrence of interferences of isobaric polyatomic ions, inhibiting correct determination of various elements with m/z < 100, notably Fe and Si. The interferences are mostly molecular species derived from reactions in the plasma and cannot be avoided by chemical purification. In particular, the determination of $\delta^{30}Si$ on a conventional Nu Plasma™ instrument has proved elusive until now because of the insufficient resolution of the $^{14}N^{16}O$ interference overlying the ^{30}Si peak. $\delta^{30}Si$ was calculated from $\delta^{29}Si$ using theoretical multiplying factors based either on kinetic ($\delta^{30}Si=1.96*\delta^{29}Si$) or equilibrium ($\delta^{30}Si=1.93*\delta^{29}Si$) simplified mass-dependent fractionation law, based on an approximation valid for small ranges of isotopic fractionations (Johnson et al., 2004). In order to eliminate these interferences and to obtain high precision measurements, the Nu Plasma™ MC-ICP-MS was upgraded with a new high quality adjustable entrance slit, newly designed B-type cones (as opposed to the regular A-type cones) and a more powerful primary pump. The second objective of this paper is to demonstrate precise and accurate $\delta^{30}Si$ determinations on a conventional Nu Plasma™ instrument in high resolution mode.

5.2. Instrumental

5.2.1. New configuration of the Nu Plasma™ mass spectrometer

The measurements were performed on a Nu Plasma™ MC-ICP-MS (Nu Instruments, Wrexham UK, described in detail by Belshaw et al. (1998)) at the Universite Libre de Bruxelles (Belgium). For $\delta^{30}Si$ determinations our Nu Plasma™ instrument was upgraded with the combination of two sets of adjustable slits (entrance and collector slits), high transmission B cones and a new vacuum rotary pump (BOC Edwards E2M80), in order to accomplish a compromise between complete interference separation, flat-topped peak shape and sufficient signal intensity on all Si stable isotopes: ^{28}Si, ^{29}Si and ^{30}Si.

A newly designed entrance slit was installed in 2006 with three selectable narrower slit settings: 0.3 mm, 0.05 mm and 0.03 mm, corresponding to true low (~ 400 M/ΔM), medium (~ 1500 M/ΔM) and high resolution (~ 3000 M/ΔM). For Si isotope measurements, this slit was set at medium resolution. A higher resolution mode reduced the transmission and overall sensitivity. Contrary to the Nu Plasma™ HR, the Nu Plasma™ instrument used in this study was not equipped with so-called "Alpha" slits, used to reduce beam aberrations, which could cause a blurred peak image at the detector. As an alternative to improve the peak shape, the edge-resolving power was improved by setting the High Voltage 5 lens to 0 V. This led to steeper peak edges and improved peak top flatness. However, sensitivity was further reduced by a factor of approximately 2.

Two collector slits were installed in 2001 on the Nu Plasma™ instrument at ULB in Brussels in front of the L4 and H5 Faraday cups, where respectively ^{28}Si and ^{30}Si are measured. They were used to clip the interfering $^{14}N_2$ and $^{14}N^{16}O$ ion beams from the ^{28}Si and ^{30}Si beams to achieve full separation from the interference and to help peak-centering the instrument in dynamic mode (Figure 1).

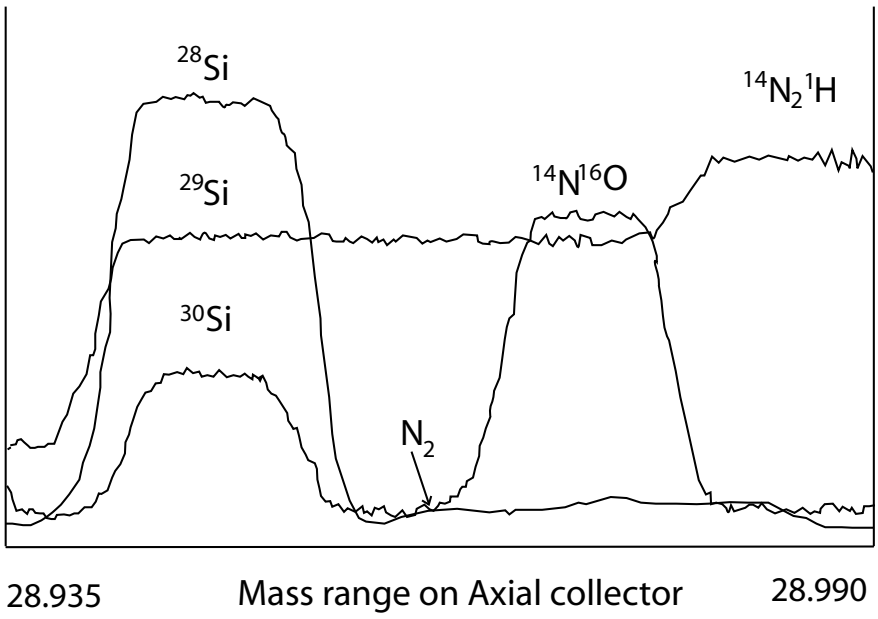

Figure 1. Magnet scan of an acid blank solution. Abscissa characterises the magnet scan mass range on the axial collector. Ordinate indicates signal intensity (different scales per curve, ^{28}Si-peak ~ 17 mV, ^{29}Si-peak ~ 1.4 mV and ^{30}Si-peak ~ 0.8 mV). Interferences were identified by calculation of ΔM (Reed et al., 1994). The ^{29}Si-peak was not separated from its $^{14}N_2{}^1H$ interference due to the absence of a collector slit in front of the axial collector. Given that the analysis is centred on the ^{28}Si or ^{30}Si peak, the measurements of ^{29}Si took place on the interference-free left side of the ^{29}Si-peak. Note that the $^{14}N_2{}^1H$ interference was much higher, as in Cardinal et al., (2003), who report insignificant levels (< 0.1 mV), probably related to the use of the Big80 pump in combination with B-cones, causing a higher transmission of plasma-entrained atmospheric nitrogen into the mass spectrometer.

The data acquisition was done in high resolution mode. The peak centring was performed according to the 10% valley rule on ^{28}Si or ^{30}Si. The source slit was set to give medium resolution, while the collector slit was optimised for each session to give spatially resolved beams on the collector. The interfered parts of the beams were clipped by the collector slits on the high mass end of the peaks. Given that $^{14}N_2$ and $^{14}N^{16}O$ are slightly heavier than ^{28}Si and ^{30}Si and do not enter the detector, this allowed only the analyte beam to enter the Faraday cup. In doing so the signal for each isotope was measured at the mid-point of the analyte peak. This configuration could be used when all interfering species are located at the high-mass side of the peak. As there was no collector slit on the axial Faraday cup where ^{29}Si was measured, this did not allow full separation of analyte and interference peaks (10% valley). This isotope was analysed in the so-called "pseudo-high resolution mode", i.e., the ^{29}Si peak was wider than ^{28}Si and ^{30}Si but measurement was performed on the lower mass side of the peak where no interference was present (Figure 1).

The "Big 80" (BOC Edwards E2M80) vacuum rotary pump with a capacity of 80 m^3 hr^{-1} was installed for a better vacuum in the expansion chamber to improve the transmission and balance the loss of sensitivity related to the medium resolution mode. The Big 80 evacuated the interface region between the sampler and skimmer cones. It improved the vacuum to approximately 1 mbar in comparison to the standard E2M28 rotary pump of 28 m^3 hr^{-1} (2 mbar). Furthermore, higher sensitivity was obtained by running in dry plasma mode using a Cetac Aridus desolvating sample introduction system in combination with B-type cones with a slightly different geometry than regular A-type cones: a B-type skimmer is characterised by a flatter tip and a B-type sample cone by a smaller interior angle compared to the former A-type design. Sample desolvation greatly reduced potential polyatomic isobaric interferences. The sensitivity on Si decreased with increasing resolution and decreasing entrance slit width.

5.2.2. Analytical conditions

The measurements were carried out using the calibrator-sample bracketing technique in dry plasma mode. The isotopic variations were expressed as δ-values in per mil deviation from a reference material (NBS 28 or an in-house reference sample: $pSiO_2$ or Quartz Merck). We applied mass bias correction using external Mg doping and measured Si and Mg in dynamic mode. Typical operation conditions for Si isotope analysis on this instrument are reported in Cardinal et al. (2003) except that a single analysis is now split in four blocks of fifteen runs instead of three blocks of twenty runs (5 second integration). Peak centring was required before each block, as the narrower plateau of ^{28}Si and ^{30}Si in high resolution resulted in an increased sensitivity to magnet drift during the measurement.

In contrast to the low resolution mode (Cardinal et al., 2003), the analyte concentrations were doubled (1.7-2.5 µg ml^{-1} Si, 0.9-1.25 µg ml^{-1} Mg, for an uptake rate of 100 µl min^{-1}) (Table 1) to compensate for the loss of sensitivity in medium resolution mode. Conversely, in order to minimise the use of HF, which induces a loss of Si in the desolvator (Cardinal et al., 2003; Georg et al., 2006a), the HF/HCl content was reduced by a factor of ~ 2 compared to the procedure of Cardinal et al. (2003). Acid molarities of the running solutions were usually in the range of 0.7-1.2 mmol l^{-1} for both HF and HCl. Silicon-rich sample solutions were diluted and spiked with Mg in order to reach approximately a 1:1 voltage intensity ratio (^{28}Si:^{24}Mg) at the mass spectrometer (Cardinal et al., 2003). The Mg/Si intensity ratios ranged between 1.01 and 1.34 and generally did not vary by more than ± 3% between a sample and calibrator. Indeed HF, HCl, Mg and Si contents of the running solutions were adjusted daily and kept constant throughout each analytical session. The δ-values are expressed relative to NBS 28 or with acid attack digested in-house reference samples Quartz Merck and $pSiO_2$. The average values of -0.03 ± 0.06‰ ($\delta^{29}Si$) and -0.04 ± 0.11‰ ($\delta^{30}Si$) for $pSiO_2$ (n = 10, 1σ) and -0.01 ± 0.07‰ ($\delta^{29}Si$) and 0.00 ± 0.03‰ ($\delta^{30}Si$) for Quartz Merck (n = 2, 1σ) confirm that the in-house reference samples measured versus NBS 28 were not significantly different from zero. The $pSiO_2$ was already used and calibrated as an internal in-house reference sample by Cardinal et al. (2003).

Table 1. Operation conditions for Si isotope determination using the MC-ICP-MS Nu Plasma™ instrument

Parameter	**Running conditions**
RF power	1350 W
Acceleration voltage	4 kV
Plasma mode	Dry plasma
Introduction system	Cetac ARIDUS (I) desolvator
Coolant gas flow rate	13 l/min
Auxiliary gas flow rate	0.7 l/min
Nebulizer gas flow rate	0.9 l/min
Nebulizer type	100 µl/min PFA microconcentric nebulizer (ESI)
Aridus sweep gas flow rate	3.5 - 4.0 l/min
PFA Spray chamber temperature	105°C
Membrane temperature	160°C
Running concentrations	Si = 1.7-2.5 ppm, Mg = 0.9-1.25 ppm
Intensity yields	^{28}Si = 5-7 V
Backgrounds on HCl-HF (~1mM) running solutions	^{28}Si ~ 40 mV, ^{24}Mg ~ 5 mV
Washout time	7 minutes
Stabilisation time before analyse	7 minutes
cup configuration	L4(^{28}Si), Ax(^{29}Si), H5(^{30}Si); L5(^{24}Mg), Ax(^{25}Mg)

5.3. Experimental

5.3.1 Reference material preparation

Secondary Si isotope reference materials Diatomite and Big Batch were dissolved using single step HF-HCl dissolution at atmospheric pressure (Cardinal et al., 2003) in order to check the accuracy of the new MC-ICP-MS configuration on these previously inter-compared reference materials (Reynolds et al., 2007). For each aliquot we dissolved about 800 µg silicate powder with HCl (~ 1 mol l^{-1}) - HF (~ 2.3 mol l^{-1}). After dissolution the solution was diluted to reach a ~ 100 µg ml^{-1} Si solution with acid concentrations of ~ 0.05 mol l^{-1} and ~ 0.04 mol l^{-1} for HCl and HF, respectively.

USGS BHVO-1 and BHVO-2 Hawaiian rock reference materials were taken from the same location from the surface layer of a pahoehoe lava that overflowed from the Halemaumau crater in late 1919 (cf. Flanagan et al., 1976). They thus should be considered as two aliquots from the same lava flow. Because the low pressure HF/HCl acid attacks were inefficient in dissolving rock samples, aliquots of BHVO powders were digested using an alkaline flux attack procedure adapted from the techniques proposed by Georg et al. (2006a). The generated glass is easily dissolvable in low concentration acids (Georg et al., 2006a). A series of tests were performed to determine the appropriate flux for the alkaline fusion method. In addition to $LiBO_2$ we tested alternative fluxes like Cs_2CO_3 and Na_2CO_3 for the fusion step, but they resulted in poor yields of recovery of about 60 to 90% and were therefore thought to potentially fractionate the Si isotopes.

Therefore the fusion step was carried out with $LiBO_2$ as the most appropriate flux due to its providing the highest yield (> 98%, see below). About 5 mg of silicate powder was mixed with 30 mg of $LiBO_2$ flux in a platinum crucible. After one hour of melting at 1000 °C, the fusion beads were quickly quenched in 50 ml double distilled 5% HNO_3 (0.8 mol l^{-1}) to inhibit crystallization and avoid potential Si isotope fractionation that might result from such a process. Silicon was purified through its quantitative co-precipitation with triethylaminemolybdate (TEA) (De La Rocha et al., 1996). The pure cristobalite was dissolved with HCl (~ 1 mol l^{-1}) – HF (~ 2.3 mol l^{-1}) solution. The same alkaline procedure was also applied to the diatomite reference material and four quartz Merck aliquots (Table 2) in order to compare results from acid and alkaline attacks.

Table 2. Bulk average isotopic compositions for Diatomite and Big Batch: (1) prepared by acid attack and alkaline fusion (this study) and (2) from the inter-laboratory comparison (Reynolds et al., 2007) and average isotopic composition of Quartz Merck digested by alkaline attack (Quartz Merck is not an inter-laboratory compared reference material in Reynolds et al. (2007)).

Isotope standard	$\delta^{29}Si$ (‰)	st.dev ($1\sigma_{SD}$)	n	$\delta^{30}Si$ (‰)	st.dev ($1\sigma_{SD}$)	n	ratio δ^{30}/δ^{29}
Diatomite							
This study	**0.64**	**0.05**	**24**	**1.25**	**0.07**	**24**	**1.95**
Reynolds *et al.* 2007	**0.64**	**0.07**	**100**	**1.26**	**0.10**	**82**	**1.97**
Big Batch							
This study	**-5.38**	**0.05**	**5**	**-10.53**	**0.07**	**5**	**1.96**
Reynolds *et al.* 2007	**-5.35**	**0.15**	**198**	**-10.48**	**0.27**	**159**	**1.96**
Quartz Merck							
This study	**0.00**	**0.07**	**4**	**-0.01**	**0.12**	**4**	**-**

Standard deviation is expressed as 1σ as for respective literature values. Attention should be paid to the standard deviation of inter-laboratory comparison where variability is also resulting from different laboratories using different methodologies and instrumentation.

All sample preparation steps were carried out in a clean environment. Procedural blanks were prepared for all samples and found to contain non-measurable quantities of Si (with a sample : blank ratio > 350). Concentrations were measured by ICP-AES after fusion to calculate Si recovery (Table 3) and before Si-purification in order to check the absence of major elements and Mo contaminants. Our average calculated yield was 100.9 ± 2.9% (1σ).

5.4. Results

Results for Diatomite and Big Batch secondary reference material are reported in Table 2 and Figure 2. For the silica reference material Diatomite the average delta value of +0.64 ± 0.05‰ and +1.25 ± 0.07‰ (1σ) for $\delta^{29}Si$ and $\delta^{30}Si$, respectively with a $\delta^{30}Si/\delta^{29}Si$ of 1.95 are in good agreement with the recommended values from the recent inter-laboratory comparison (+0.64 ± 0.07‰ and +1.26 ± 0.10‰, 1σ; Reynolds et al., 2007). No significant difference was observed between samples prepared by acid and alkaline attack, including for Quartz Merck showing that the alkaline flux procedure does not introduce any analytical bias relative to those obtained with our previous acid procedure (Cardinal et al., 2003). For the Big Batch reference material, we obtained values of -5.38 ± 0.05‰ ($\delta^{29}Si$, 1σ) and -10.53 ± 0.07‰ ($\delta^{30}Si$, 1σ) with a $\delta^{30}Si/\delta^{29}Si$ of 1.96, which also fits closely with the recommended values (-5.35 ± 0.15‰ and -10.48 ± 0.27‰, 1σ, Reynolds et al., 2007). These accurate results demonstrate clearly the high data quality of the $\delta^{30}Si$ measurements with our new alkaline fusion procedure and the upgraded configuration of the Nu Plasma™ MC-ICP-MS.

Table 3. Delta values, precision and recovery of individual BHVO-1 and BHVO-2 analys

BHVO-1	Date of analysis	δ^{29}Si (‰)	st. error (1σ)	δ^{30}Si (‰)	st. error (1σ)	Recovery (%)
BHVO-1 1	06.07.2006	-0.18	0.03	n.a.	n.a.	102.4%
BHVO-1 3	07.07.2006	-0.25	0.03	n.a.	n.a.	99.3%
BHVO-1 1	23.10.2006	-0.10	0.04	n.a.	n.a.	103.1%
BHVO-1 2	23.10.2006	-0.16	0.04	n.a.	n.a.	98.8%
BHVO-1 b-I	15.01.2007	-0.12	0.04	-0.28	0.06	101.0%
BHVO-1 2	24.02.2007	-0.26	0.03	-0.41	0.05	106.2%
BHVO-1 3	24.02.2007	-0.18	0.03	-0.29	0.06	99.9%
BHVO-1 1	24.02.2007	-0.17	0.04	-0.22	0.05	102.8%
BHVO-1b-II	07.03.2007	-0.20	0.05	-0.37	0.08	103.0%
BHVO-1a-I	09.03.2007	-0.12	0.05	-0.31	0.09	98.0%
BHVO-1a-Li	10.03.2007	-0.17	0.04	-0.41	0.06	105.0%
		δ^{29}Si (‰)	$2\sigma_{SEM}$	δ^{30}Si (‰)	$2\sigma_{SEM}$	Recovery (%)
average	**BHVO-1**	**-0.17**	**0.03**	**-0.33**	**0.05**	**101.8 ± 2.6 (1s)**

BHVO-2	Date of analysis	δ^{29}Si (‰)	st. error (1σ)	δ^{30}Si (‰)	st. error (1σ)	Recovery (%)
BHVO-2 1	24.10.2006	-0.24	0.03	n.a.	n.a.	99.0%
BHVO-2 3	24.10.2006	-0.16	0.04	n.a.	n.a.	102.5%
BHVO-2 2	16.01.2007	-0.11	0.03	-0.17	0.05	99.5%
BHVO-2 3	23.02.2007	-0.10	0.04	-0.22	0.08	95.4%
BHVO-2 1	23.02.2007	-0.15	0.04	-0.19	0.06	102.5%
BHVO-2 1	24.02.2007	-0.23	0.04	-0.44	0.06	102.1%
BHVO-2 2	24.02.2007	-0.26	0.03	-0.47	0.05	95.2%
BHVO-2b-II	09.03.2007	-0.12	0.03	-0.22	0.07	101.0%
		δ^{29}Si (‰)	$2\sigma_{SEM}$	δ^{30}Si (‰)	$2\sigma_{SEM}$	Recovery (%)
average	**BHVO-2**	**-0.17**	**0.04**	**-0.29**	**0.11**	**99.7 ± 2.9 (1s)**

		δ^{29}Si (‰)	$2\sigma_{SEM}$	δ^{30}Si (‰)	$2\sigma_{SEM}$	Recovery (%)
average	**BHVO-total**	**-0.17**	**0.03**	**-0.31**	**0.06**	**100.9 ± 2.9 (1s)**

The recovery noted here was achieved by concentration measurements after the fusion. n.a. stands for not analysed. 1se is the standard error of the mean for each individual analysis. $2\sigma_{SEM}$ represents two times the standard error of the mean of the average values. All data biasing more than $2\sigma_{SEM}$ away from their mean of δ^{29}Si were rejected and are not shown in this table (n = 3 for BHVO-1 and n = 4 for BHVO-2).

The BHVO-1 and BHVO-2 datasets are given in Table 3. The average values of BHVO-1 and BHVO-2 are identical at -0.17 ± 0.03‰ for $\delta^{29}Si$ and -0.33 ± 0.05‰ and -0.29 ± 0.11‰ ($2\sigma_{SEM}$) for $\delta^{30}Si$, respectively. The reproducibility of BHVO measurements is slightly inferior to that obtained for the mono-elemental materials (Diatomite and Big Batch), probably due to the alkaline fusion step, to the purification procedure or to a combination of both, which induces additional variability for samples with more complex matrix. Considering that BHVO-1 and BHVO-2 are derived from the same rock sampled at the same location, we use their grand mean as the representative isotopic composition of the BHVO lava flow (see Table 3). These grand mean values ($\delta^{29}Si$ = -0.17 ± 0.10‰ and $\delta^{30}Si$ = -0.31 ± 0.20‰, 2σ) fall within the error brackets of the previous data on BHVO-2 ($\delta^{29}Si$ = -0.03 ± 0.17‰ (n = 14, 2σ and $\delta^{30}Si$ = -0.09 ± 0.31‰ (n = 14, 2σ) by van den Boorn et al., (2006). Besides, our $\delta^{30}Si$ BHVO estimate is fully consistent with the average value of four Ocean Island Basalt (OIB) samples by Georg et al. (2007a, $\delta^{30}Si$ = -0.37 ± 0.14‰, 2σ). In contrast, it slightly differs from Ziegler et al. (2005b) evaluation of a Hawaiian basalt ($\delta^{30}Si$ = -0.5‰), that relies on a single measurement and cannot thus be used as an actual reference value.

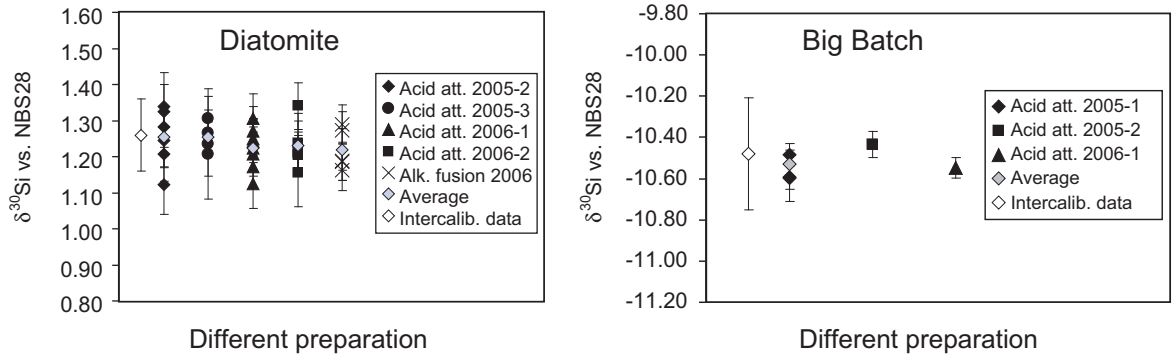

Figure 2. Individual analyses of Diatomite and Big Batch prepared in different years and by different methods (alkaline fusion and acid attack) are indicated by black symbols, with error bars showing $1\sigma_{SEM}$. Open diamonds on the left side of each figure represent the mean of inter-calibrated reference materials (Reynolds et al., 2007); their error bars stand for 1σ. Grey coloured points indicate the average values for each digestion, with error bars representing 1σ. Alkaline attack analysis corresponds to different chemical preparations.

The three-isotope plot shown in Figure 3 on all reference materials Diatomite, BHVO-1, BHVO-2 and Big Batch is an additional way to demonstrate high data quality and the interference-free determination of $\delta^{30}Si$ and $\delta^{29}Si$. The slope of 0.510, mostly driven by the Big Batch set of data, is not significantly different from that in Reynolds et al. (2007) observed on Big Batch, Diatomite and IRMM018 (0.511). This slope is again in close agreement with kinetic fractionation law (0.509), as expected for large isotopic fractionation process such as the one likely to have led to the Big Batch isotopic signature.

5.5. Discussion

Our BHVO grand mean ($\delta^{30}Si$ = -0.31 ± 0.06‰, $2\sigma_{SEM}$) is significantly heavier than the chondritic reservoir ($\delta^{30}Si$ = -0.55 ± 0.08‰, Molini-Velsko et al., 1986; $\delta^{30}Si$ = -0.58 ± 0.06‰, (1σ), Georg et al., 2007a), but is consistent with the average compositions of upper mantle spinel lherzolites, recent OIB basalts (both at -0.37 ± 0.06‰ (1σ), Georg et al., 2007a) and bulk Iceland basalts ($\delta^{30}Si$ = -0.35 ± 0.10‰, 2σ, Georg et al., 2007b).

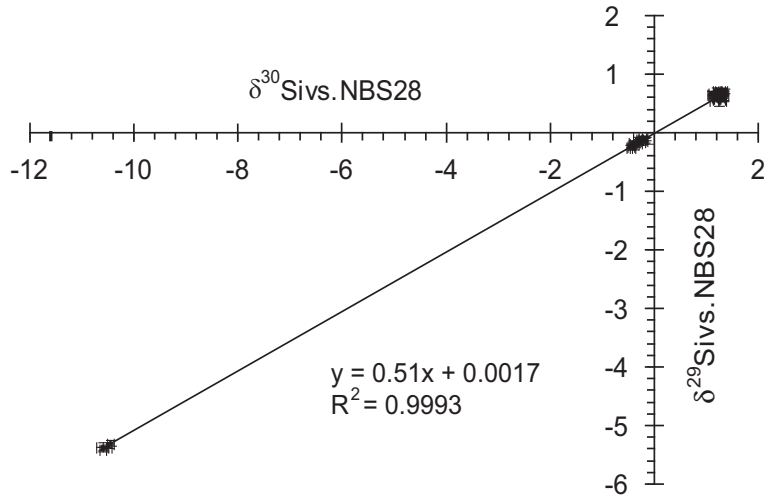

Figure 3. Three isotope plot of $\delta^{29}Si$ versus $\delta^{30}Si$ for all reference materials Diatomite, BHVO-1, BHVO-2 and Big Batch with linear regression line (error bars indicate $1\sigma_{SEM}$). All groups of reference materials fall along a mass dependent line. The best fit line with an intercept of zero has a gradient of 0.510, which is principally controlled by the kinetic fractionation of Big Batch (Reynolds et al., 2007).

Four processes may be invoked to account for the non-chondritic $\delta^{30}Si$ signature within OIBs. First, water-rock interactions may have modified Si isotopic compositions of altered rocks (e.g., Ziegler et al., 2005a, 2005b), which can be discounted considering the lack of any surface weathering on BHVO reference materials (Flanagan et al., 1976). Second, Si-rich rocks from the continental crust and sedimentary components derived from them bear heavier signatures ($\delta^{30}Si$ = -0.07 ± 0.05‰, Douthitt, 1982; Ding et al., 1996; André et al., 2006), indicating that crustal contamination may shift the Si isotopic compositions of basaltic melts towards more positive $\delta^{30}Si$ values. This hypothesis can obviously be disregarded for Hawaii, which lies within an oceanic plate. Third, the BHVO $\delta^{30}Si$ signature might mirror a widespread mantle-derived geochemical feature related to the incorporation of Si as a light element in the core during the early history of the Earth as proposed by Georg et al., (2007a). Finally, the BHVO $\delta^{30}Si$ signature might reflect recycling of old oceanic crust through the mantle. Indeed, much of the trace element and isotopic variability observed in Hawaiian basalts has been attributed to mantle sources that contain various proportions of old (~ 3 Ga) recycled oceanic basaltic crust with or without sediments (e.g., Hofmann, 1986). Because highly silicified early Archaean metabasalts bear heavy Si isotopic compositions ($\delta^{30}Si$ > 0‰, André et al., 2006; Abraham et al., 2007), their recycling through the mantle is a process by which mantle sources with super-chondritic signatures ($\delta^{30}Si$ > -0.55‰) might be generated.

The feasibility of such a scenario may be evaluated through a simple (SiO_2-$\delta^{30}Si$) mass balance using a lherzolitic chondritic mantle with a silica content of ca. 45% m/m and the 3.47 Ga "Barberton Silicified Basalts" (BSB: 70 < SiO2 < 75% m/m, +0.4‰ < $\delta^{30}Si$ < +0.6‰) as the recycled component. With these end-members, the offset of +0.24‰ between the Hawaiian basalts and the chondritic reservoir requires between 13% (for SiO_2 = 75% m/m, $\delta^{30}Si$ = +0.6‰ in BSB) and 28% (for SiO_2 = 70% m/m, $\delta^{30}Si$ = +0.4‰ in BSB). These percentages match well the recent estimates of recycled inputs in the source of Hawaiian basalts (~ 16% m/m, Sobolev et al., 2007). Therefore, Si isotopes might have some potential in tracing early oceanic crust recycling in the source of OIBs. To decipher whether crustal recycling or core formation (or both) is the ultimate cause of the non-chondritic OIB composition will need further detailed examination based on larger Si-isotopic datasets on various basaltic rock populations with improving accuracy and reproducibility. After accurate inter-laboratory calibration, BHVO-1 and BHVO-2 rock reference materials may serve as ideal reference materials to test new appropriate sample preparation procedures and provide insights to answer this question.

5.6. Conclusion

We have demonstrated that accurate and precise $\delta^{30}Si$ data can be acquired on a Nu Plasma™ MC-ICP-MS. A new simple alkaline flux digestion method followed by purification by TEA co-precipitation has been tested successfully on secondary reference materials (Big Batch and Diatomite). This $LiBO_2$ alkaline fusion method seems to be suitable also for chemically more complex samples such as soils and rocks, since it produces consistent and reproducible silicon isotopic signatures. We provide the second silicon isotope characterization of international basaltic rock reference materials, BHVO-1 and BHVO-2. Our $\delta^{30}Si$ values agree with isotope signatures of average Ocean Island Basalts, (Georg et al., 2007a) and fall in the middle of previous Hawaiian basalt estimates by Ziegler et al. (2005b) and van den Boorn et al. (2006). As no certified rock reference material exist so far for silicon isotopic composition, our study is a first step to fill this gap. Further isotopic determinations of the BHVO reference material through inter-calibration should now be carried out.

Section III

Mechanisms controlling Archaean silicification

Chapter 6

Coupled silicon-oxygen isotopic evidences for the origin of silicification in mafic volcanic rocks of the Barberton Greenstone Belt, South Africa*

Abstract

Silica alteration zones and cherts are a conspicuous feature of Archaean greenstone belts worldwide and provide evidence of extensive silica mobilisation in the marine environment of the early Earth. In order to understand the process(es) of silicification and determine the source of silica we measured the silicon and oxygen isotope composition, and major and trace element composition of sections of variably silicified basalts and overlying bedded cherts from the Theespruit, Hooggenoeg and Kromberg Formations of the Barberton Greenstone Belt, South Africa.

$\delta^{30}Si$ and $\delta^{18}O$ values increase with increasing amount of silicification from unsilicified basalts (-0.64‰<$\delta^{30}Si$<-0.01‰ and +8.6‰<$\delta^{18}O$<+11.9‰) to silicified basalts ($\delta^{30}Si$ and $\delta^{18}O$ values as high as +0.81‰ and +15.6‰, respectively). Cherts generally have positive isotope composition (+0.21‰<$\delta^{30}Si$<+1.05‰ and +10.9<$\delta^{18}O$<+17.1), except two cherts, which have negative $\delta^{30}Si$ values, but high $\delta^{18}O$ (up to +19.5‰).

There is a positive correlation between $\delta^{30}Si$ and $\delta^{18}O$ values, with similar gradients for the Hooggenoeg and Kromberg Formation and a different gradient for the Theespruit Formation. The positive $\delta^{30}Si$ values in the cherts and the increase in both $\delta^{30}Si$ and $\delta^{18}O$ during silicification, suggest seawater as the dominant source of silica. The data are consistent with mixing between basalt and chert. Temporal changes in seawater isotope composition, secular changes in seawater temperature or secondary alteration are the possible factors that could account for different gradients of the $\delta^{30}Si$ vs. $\delta^{18}O$ arrays. Our data confirm a secular increase in chert isotope composition. Si isotopes could be applied to better understand the silica precipitation in Archaean quartz veins and provide information about the origin of carbonaceous matter in chert veins.

*Adapted from: Abraham, K., Hofmann, A., Foley, S.F., Cardinal, D., Harris, C., Barth, G.M., André, L. Coupled silicon-oxygen isotopic evidences for the origin of silicification in mafic volcanic rocks of the Barberton Greenstone Belt, South Africa. Submitted to Earth and Planetary Science Letters.

6.1. Introduction

Processes in the hydrosphere of the Archaean Earth may have been very different from the present day. The ubiquity of cherts in 3.5-3.2 Ga greenstone belts shows that silica was extensively precipitated from seawater, probably due to the absence of silica-secreting organisms that maintained Archaean seawater close to silica saturation conditions (Siever, 1992; Treguer et al., 1995). In addition, pervasive silicification of submarine volcanic rocks appears to have been a characteristic feature of the Earth prior to 3.0 Ga (e.g. Duchac and Hanor, 1987; Hanor and Duchac, 1990; Hofmann and Wilson, 2007). Silicification processes are thought to result from percolation of heated seawater that moved in shallow sub-seafloor convection cells, possibly driven by regional high heat flow (Hofmann and Harris, 2008). Investigating the mechanisms of silica precipitation and silicification of volcanic rocks and seafloor sediments in the Eo- and Palaeoarchaean may provide insights not only into seawater-lithosphere interactions on the early Earth, but also into the role of sea-floor hydrothermal activity for the chemical evolution of the early oceans. The mechanism of silica deposition is also relevant for the controversial possibility that cherts are excellent preservation environments for early life on Earth (Schopf, 1993; Pinti et al., 2009), and possibly also on Mars (Farmer and Des Marais, 1999).

Silicon (Si) isotopes may provide a key tool to check the role of the seawater percolation in the Archean silicified lithosphere. Fluid-derived silica-rich precipitates (e.g. Ding et al., 1996; Basile-Doelsch et al., 2005; André et al., 2006; Robert and Chaussidon, 2006; van den Boorn et al., 2007, 2010) as well as secondary minerals formed by weathering (De La Rocha et al., 2000; Ding et al., 2004; Ziegler et al., 2005b; Georg et al., 2006b, 2007b; Delstanche et al., 2009; Opfergelt et al., 2009) are enriched in ^{28}Si, leading to a ^{28}Si depletion of their residual fluids. As a consequence, we should expect that gradual developments of oceanic-derived Si-rich deposits would lead the ocean towards more positive $\delta^{30}Si$ signatures (Robert and Chaussidon, 2006). Mineral precipitation from such an isotopically fractionated ocean should therefore contrast with the rather limited range of $\delta^{30}Si$ variation in mafic and ultramafic igneous rocks ($\delta^{30}Si$=-0.29±0.08‰, Georg et al., 2007a, 2007b; Fitoussi et al., 2009; Savage et al., 2010). In contrast, silica-rich minerals precipitating from a hydrothermal fluid equilibrated with basalt would have a very ^{28}Si-enriched component ($\delta^{30}Si$<-0.29‰). Thus Si isotopic ratios may unravel the contributions of pure hydrothermal ($\delta^{30}Si$<<-0.29‰), basaltic ($\delta^{30}Si$~-0.29‰) and seawater-derived ($\delta^{30}Si$>>-0.29‰) silica.

In addition, Si isotopes are resistant to metamorphic reset (André et al., 2006; Robert and Chaussidon, 2006, van den Boorn et al., 2007, 2010). As Si concentrations are low compared to oxygen (O) in hydrothermal and metamorphic fluids, the Si isotope ratios of

metamorphosed Archaean rocks are more likely to be close to primary magmatic values than are oxygen isotopes. Robert and Chaussidon (2006) used the Si isotope variation in cherts as an indirect palaeotemperature indicator, based on the assumption that seafloor hydrothermal fluids, which precipitate a large fraction of their dissolved Si within altered oceanic crust, have variable $\delta^{30}Si$ values as a function of seawater temperature, resulting in corresponding variation in marine cherts. They observed an increase in $\delta^{30}Si$ values in cherts through time, which, together with a similar rise in chert $\delta^{18}O$ values over the same time span, they ascribed to a decrease in ocean temperatures from ~70°C at 3.5 Ga to present day values. This interpretation was challenged by van den Boorn et al. (2010), who noted that primary and secondary cherts should be distinguished. Cherts that directly formed by chemical precipitation (C-cherts) show the largest spread in $\delta^{30}Si$ (-2.4‰ up to +0.6‰) and their isotopic signature reflect the degree of fractionation of hydrothermal fluids or the degree of mixing with seawater. In contrast, secondary cherts that developed by silicification of volcanogenic sediments (S-cherts) display a more restricted range of $\delta^{30}Si$ (+0.1‰ to +1.1‰), pointing to seawater as the dominant source of silica.

Coupling O and Si isotope values gives us further information about the mechanisms of silicification, because these isotope systems show opposite fractionation behaviour during precipitation of silica, and the amount of oxygen in the fluid remains constant, in contrast to silicon.

We investigated three sections of variably silicified basalt and overlying chert from different stratigraphic units of the Onverwacht Group, Barberton Greenstone Belt (BGB), ranging in age from 3.54 to 3.33 Ga. All sections exhibit a gradual increase in the intensity of silicification within the basalt towards the capping chert. By comparing Si and O isotope variation in these sections, we investigate (1) the relative mobility of Si and O isotopes; (2) the most likely Si sources for silicification; (3) the controlling factors of isotope variation; and (4) the potential of using Si isotopes as a geothermometer.

6.2. Geological background

The supracrustal succession of the BGB is situated in the eastern part of the Kapvaal Craton in South Africa and Swaziland (Brandl et al., 2006; Lowe and Byerly, 2007). The BGB can be divided into three main stratigraphic units, which include 1) the Onverwacht Group, a predominantly volcanic sequence, 2) the Fig Tree Group, a volcaniclastic and fine-grained siliciclastic succession and 3) the Moodies Group composed predominantly of sandstones (Lowe and Byerly, 1999, 2007). The Onverwacht Group consists of submarine ultramafic and mafic volcanic rocks (komatiites, komatiitic basalts, basalts) and minor felsic (dacitic)

volcanic rocks, which are intercalated with thin, silicified sedimentary units, deposited during breaks in volcanic activity. The stratigraphic thickness of the Onverwacht Group ranges from 1 km in the western and northern edge of the belt to more than 10 km in the southern part (Lowe and Byerly, 2007). It can be subdivided into six different units, the Sandspruit, Theespruit, Komati, Hooggenoeg, Kromberg and Mendon Formations. Metamorphic grade is mainly greenschist facies, but reaches amphibolite facies in the Sandspruit and Theespruit Formations (Lowe and Byerly, 1999).

We have investigated three sections of variably silicified rocks with overlying chert horizon from the 1) Theespruit Formation, 2) Hooggenoeg Formation and 3) Kromberg Formation. Silicification is accompanied by a change in the mineral assemblage. With increasing silicification, the paragenesis changes from an amphibole-garnet paragenesis (Theespruit Formation) or an epidote-chlorite paragenesis (Kromberg and Hooggenoeg Formation) to an assemblage dominated by quartz, carbonates and sericite. Detailed descriptions of these sections are provided in Hofmann and Bolhar (2007) and Hofmann and Harris (2008).

6.2.1. Investigated samples and petrography

6.2.1.1. Theespruit Formation (3.54 Ga)

The Theespruit Formation is made up largely of metamorphosed komatiitic basalt, basalt, and sericitic and aluminous rocks representing silicified felsic volcanic and volcaniclastic-epiclastic rocks. The felsic units are commonly associated with thin layers of carbonaceous chert. Theespruit felsic schists in the Steynsdorp Anticline have been dated at 3547 Ma by zircon $^{207}Pb/^{206}Pb$ evaporation (Kröner et al., 1996) and thus represent the oldest supracrustal rocks of the Barberton belt.

The section investigated for this study is from NE of Tjakastadt. It is composed of intercalated pillow and massive basalts, which are more strongly silicified towards overlying felsic schist. The basalts contrast with those of the other two formations investigated in that they are more strongly foliated and more strongly metamorphosed, as garnet porphyroblasts are locally present in the silicified pillow basalts. Diener et al. (2005) reported P-T conditions of 7.4±1.0 kbar and 560±20 ºC for rocks of this area. Overlying the basalts are siliceous felsic schists that are intercalated by discontinuous thin layers of carbonaceous chert. The felsic schists are strongly silicified cherty rocks that consist of silicified felsic agglomerates in low strain domains and, locally, conglomerates. Massive, unsilicified komatiitic basalt overlies the felsic schists.

6.2.1.2. Hooggenoeg Formation (3.45 Ga)

The Hooggenoeg Formation can be subdivided into several stratigraphic units (H2 to H5), denoted with "v" or "c", representing a volcanic interval (H2v-H5v) or a capping chert horizon (H2c-H5c), respectively (Lowe and Byerly, 1999). We investigated the uppermost section of basalt of the Hooggenoeg Formation from the east limb of the Onverwacht Anticline. Section H5 consists of a few hundred metres thick succession of undeformed variolitic pillow and massive basalts (H5v) that are silicified immediately below a thin horizon of strongly silicified sedimentary rock referred to as chert horizon H5c. A network of black carbonaceous chert veins transects the uppermost 5 metres of the volcanic sequence. Remains of purported microfossils have been reported from one of these veins (Glikson et al., 2008). The contact between basalt and bedded chert is sharp and planar with no evidence of tectonic movement. The chert unit is about 1 m thick and consists of three different types of silicified sediments (from base to top): green chert (silicified vitric tuff with glass shards), massive black chert (silicified carbonaceous sediment) and green chert (silicified ash with accretionary lapilli).

6.2.1.3. Kromberg Formation (3.33 Ga)

The Kromberg Formation is well exposed on the west limb of the Onverwacht anticline, where it has been subdivided into three informal members (Lowe and Byerly, 1999), the Buck Reef Chert (K1), mafic lapilli tuff and lapillistone (K2) and tholeitic basalt (K3). The section investigated for this work is situated in the central part of the BGB at the top of the Kromberg Formation (K3). A sequence of variably silicified pillow basalts is intercalated and capped by banded carbonaceous chert (K3c of Lowe and Byerly, 1999) that forms two laterally traceable horizons, the upper one of which has been dated at 3.33 Ga (Byerly et al., 1996).

The volcanic succession consists of pillow basalt, of which the uppermost 50m is silicified. The pillow basalt is locally slightly foliated and commonly variolitic. In the uppermost few meters of the section, translucent chert forms anastomosing veins and voids in pillows. Basalt is overlain by a black and white banded chert and a finely laminated black chert, representing the upper boundary of the first part of the section. Above this, there is a further zone of strongly silicified pillow and massive basalts and overlying black/white banded chert horizon. Hence two cycles of silicified basalts and overlying cherts were studied in the same section.

6.3. Analytical methods and chemical preparation techniques

Major and trace element as well as oxygen isotope data of most of the rocks are described in Hofmann and Harris (2008). In order to complete the data set, additional samples were investigated. Samples from Hofmann and Harris (2008) were re-analysed for major and trace elements on rock powders crushed at the University of Mainz by tungsten carbide instead of agate mills to avoid silicon contamination (see Fig 1S. and Table 1S in supplementary information).

6.3.1. Silicon isotopes

The samples were crushed using a tungsten-carbide grinding bowl. Powder was dried in an oven overnight at 100°C. About 5 mg of the rock powder were dissolved in a clean laboratory environment using alkaline attack ($LiBO_2$ flux, Abraham et al., 2008). Silicon was then purified through its quantitative co-precipitation with triethylamine-molybdate (De La Rocha et al., 1996). The precipitate was then dried and combusted in Pt crucibles in a furnace at 1000°C. The residue was a pure powder of cristobalite and tridymite (De La Rocha et al., 1996), which was transferred to polypropylene vials and dissolved in dilute Suprapur HF-HCl mixture.

We analysed silicon isotopes using a Nu Plasma™ MC-ICP-MS (Nu Instruments, Wrexham UK, Belshaw et al., 1998) at the Université Libre de Bruxelles (Belgium). Silicon isotopes are expressed by the conventional δ-notation in per mil (‰) deviation from a reference. Data were reported relative to in-house standards ($pSiO_2$ or Quartz Merck), which are isotopically similar (Abraham et al., 2008) to NBS28 (National Institute of Standard and Technology RM #8546), the reference standard for silicon isotopes (Carignan et al., 2004). Mass bias was corrected for by a standard-sample bracketing protocol, using external Mg doping in dynamic mode (Cardinal et al., 2003), but slightly modified to allow measurement of both $\delta^{30}Si$ and $\delta^{29}Si$ (Abraham et al., 2008). Accuracy of Si isotope values was checked using the Diatomite standard that was confirmed by an inter-laboratory comparison exercise on secondary reference materials (Reynolds et al., 2007).

All $\delta^{30}Si$ and $\delta^{29}Si$ data fall along the mass-dependent terrestrial fractionation lines of Si (R^2=0.98, Fig. 2 in supplementary information) describing either kinetic ($\delta^{29}Si=0.5092*\delta^{30}Si$) or, for equilibrium ($\delta^{29}Si=0.5178*\delta^{30}Si$) fractionations which are indistinguishable at such low degrees of fractionation (Young et al., 2002). This $\delta^{30}Si$-$\delta^{29}Si$ correlation demonstrates the quality of the isotopic determinations. The complete data set of $\delta^{30}Si$ is presented in Table 1 along with $\delta^{18}O$ and SiO_2 concentrations.

Table 1: Average δ^{30}Si-values of the chemical and analytical replicates and standard deviation ($2\sigma_{SD}$) in conjunction with SiO_2, depth and δ^{18}O.

KROMBERG					Average		2 std.
Sample	Description	SiO_2 (%)	Depth (m)	δ^{18}O (‰)	δ^{30}Si (‰)	n	deviation (‰)[a]
AK15	banded bl/w chert	96.4	2	15.4	0.55	2	0.09
AK12*	sil. pb.	87.5	-0.7	15.3	0.81	2	0.02
AK4	bl. chert-vein	97.9	-2	15.1	0.40	2	0.03
AK3*	sil. pb.	84.8	-10	15.6	0.63	2	0.04
AK13	bl. chert-vein	97.9	-12	16.2	0.40	2	0.13
AK2	bl. chert, finely laminated	100.1	-29	19.5	-0.15	2	0.02
AK14	banded bl/w chert	98.0	-25	16.5	-0.35	2	0.03
AK7*	sil. pb.	84.8	-32	15.1	0.74	2	0.04
AK11*	sil. pb.	81.2	-46	15.6	0.65	2	0.02
AK1*	sil. pb.	76.8	-64	10.0	-0.22	2	0.06
AK10*	unsil. pb.	51.9	-131	11.9	-0.21	3	0.07
average							**0.05**

HOOGGENOEG					Average		2 std.
Sample	Description	SiO_2 (%)	Depth (m)	δ^{18}O (‰)	δ^{30}Si (‰)	n	deviation (‰)[a]
H3B	gr. chert (lapilli)	92.3	0.7	16.7	1.05	2	0.10
H2B	bl. chert	97.1	0.5	17.0	0.80	2	0.05
AH14	gr. chert (glass shards)	90.1	0.2	15.8	0.60	2	0.15
H1B	bl. chert-vein	98.5	-1	17.1	0.48	3	0.11
AH15	bl. chert-vein	98.9	-2	16.4	0.50	3	0.08
AH13*	sil. pb.	70.3	-1.5	14.9	0.41	2	0.03
AH16	sil. b.	76.3	-5	15.6	0.60	3	0.12
AH12*	sil. mb.	74.8	-7	15.4	0.62	2	0.02
AH11*	sil. pb.	73.4	-19	14.3	0.39	2	0.01
AH18*	sil. pb. center	54.7	-30	12.2	-0.02	2	0.05
AH18R	sil. pb. rim	46.6	-30	12.3	-0.07	2	0.10
AH10*	unsil. pb. center	43.1	-60	9.0	-0.44	2	0.05
AH10R	unsil. pb. rim	39.7	-60	8.6	-0.64	2	0.01
AH17*	unsil. pb. center	50.9	-150	9.4	-0.24	3	0.12
AH17R	unsil. pb. rim	53.1	-150	9.6	-0.41	2	0.08
average							**0.07**

THEESPRUIT					Average		2 std.
Sample	Description	SiO_2 (%)	Depth (m)	δ^{18}O (‰)	δ^{30}Si (‰)	n	deviation (‰)[a]
AT1*	mafic schist, unsil. mb.	47.6	16	8.8	-0.06	2	0.07
AT2*	felsic schist	76.3	12.5	10.9	0.29	2	0.14
AT3	carb chert/shale	89.3	13	11.6	0.30	3	0.02
TS2	carb shale	90.7	3	12.0	0.21	2	0.07
AT4*	felsic schist	93.9	2	12.0	0.81	2	0.09
AT5R	sil. pb., sheared	84.1	-1	11.9	0.39	4	0.12
AT5M*	sil. pb., sheared	76.0	-1	11.9	0.46	2	0.07
AT6*	sil. pb., sheared	58.9	-5	10.8	0.23	2	0.03
AT7*	mafic schist, unsil. mb.	47.8	-18	9.9	-0.33	2	0.06
AT8*	unsil. pb.	50.2	-30	10.4	-0.01	2	0.10
AT9*	unsil. mb.	48.9	-55	8.9	-0.299	3	0.10
average							**0.08**
average all							**0.07**

[a]Abbreviations: bl = black; w = white; sil = silicified; pb = pillow basalt; unsil = unsilicified, gr = green; b = basalt; mb = massive basalt. “n” stands for the number of chemical and analytical Si isotope replicates.

[b] “a“ denotes the standard deviation between the chemical and analytical replicates.

[c] “R“ stands for rim and “*” is labelling the samples described in Hofmann and Harris, 2008.

All samples have been at least fully duplicated (including different aliquots, chemical separation and spectrometric determinations); they display an average reproducibility for $\delta^{30}Si$ of 0.07 ‰ ($2\sigma_{SD}$; SD=Standard deviation, Table 1).

6.3.2. Oxygen isotopes

Oxygen isotopes were analyzed at the University of Cape Town (UCT), South Africa and are expressed by the δ-notation in per mil (‰) deviation from SMOW. The NBS28 standard was analysed with every batch of samples and the raw data were normalized to the SMOW scale using the value of 9.64‰ for NBS28 recommended by Coplen et al. (1983). Based on the reproducibility of NBS28 analyses, the typical error on a $\delta^{18}O$ determination is ± 0.1‰ (1σ). Oxygen isotope compositions of silicate whole rocks were determined using conventional extraction methods after reaction with ClF_3 (Hofmann and Harris, 2008). The O_2 was converted to CO_2 using a hot platinised carbon rod. Isotope ratios were measured using a Finnigan MAT Delta XP mass spectrometer. Further details of the methods employed for the extraction of oxygen from silicates are given by Harris et al. (2000). The results of oxygen isotope analysis are reported in Table 1.

6.4. Results

6.4.1. Major and trace elements

The major and trace element data are presented in Table S1 of the supplementary material. The increase in SiO_2 content is the most significant change in major element concentrations with depth below the capping cherts. The basalt sections show compositional changes typical for silicification as reported by Duchac and Hanor (1987) and Hofmann and Harris (2008): Silicification led to a decrease in Fe_2O_3, MgO, MnO and Na_2O contents and an increase in K_2O contents. The contents of immobile element oxides P_2O_5, Al_2O_3 and TiO_2 show slight, but no systematic changes. The transition metals are variably depleted in the silicified basalts. The depletion is greatest for Cu and Zn. The HFSE were mostly immobile. The LIL-elements Rb and Ba were enriched whereas Sr was depleted during silicification. Constant ratios of Al_2O_3/TiO_2 and P_2O_5/TiO_2 for samples of each section indicate that the basaltic rocks are derived from compositionally similar lavas.

Overlying and cross-cutting cherts have by far the highest SiO_2 contents. Archaean cherts may have different origins including chemical precipitates and silicified volcaniclastic, siliciclastic and organic sediments (e.g. Hofmann and Bolhar, 2007). Diagnostic for detrital components are high Al_2O_3 and TiO_2 concentrations. High Zr concentrations would be expected for silicified felsic sediments, whereas high Cr contents would indicate mafic/

ultramafic detritus. The best discriminant between chemical and volcaniclastic sediments is the presence of (volcani)clastic grains. For example, the green cherts from the Hooggenoeg Formation contain volcanic debris including lapilli, accretionary lapilli and glass shards, suggesting a volcaniclastic sediment precursor. Vein-cherts contain relatively small amounts of Al_2O_3 and Zr, indicating a relatively high proportion of pure chemical precipitate.

PAAS-normalized (Post-Archaean Australian Shales, Taylor and McLennan, 1985) REE+Y (Rare Earth Element plus Yttrium) patterns of all samples are shown in Fig. 2S in the supplementary information. Most samples show a positive Eu anomaly and depletion in LREE relative to MREE. The general tendency for the most SiO_2-rich samples to have the lowest REE abundances is a simple dilution effect. HREE were depleted relative to the LREE with increasing silicification, resulting in higher (La_{SN}/Yb_{SN}). The absence of Y/Ho anomalies further indicates that the cherts represent silicified sedimentary rocks (referred as S-cherts by van den Boorn et al., 2007; 2010) rather than chemical precipitates from a silica rich fluid (C-cherts). Further details about the major and trace element variation are described in Hofmann and Harris (2008).

6.4.2. Stable isotope variations

$\delta^{30}Si$ and $\delta^{18}O$ values are presented in Table 1 and in stratigraphic columns of the studied sections (Fig. 1). Our $\delta^{30}Si$ and $\delta^{18}O$ data are compared with those of terrestrial reservoirs in Figure 2.

6.4.2.1. Silicon stable isotope variations

$\delta^{30}Si$ values of unsilicified basalts in all three formations (-0.64‰ to -0.01‰, mean=-0.29‰) are similar to those of recent basaltic rocks and peridotites (see Fig. 2 for references), and their mean (-0.29‰) falls close to estimates of the Bulk Silicate Earth (BSE) Si isotopic composition ($\delta^{30}Si$=-0.28±0.06‰, Fitoussi et al., 2009; $\delta^{30}Si$=-0.29±0.08‰, Savage et al., 2010). Compared to pillow centres, rims demonstrate enrichment in ^{30}Si (average $\Delta^{30}Si$=+0.13‰), and variable SiO_2 contents but the two factors are not correlated. It should be pointed out that most of these differences between pillow centres and rims are within the analytical uncertainty and may be fortuitous. The $\delta^{30}Si$ values for silicified basalts (-0.22‰ to +0.81‰, mean=+0.40‰) shift towards more positive values in all three sections with increasing grade of silicification (Figs. 1 and 2).

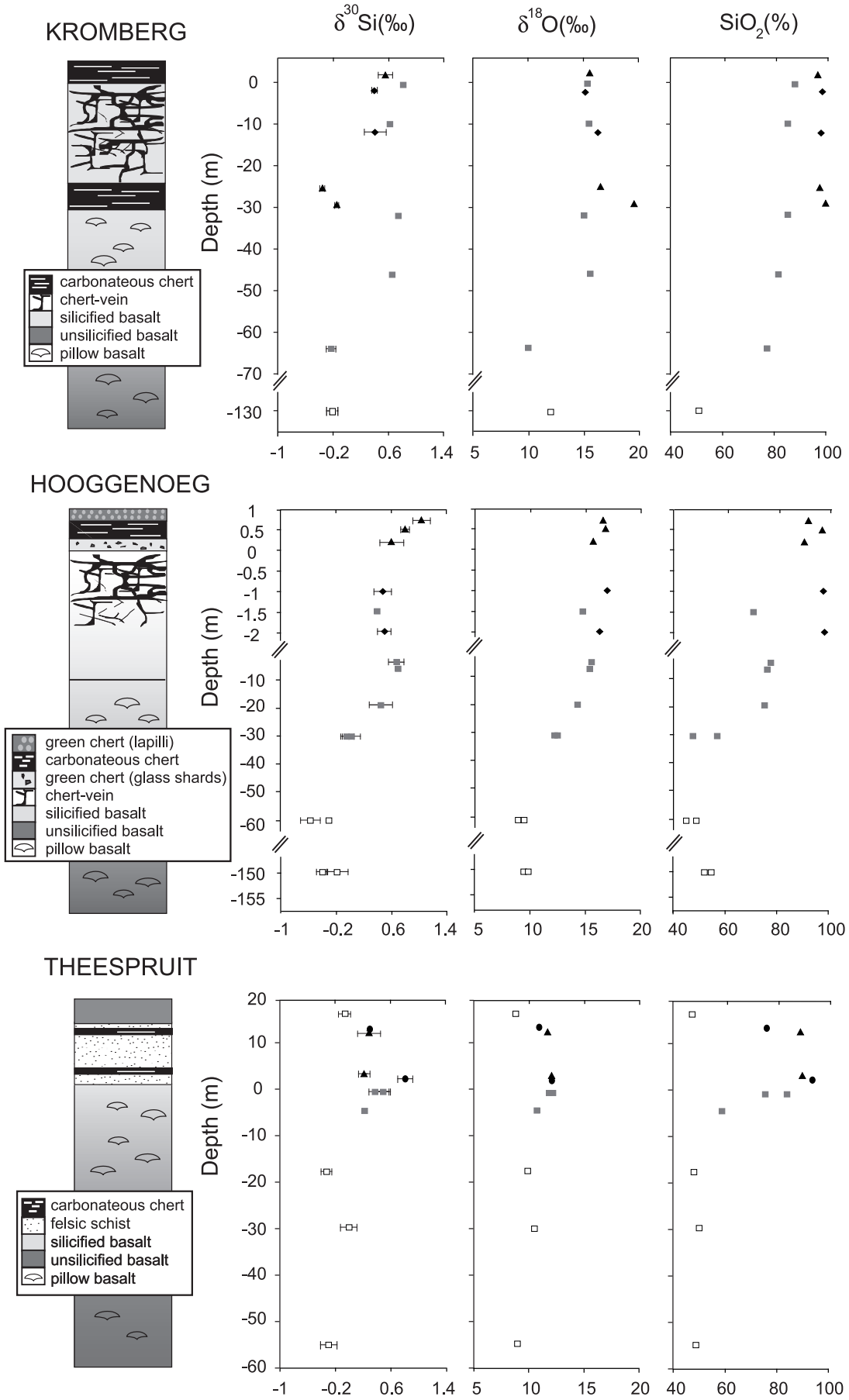
KROMBERG
δ30Si(‰)
δ18O(‰)
SiO2(%)
Depth (m)
carbonateous chert
chert-vein
silicified basalt
unsilicified basalt
pillow basalt
HOOGGENOEG
green chert (lapilli)
carbonateous chert
green chert (glass shards)
chert-vein
silicified basalt
unsilicified basalt
pillow basalt
THEESPRUIT
carbonateous chert
felsic schist
silicified basalt
unsilicified basalt
pillow basalt

Fig. 1: $\delta^{30}Si$ and $\delta^{18}O$ values and SiO_2 plotted against stratigraphic height for the Kromberg, Hooggenoeg and Theespruit Formations. The image on the left shows the schematic stratigraphy of the sections investigated. Symbols refer to rock types: unsilicified basalts (open squares), silicified basalts (grey squares), cherts (black triangles), chert veins (black diamonds) and felsic schists (black circles). All sections show a change to higher $\delta^{30}Si$ and $\delta^{18}O$ with increasing grade of silicification (SiO_2 concentration). Error bar on $\delta^{30}Si$ represents the standard deviation between the replicates. Error bar of the oxygen isotopes characterize the standard error (~0.1‰) and are smaller than symbol size.

All but two cherts and all silicified felsic schists have ^{28}Si-depleted signatures (+0.21‰ to +1.05‰, mean=+0.53‰) and bear close resemblance to the Si isotope values of the silicified volcanogenic sediments (S-type cherts), which have been interpreted to contain silica derived from$\delta^{30}Si$-enriched seawater (cf. van den Boorn et al., 2007; 2010, see Fig. 2). Additionally, chondritic Y/Ho ratios (~26), small Eu anomalies (0.8-2.8, average: 1.6) and high Al_2O_3 contents are typical for cherts formed by silicification of sedimentary or volcaniclastic material (see Fig. 1S and Table 1S in supplementary material). The cherts have $\delta^{30}Si$ values (-0.58‰ to +1.95‰) in the middle of the range obtained by Robert and Chaussidon (2006) for Barberton cherts. However, the chert $\delta^{30}Si$ values are significantly higher than those in metacherts from Isua (-1.99‰ to -0.25‰, André et al., 2006) and cherts associated with Banded Iron Formations (BIFs; Ding et al., 1996; Steinhoefel et al., 2009). Two cherts with negative $\delta^{30}Si$ were found in the Kromberg Formation. This signature and their low Al_2O_3-contents characteristic point to a relatively pure chemical precipitate (C-type cherts; cf. van den Boorn et al., 2007, 2010; $\delta^{30}Si$ of -2.4‰ to +0.6‰) although they lack a positive Y/Ho anomaly characteristic for marine chemical precipitates (Bolhar et al., 2004). Vein cherts resemble isotopically silicified basalts (+0.48‰<$\delta^{30}Si$<+0.50), although they have much higher SiO_2 contents.

6.4.2.2. Oxygen stable isotope variations

There is an increase in $\delta^{18}O$ value from unsilicified basalt (+8.6‰ to +11.9‰; mean=+9.6‰) to silicified basalt (+10.0‰ to +15.6‰; mean=+13.6‰), and to chert (+10.9‰ to +17.1‰; mean=+14.7‰). The unsilicified rocks have slightly higher $\delta^{18}O$ values than a suite of variably altered mafic and ultramafic samples from the Onverwacht Group (Hoffman et al., 1986; group B, +5.5‰ to +8.4‰). Isotopic studies of Archaean komatiites and their primary magmatic minerals from Quebec (Canada), Western Australia and the Barberton Greenstone Belt yielded $\delta^{18}O$ values that are not very different from those of modern mantle-derived mafic magmas ($\delta^{18}O$= +5.6‰ to +6.0‰, Beaty and Taylor, 1982; Smith et al., 1984, Fig. 2).

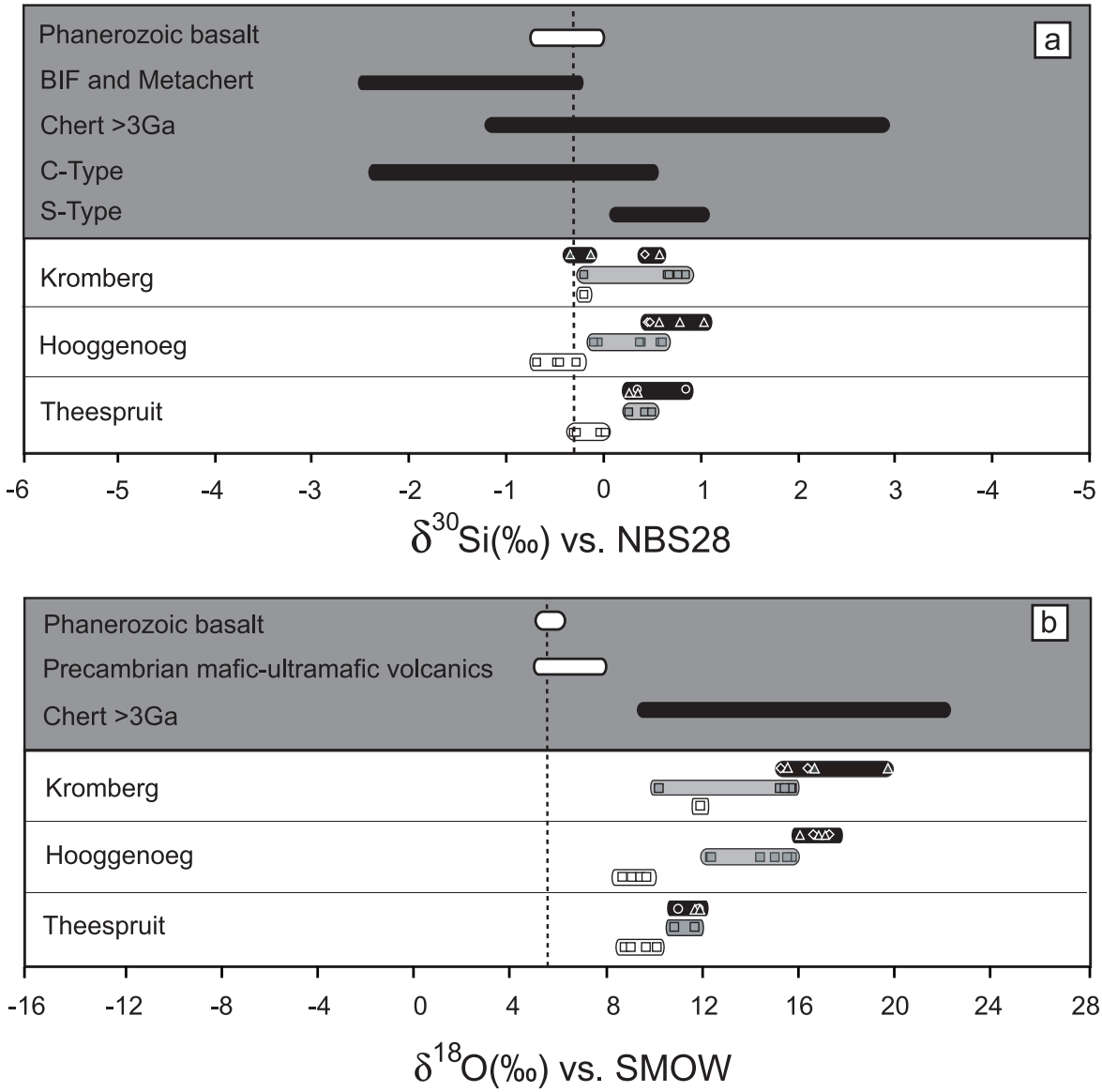

Fig. 2: $\delta^{30}Si$ and $\delta^{18}O$ values of terrestrial reservoirs relevant to this study. Top part (dark grey) of each diagram summarises the ranges for unaltered basalts, BIFs and cherts. The lower parts (white) are data from this study using the same symbols for rock types as in Figure 1. a) $\delta^{30}Si$ reservoirs: the vertical dotted line refers to the BSE ($\delta^{30}Si$=-0.28±0.06‰, Fitoussi et al., 2009; $\delta^{30}Si$=-0.29±0.08‰, Savage et al., 2010). Phanerozoic basalts (Douthitt, 1982; Ding et al., 1996; Ziegler et al., 2005b; Georg et al., 2007a, 2007b; Abraham et al., 2008), BIFs and metacherts (Ding et al., 1996; André et al., 2006; Steinhoefel et al., 2009) and cherts (Robert and Chaussidon 2006; van den Boorn et al., 2007, 2010). b) $\delta^{18}O$ reservoirs: the vertical dotted line refers to the mantle composition ($\delta^{18}O$=+5.5‰, Mattey et al., 1994). Phanerozoic basalts (Beaty and Taylor, 1982; Smith et al., 1984), Precambrian mafic ultramafic rocks (Hoffmann et al., 1986) and cherts (Knauth and Lowe, 1978; Robert, 1988; Robert and Chaussidon, 2006).

The similarity indicates that the mantle source for Archaean komatiites had the same isotope composition to the modern ocean ridge basalt source. At the high degrees of partial melting necessary for the generation of Archaean tholeiites and komatiites (Arndt et al., 2009), the mantle can be regarded as an isotopically uniform reservoir of O.

Therefore the $\delta^{18}O$ values of the unsilicifed basalts from this study are unlikely to be those of the original unaltered rock. $\delta^{18}O$ values of basalts increase, as do $\delta^{30}Si$ values, with increasing degree of silicification ($\delta^{18}O$ up to +15.6‰). The $\delta^{18}O$ values of chert veins (+16.4‰ to +17.1‰) and bedded cherts (+15.8‰ to +17.0‰) are similar to cherts from the Onverwacht Group previously analyzed (+15.1‰ to +22.7‰, Robert, 1988; +9.4‰ to 22.7‰, Knauth and Lowe, 1978; +13.9‰ to +16.5‰, Robert and Chaussidon, 2006). It is notable that there is a strong positive correlation between $\delta^{30}Si$ and $\delta^{18}O$ (Fig. 3a-d). Data arrays from the Kromberg and Hooggenoeg sections are similar. In contrast, the Theespruit data array has a different gradient in the $\delta^{30}Si$ vs. $\delta^{18}O$ plot . $\delta^{30}Si$ and $\delta^{18}O$ values generally correlate positively with SiO_2 in the Hooggenoeg and Theespruit Formations (Fig. 3e,f). Kromberg Formation data show more scatter due to the presence of two chert samples with negative $\delta^{30}Si$ values, but high $\delta^{18}O$.

6.5. Discussion

$\delta^{30}Si$ and $\delta^{18}O$ values correlate positively with SiO_2 contents (Fig. 3). Silicification of volcanic and overlying sedimentary rocks and correlation of $\delta^{18}O$ values and SiO_2 contents have been interpreted by Hofmann and Harris (2008) to be a result of seafloor alteration by diffuse, low-temperature hydrothermal fluids. Si isotope values may provide additional constraints. $\delta^{30}Si$ values of unsilicified basalts of this study resemble $\delta^{30}Si$ values of Phanerozoic basalts and are close to the Bulk Silicate Earth (BSE) value (Fig. 2). This suggests that the silicon budget remained mostly unaffected by the silicification process. In contrast, the average $\delta^{18}O$ values of the unsilicified rocks (+9.6±1.1‰) are significantly higher than fresh modern basalts and Archaean komatiites from Barberton, which have mantle-like $\delta^{18}O$ values (Smith et al., 1984). This apparent decoupling between Si and O isotopic data needs explanation.

6.5.1. Unsilicified basaltic rock suite: is there a process before silicification?

The $\delta^{30}Si$ values of unsilicified basalts range from -0.64‰ to -0.24‰ in the Hooggenoeg section and from -0.33‰ to -0.01‰ in the Theespruit section. A difference of $\Delta^{30}Si$=0.32‰ (Theespruit) or $\Delta^{30}Si$=0.40‰ (Hooggenoeg) within the unsilicified basaltic rock suite is significant with regard to the average standard deviation between the replicates (0.07‰, Table 1). It encompasses the $\delta^{30}Si$ values of the chondritic and mantle reservoirs and average fresh basalts (Douthitt, 1982; Ding et al., 1996; Ziegler et al., 2005b; Georg et al., 2007a, 2007b; Abraham et al., 2008; Fitoussi et al., 2009; Savage et al., 2010), Fig. 2). The isotopic heterogeneity among these unsilicified rocks may therefore reflect (1) differences in $\delta^{30}Si$ among the original magmas, or (2) fractionation linked to Si redistribution between

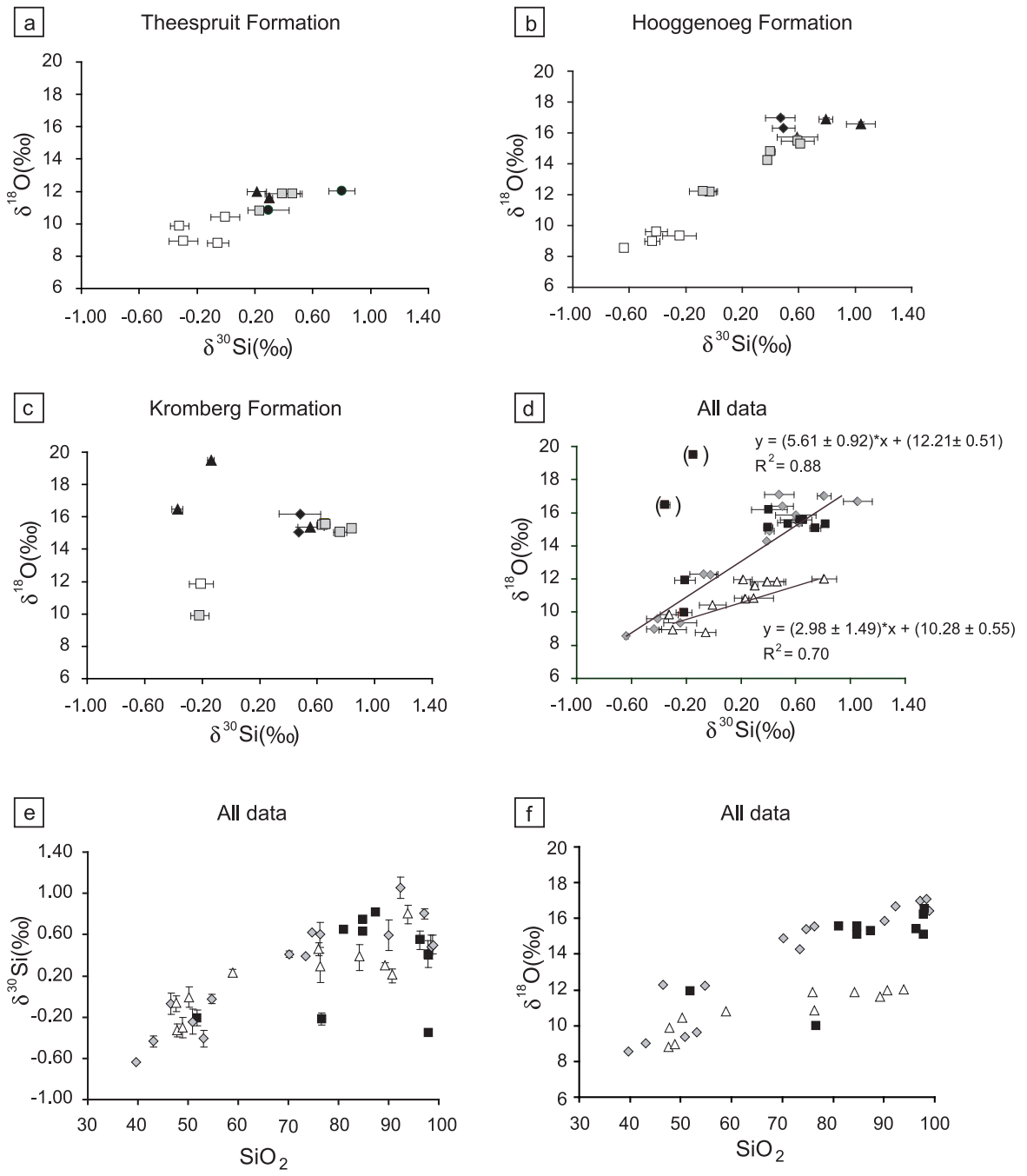

Fig. 3: (a,b,c) Plots of $\delta^{30}Si$ vs. $\delta^{18}O$ for the Theespruit, Hooggenoeg and Kromberg Formations, showing coupled behaviour of silicon and oxygen isotopes during the silicification process. For symbols see Fig.1. Panels d, e and f show the complete data set of all three sections: d) with lines of best-fit of $\delta^{30}Si$ vs. $\delta^{18}O$, (e) plots of SiO_2 vs. $\delta^{30}Si$ and (f) SiO_2 vs. $\delta^{18}O$. Theespruit Formation is illustrated by white triangles, the Hooggenoeg Formation by grey diamonds and the Kromberg Formation by black squares.

phases during post-magmatic mineral reactions. Recent studies have demonstrated a lack of isotopic heterogeneities between basalts from different tectonic settings, showing that the mantle melting processes had little impact on their isotopic compositions (Georg et al., 2007a, 2007b; Fitoussi et al., 2009; Savage et al., 2010). Besides, the high-temperature

Si isotopic fractionation between major phases of basalt crystallization (olivine and clinopyroxene) should, in theory, be very limited (Douthitt, 1982; Ding et al., 1996). A maximum range of about 0.1‰ is likely when comparing the very similar theoretical Si isotopic fractionation factors between silicate showing large structural differences such as quartz-olivine or quartz-clinopyroxene (($\Delta_{quartz\text{-}forsterite}$ = 0.196‰ and $\Delta_{quartz\text{-}enstatite}$ = 0.224‰ at 1 200°C; Méheut et al., 2009). Moreover, the lack of variations for immobile element ratios, such as Al_2O_3/TiO_2 or La/Yb, suggests that all studied pillow lavas have been fractionated to similar degrees from a similar magma source. We conclude that the observed heterogeneities in Si isotopic signatures among the unsilicified basalts cannot be a primary magmatic feature. They are attributed to post-magmatic processes, either a late magmatic alteration or a metamorphic overprint.

In order to explain the high O isotope values of unsilicified basalts, a post-magmatic process seems most likely. Unsilicified basalts show mineral assemblages of greenschist- (Hooggenoeg and Kromberg Formations) and amphibolite-facies (Theespruit Formation) metamorphic grade. It is thus possible that metamorphism influenced the isotope composition, especially for the Theespruit Formation. However, Lecuyer et al. (1994) reported the lowering of $\delta^{18}O$ values of Barberton komatiites by metamorphic fluids (with initial isotopic values of $\delta^{18}O$ = +5 to +7‰) to between +3.2‰ and +5.0‰ at high temperature (-450°C) under high water/rock ratios. The komatiites investigated by Lecuyer et al. (1994) derive from the Schapenburg greenstone belt, which correlate with komatiites of Barberton, but show a higher metamorphic grade. This may indicate a role for metamorphism in the formation of higher $\delta^{18}O$ in basalts, as lower grade metamorphism induces an increase in $\delta^{18}O$.

It is well known from Phanerozoic submarine basalts that low-temperature seafloor alteration increases their $\delta^{18}O$ values (e.g. Muehlenbachs and Clayton, 1972; Gregory and Taylor, 1981). High-temperature alteration can also increase $\delta^{18}O$ values but, due to the inverse relationship of the temperature and fractionation factors, the shift becomes smaller as temperature increases until at ~400°C the rock $\delta^{18}O$ value starts to decrease. Smith et al. (1984) argued that an increase in oxygen isotopic composition of Barberton pillow lavas may have taken place shortly after emplacement of these lavas on the seafloor, prior to the onset of silicification, when rapid effusion of pillow lavas resulted in relatively high-T (240-450°C) exchange processes with deep-seated water. Therefore the slightly higher $\delta^{18}O$ values of the unsilicified basalts are likely to be the result of low-temperature alteration processes.

6.5.2. The source of silicon

The origin of silicon during silicification has been the subject of debate (e.g. Knauth and Lowe, 2003; Van Kranendonk, 2006; Hofmann and Harris, 2008). In general, the positive $\delta^{30}Si$ value in cherts can be attributed to one or more of the following (Steinhoefel et al., 2009): the influence of a continental source, increased seawater temperature, precipitation from isotopically positive seawater or open system type fractionation of hydrothermal fluids (André et al., 2006; Robert and Chaussidon, 2006; van den Boorn et al., 2007, 2010). Coupling Si to O isotopes helps to decipher which factor determined the isotope composition and hence the silicon source.

Potential sources of silicon include the breakdown of primary minerals (olivine, pyroxenes and plagioclase), glass and its devitrified products, magmatic-derived hydrothermal fluids and seawater (Hofmann and Harris, 2008). Hanor and Duchac (1990) stated that pervasive silicification as recorded in strata from Barberton required the introduction of large volumes of mildly-acidic pore fluids that led to the breakdown of silicates in the basalts. The dissolution of primary minerals or glasses preferentially releases the lighter Si isotopes into the fluid (Ziegler et al., 2005b). In detail, in the initial stages of dissolution of crystalline material induce a negative ^{30}Si shift away from the $\delta^{30}Si$ in the rock ($\Delta max \sim -3‰$) that decreases with greater degrees of dissolution. In contrast, the dissolution of glassy material produces a less distinct ^{30}Si shift ($\Delta max \sim -1‰$), given that glassy material lacks crystallographic order. Subsequent silica precipitation from such fluids again preferentially removes these lighter isotopes from the fluid in the precipitating phases (e.g. Ding et al., 1996; Basile-Doelsch et al., 2005). The repetition of such a process would lead to gradual depletion of the precipitated phase in ^{30}Si, lowering the $\delta^{30}Si$ values below those found for the chondritic and BSE reservoirs (Basile-Doelsch et al., 2005). This is the opposite of what is observed for the silicified basalts. This indicates that the main source of the mobilised silicon is unlikely to have been just originated from *in-situ* mineral breakdown reactions. From the oxygen isotope perspective, the interaction of basalt with fluid is described as equilibrium isotope fractionation between the two phases, which is in turn determined by temperature. Thus depending on the isotope composition of the fluid, interaction with magmatic water ($\delta^{18}O = 5$ to $7‰$) would show different isotope variation than with seawater ($\delta^{18}O = 0‰$).

An alternative explanation for the observed $\delta^{30}Si$ range may be the successive precipitation from hydrothermal fluids by conductive cooling. Closed-system fractionation cannot produce silica deposits with more positive $\delta^{30}Si$ values than that of the initial solution (see van den Boorn et al., 2010 for illustration). An increase in the $\delta^{30}Si$ value of the precipitating silica can be achieved only by Rayleigh-type fractionation after the solution has precipitated

a relatively high proportion of silica (André et al., 2006; van den Boorn et al., 2010). To reach a value of $\delta^{30}Si>0$ for the precipitates from a hydrothermal fluid with an original value of $\delta^{30}Si=-0.2‰$ about 65% to 67% must have been precipitated, corresponding to f=0.33 to 0.35, where "f" represents the fraction of silica remaining. So the paucity of observed negative $\delta^{30}Si$ values within the silicified rocks does not fit well with a pure hydrothermal derivation for silica (van den Boorn et al., 2010).

Seawater has been regarded as the most likely source of silica for silicification (Hofmann and Harris, 2008). The positive $\delta^{30}Si$ values for most of our samples also point to seawater as the dominant silicifying medium. The extrapolation of the array of the silicified samples to a fully silicified composition of 100% SiO_2 give end-member $\delta^{18}O$ and $\delta^{30}Si$ of circa +18‰ and +1.0, (Hooggenoeg/Kromberg) and to 14‰ and 0.8‰ (the Theespruit Formation), respectively. This shows that in both cases the extrapolated values are close to the isotope composition observed in the overlying cherts, arguing for Archaean seawater as an end-member of the silicification process.

Another possible explanation of the isotope values is the mixing of two sources e.g. hydrothermal fluid with seawater. Based on their mixing model, van den Boorn et al. (2010) were able to show that at temperatures below ~150 to 175°C the hydrothermal fluid remains largely non-precipitated to the point of their appearance at the seafloor ($\delta^{30}Si \sim -0.2‰$). Therefore, this negative isotope composition of $\delta^{30}Si \sim -0.2‰$ is not in line with hydrothermal silica deposition during silicification. Furthermore, assuming a tidal-flat depositional environment for the silicification process (De Vries, 2004), they concluded that intensive mixing with seawater due to high initial porosities of the sediments and very high water/rock ratios (Rouchon and Orberger, 2008) can lead to obliteration of the hydrothermal isotope values and therefore to a subordinate importance of hydrothermally derived silica.

6.5.3. The controlling factor of the variation in isotope composition

The pronounced positive correlations between $\delta^{30}Si$, $\delta^{18}O$ and SiO_2 (Fig. 3) implies that the variation in isotope composition for both O and Si is driven by the silicification process. The nature of the covariation gives us further constraints on the controlling factors of the isotope fractionation and thus about the process of silicification.

6.5.3.1. Water-rock interaction

The isotopic change during water-rock interaction depends on the O-Si isotopic ratio and on O-Si concentrations of the fluid from which silica is precipitated and on the silicon and oxygen isotope fractionation factor between quartz and the fluid. Despite the fact that

Archaean seawater was saturated with respect to silica (Siever, 1992; Treguer et al., 1995), the amount of silicon (SiO_2 = 49 ppm. at 20°C, Gunnarson and Arnorsson, 2000) is extremely low in comparison to oxygen. Due to this high $(O/Si)_{water}/(O/Si)_{basalt}$ concentration ratio, the interaction with seawater should in general affect the isotopic composition of oxygen in the rock much more strongly than that of silicon. Consequently the theoretical curve of water-rock O-Si isotopic alteration is expected to be a hyperbola rather than a linear trend in a binary $\delta^{18}O-\delta^{30}Si$ diagram.

In order to investigate the role of water-rock interaction we calculated a hypothetical alteration curve with different water-rock ratios (see supplementary information, Calculation 1S). We observe that the silicon isotope composition of the rocks does not show any indication of the $\delta^{30}Si$ impact of the seawater (Fig. 4b), even for very high water/rock interactions. The computed values of the water-rock interaction show only a change to higher $\delta^{18}O$. We therefore conclude that such a process cannot explain the observed positive correlation trend, except by postulating implausibly high Si concentrations for the Archaean seawater.

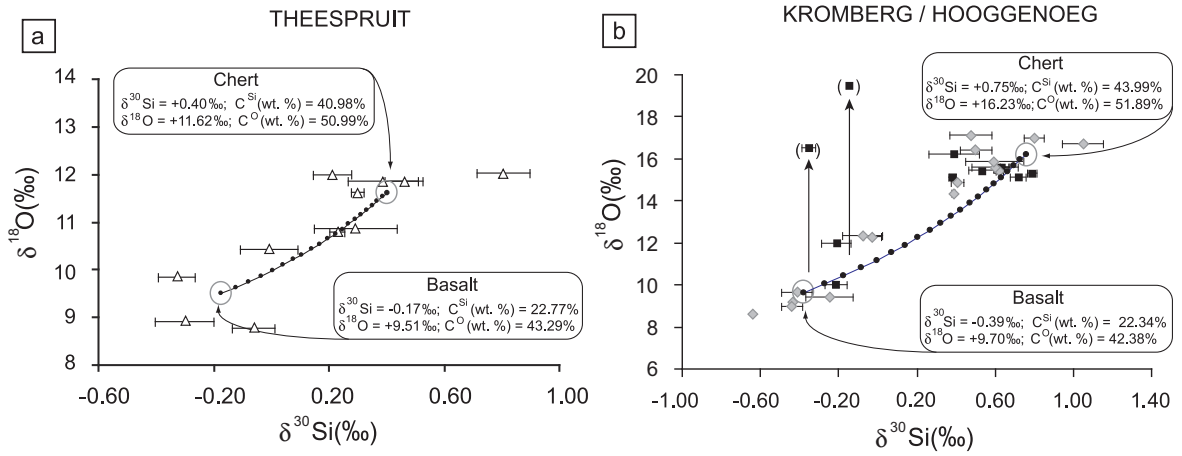

Fig.4: Comparison of calculations (modelled water-rock interaction and mixing trends) and analysed values for the Theespruit (a) and Hooggenoeg/Kromberg Formations (b). Owing to the similarity of Hooggenoeg and Kromberg Formations, only one trend is modelled. The water-rock interaction (Calculation 1S) is illustrated schematically by arrows facing upwards, since the computed results show only a change to higher $\delta^{18}O$. The modelled mixing trends (Calculation 2S) between basalt and chert end-member are illustrated by a black curve with black circles showing the single computed values for different fractions of isotope and concentration composition. The end-member compositions used for the calculation are illustrated by grey open circles and are described in the boxes.

6.5.3.2. The role of diffusion

The relative magnitude of solid state diffusion coefficients for silicon isotopes has not been established so far. It is known that oxygen isotopes have a much higher diffusivity (D; e.g. Giletti, 1986) than silicon isotopes; the difference in diffusivity must increase with lower temperature ($D_O >> D_{Si}$). Consequently it is expected that both isotope systems would behave

differently during diffusion, causing a pronounced hyperbolic line in a binary $\delta^{30}Si$-$\delta^{18}O$ diagram. As the $\delta^{30}Si$-$\delta^{18}O$ correlation is best-fit by a linear correlation trend, we conclude that diffusivity does not play a major role, which is supported by the fact that solid-state diffusion is very limited at low temperatures.

6.5.3.3. Two end-member component mixture

Precipitated silica will have a $\delta^{18}O$ value that is higher than the fluid from which it formed, because $\Delta^{18}O_{qtz\text{-}water}$ is always positive (e.g. Matsuhisa et al., 1979). In contrast, precipitates have lower $^{30}Si/^{28}Si$ ratios than the dissolved Si in the fluid (e.g. Ding, 1996, Basile-Doelsch et al., 2005, Georg et al., 2009a). Thus variable degrees of precipitation from a constantly renewed juvenile fluid would lead to a negative O-Si isotopic correlation; with Si isotopes and O isotopes evolving to higher and lower values, respectively during both closed and open system precipitation processes. However, the precipitation process also depends on the remaining fraction of both elements. The amount of oxygen in the fluid is so abundant that it remains constant during precipitation, so that the $\delta^{18}O$ of the oxygen in the water will not change through time. In contrast, considering the limited abundance of Si present as a dissolved species, the Si will gradually be exhausted from the solution, leaving a residual fluid enriched in ^{30}Si. Thus both isotope systems can evolve to heavier isotopic compositions with the ageing of the precipitating fluid, despite their opposite fractionation behaviour. From this we postulate that (1) the silicification was controlled by downward percolating seawater with a Si isotopic composition that was much more enriched in ^{30}Si than the most enriched rock sample ($\delta^{30}Si$>+1.05‰); (2) the observed trends between $\delta^{30}Si$, $\delta^{18}O$ and SiO_2 (Fig. 3) result from the mixing of the basalt with a seawater-derived silica component precipitated in both the lava flows and their sedimentary covers and can be treated as a mixing line, between basalt and cherts.

We applied the ratio-concentration relationships in binary mixing (Albarède, 1995; Fig. 4a,b and Calculation 2S and Table 2S in the supplementary material) to model two-component mixing between basalt and chert. Average analysed values from this study are used for the calculation of both end-members (basalt and chert), in order to avoid extreme values, which might give an erroneous mixing trend. In general, much higher values for $\delta^{30}Si$ are not expected, because the Si isotope values of the cherts of silicified precursor rocks in Pilbara do not exceed 1.1‰, similar to Barberton (Fig. 2). Oxygen isotope values of Onverwacht cherts show a range, but it is assumed that only the highest values are geologically relevant, since post-depositional isotopic exchange with meteoric or hydrothermal fluids alter the cherts towards lower $\delta^{18}O$ by up to 10% (Knauth and Lowe, 1978).The calculations are shown in Figures

4a (Theespruit Formation) and 4b (Hooggenoeg and Kromberg Formations), respectively. It can be observed that the modelled trends fit the measured isotopic compositions. Thus, a two end-member component mixing between basalt and a chert-like SiO_2-rich precipitate is theoretically supported.

6.5.4. The potential of Si isotopes as a geothermometer

The trend of $\delta^{30}Si$ and $\delta^{18}O$ values for the Theespruit Formation is less steep (Fig 3d), and may be a result of different factors: 1) secondary effects (metamorphism or alteration), 2) the prevalent temperature during isotope fractionation and 3) the isotope composition of the fluid from which the silica precipitated.

In comparison to the other formations, the Theespruit Formation differs in its higher metamorphic facies (amphibolite). During metamorphism, the O-isotope values of cherts are generally lowered (Garlick and Epstein, 1967, Knauth and Lowe, 1978), due to their exchange with metamorphic fluids that have relatively low isotope ratios owing to former interactions with crustal oxygen reservoirs ($\delta^{18}O$ = +5 to +12‰). A decrease in the $\delta^{18}O$ value owing to strong metamorphic overprint is not likely during closed system metamorphism. Instead, very large open exchanges with a significant amount of metamorphic percolating fluid or a loss of fluid by dehydration are required to significantly modify the $\delta^{18}O$. Hooggenoeg and Kromberg Formations also experienced a metamorphic overprint, albeit at greenschist facies. A further difference is that rocks of the latter formations are undeformed, whereas the Theespruit rocks are strongly foliated, potentially providing enhanced access of circulating metamorphic fluids. Considering potential Si-O mass balances, Si isotopes would presumably be less affected by metamorphism (André et al., 2006) and would change more slowly than O-isotopes due to the high O/Si ratio in water.

The formation of the Theespruit cherts could have happened at different temperature conditions than the Hoogenoeg/Kromberg formation. Hofmann and Harris (2008) concluded by means of element depletion-enrichment patterns in conjunction with oxygen isotope data that the silica alteration zones originated by low-temperature (c. 100–150 °C) hydrothermal processes. Assuming that $\delta^{18}O$ values of seawater were constant through time at 0‰, Muehlenbachs et al. (2009) deduced from multiple SiO_2-$\delta^{18}O$ trends of the Onverwacht Group that silicification operated under two different mechanisms: one is passively related to the formation of bedded cherts at the seawater/rock interface (80°C), whereas the other is assigned to diffuse impregnation of hydrothermal fluids (180 to 250°C). However, these different temperature conditions must be related to different sites, since the $\delta^{18}O$ in basalts vary depending on whether they lie beneath high $\delta^{18}O$ or cherts with hydrothermal field

association and lower $\delta^{18}O$. We argue that the silicification process did not take place at a high temperature, since chert-water fractionation would require that the $\delta^{18}O$ of seawater in equilibrium with the most silicified basalt was high. For example at 350°C, the $\Delta^{18}O_{chert\text{-}water}$ ($\Delta^{18}O_{chert\text{-}water}=\delta^{18}O_{chert}-\delta^{18}O_{water}$) has a value of +4.6. Consequently, seawater in equilibrium with a chert ($\delta^{18}O$=+16‰) would have an isotope composition of +11.4‰, far removed from the expected uniform oceanic reservoir.

The composition of Archaean seawater is poorly constrained, but was likely close to silica saturation with regard to amorphous silica (Siever, 1992), so that silica precipitation occurred relatively easily due to any perturbation such as a drop in temperature (Posth et al., 2009). Any precipitation of amorphous silica precipitation from such a reservoir would tend to move the $\delta^{30}Si$ of the residual dissolved silicon to higher values with time. We thus infer that silica precipitation gradually increased ^{30}Si in seawater with time. We interpret this as the cause of the gradual increase in the chert $\delta^{30}Si$ values with time (Robert and Chaussidon, 2006). $\delta^{30}Si$ values are negative at 3.9 Ga (-1.99‰<$\delta^{30}Si$<-0.25‰, André et al., 2006) and reach very positive values (~+4‰) at the end of the middle Proterozoic (Robert and Chaussidon, 2006). The increase in isotope value from the Theespruit (+0.21‰<$\delta^{30}Si$<+0.81‰) to the Hooggenoeg/Kromberg cherts (+0.40‰<$\delta^{30}Si$<+1.05‰) fit this trend of increasing $\delta^{30}Si$ of seawater from 3.54Ga to 3.45-3.33Ga.

6.5.5. Vein chert signatures

Carbonaceous chert veins cross-cut silicified basalts and have been interpreted to represent hydraulic fractures partially infilled by silicified sediment derived from overlying chert horizons (Hofmann and Bolhar, 2007; Hofmann and Harris, 2008). This hypothesis can be evaluated in the light of the new Si isotopic data (Fig. 1). In the Hooggenoeg section, the veins have Si isotope values of +0.48‰ to +0.50‰, which are similar to the surrounding silicified basalt (+0.41‰), but contrast with those of the overlying black carbonaceous cherts (+0.80‰). This suggests that a significant part of the Si was precipitated in isotopic equilibrium with the surrounding silicified basalts but was not in isotopic equilibrium with the overlying chert beds. It further implies that filling of the vein by carbonaceous matter occurred prior to completion of the silicification process. Field observations support this, as reaction zones of non-carbonaceous chert ≤ 5 mm thick are frequently developed between the carbonaceous vein chert fill and the basaltic host rock.

In contrast, vein chert from the Kromberg section ($\delta^{30}Si$=+0.40‰) resembles the overlying chert horizon ($\delta^{30}Si$=+0.55‰) but not the surrounding silicified rocks ($\delta^{30}Si$=+0.81‰ and +0.63‰). The presence of cherts with negative $\delta^{30}Si$ (Fig. 1) indicate that the development

of Si isotopes in the vein-chert might be more complex in this unit, but the currently limited amount of data do not allow reconstruction of a multi-stage vein-chert formation history. Hofmann and Bolhar (2007) noted that many chert veins are complex, consisting of several generations of sedimentary infills, hydrothermal chert precipitates and variably silicified host rock material.

6.6. Conclusions

The isotope data reported here provide a new perspective on early Archaean chert formation and related silicification processes as well as providing some new key parameters to monitor the chemical evolution of the Precambrian oceans and to better constrain the silica-rich environments in which some controversial claims of early fossils have been discovered.

The positive isotope composition of $\delta^{30}Si$ and positive correlation between $\delta^{30}Si$ and $\delta^{18}O$ indicate that the source of silica for silicification was seawater. Due to the low concentration of Si in seawater, water-rock interaction is unlikely to have influenced the Si isotope composition. Using simple mixing calculations, we demonstrated that the observed SiO_2, $\delta^{18}O$ vs. $\delta^{30}Si$ correlations may be regarded as mixing trends between two end members; basalts and a seawater-derived SiO_2-rich precipitate.

Possible factors that could account for different gradients of $\delta^{30}Si$ vs. $\delta^{18}O$ are changes of seawater isotope signature, temperature condition or secondary alteration.

The apparent increase in the Si isotopic composition of chert from the very early Archaean (André et al., 2006) to the late Proterozoic (Robert and Chaussidon, 2006), is confirmed by the present data, showing that the chemical evolution of Precambrian oceans might have been partly controlled by these Archaean silicifications.

Si isotopes could serve as a tool to better constrain the silica precipitation in Archaean quartz veins; this may help to elucidate the origin of the carbonaceous matter found within these veins.

Supplementary material:

6.1.S Analytical methods and chemical preparation techniques

Major and trace element composition as well as oxygen isotope data of most of our rock samples have been described by Hofmann and Harris (2008). However, as additional samples were investigated during this study, all samples were again analyzed for major and trace elements on different aliquots, which were prepared avoiding silicon contamination at the University of Mainz, Germany (Table 1S). Only the black parts of the black- and white-banded cherts were taken for analysis.

Table 1S: Stable isotope data ($\delta^{30}Si$ and $\delta^{18}O$) in comparison to major and trace elements. Major and trace elements are re-measured or completed to the data set of Hofmann and Harris (2008).

	THEESPRUIT						
	Unsilicified basalt	Feslic schist	Chert		Feslic schist	Silicified basalts	
Sample code	**AT1***	**AT2***	**AT3**	**TS2**	**AT4***	**AT5R**	**AT5M**
Description	unsil. mb.	felsic schist	carb chert/shale	carb shale	felsic schist	sil. pb.	sil. pb.
Depth (m)	16	12.5	13	3	2	-1	-1
$\delta^{30}Si$ (‰)	**-0.06**	**0.29**	**0.30**	**0.21**	**0.81**	**0.39**	**0.46**
$\delta^{18}O$ (‰)	**8.79**	**10.86**	**11.61**	**11.98**	**12.03**	**11.86**	**11.86**
Major elements (%)							
SiO_2	47.60	76.28	89.28	90.73	93.86	84.13	76.01
TiO_2	0.96	0.17	0.08	0.12	0.06	1.30	0.51
Al_2O_3	4.93	12.75	6.49	4.15	3.68	7.80	11.11
Fe_2O_3	16.53	1.95	0.39	0.89	0.63	2.68	4.57
MnO	0.27	0.02	0.00	0.01	0.01	0.05	0.21
MgO	11.00	1.95	0.50	0.88	0.43	0.63	1.71
CaO	16.54	1.47	0.39	0.12	0.34	0.46	1.04
Na_2O	1.27	1.72	0.48	0.20	0.54	1.09	2.45
K_2O	0.03	1.13	1.34	0.02	0.24	1.16	0.59
$P2O_5$	0.08	0.02	0.02	0.01	0.01	0.01	0.05
LOI	6.16	2.09	0.98	1.74	0.89	1.12	1.71
Sum	**99.56**	**99.55**	**99.95**	**98.91**	**100.69**	**100.49**	**100.00**
Trace elements (ppm)							
Sc	24.9	5.06	4.35	4.93	5.29	23.3	20.8
V	179	4.38	4.08	14.8	7.51	172	200
Cr	1606	51.0	21.1	255	67.2	348	222
Co	103	171	204	267	261	263	293
Ni	983	68.4	27.6	132	34.9	43.9	103
Cu	98.9	9.17	4.97	21.9	9.50	14.3	30.7
Zn	117	16.6	1.09	18.1	3.29	1.88	4.15
Ga	8.53	14.0	7.65	5.66	4.42	8.44	11.4
Rb	1.17	33.5	23.5	0.050	4.66	26.6	14.4
Sr	100	85.9	47.1	7.33	22.8	69.7	146
Y	13.1	13.6	8.90	2.90	3.05	8.31	7.70
Zr	56.2	143	56.0	26.2	48.6	47.2	16.1
Nb	5.38	15.2	5.25	4.50	2.78	5.84	2.97
Cs	0.732	0.320	0.122	<d.l.	0.020	0.162	0.137
Ba	14.1	258	251	4.84	20.2	61.5	30.9
La	7.52	37.5	15.5	2.13	4.72	6.61	6.06
Ce	19.9	65.3	30.4	6.03	11.2	19.7	15.8
Pr	2.88	5.95	3.73	0.520	1.07	2.50	2.15
Nd	14.1	17.5	14.2	1.94	3.75	11.5	9.63
Sm	3.11	2.12	2.52	0.487	0.656	2.58	2.18
Eu	1.11	0.330	0.362	0.091	0.143	0.856	0.906
Gd	3.08	1.92	1.89	0.384	0.644	2.00	2.02
Dy	2.72	2.34	1.67	0.557	0.581	1.78	1.64
Ho	0.561	0.504	0.307	0.112	0.114	0.307	0.289
Er	1.33	1.61	0.797	0.395	0.392	0.872	0.795
Yb	1.27	2.05	0.762	0.401	0.494	0.942	0.616
Lu	0.177	0.318	0.099	0.053	0.064	0.122	0.096
Hf	1.41	4.06	2.04	0.652	1.47	1.34	0.466
Ta	0.376	3.05	3.39	2.41	3.57	3.20	3.01
Pb	0.907	1.84	0.046	<d.l.	<d.l.	0.043	0.149
Th	0.450	14.2	9.82	1.36	4.32	0.369	0.072
U	0.108	2.75	0.797	0.559	0.762	0.154	0.101
Sum REE	57.7	137.5	72.3	13.1	23.8	49.8	42.2
Eu/Eu*	1.66	0.76	0.77	0.98	1.02	1.76	2.01
Y/Ho	23.3	27.0	29.0	26.0	26.8	27.1	26.7
Al_2O_3/TiO_2	5.15	75.00	81.13	34.58	61.33	6.00	21.78

Table 1S (Continued)

	THEESPRUIT (continued)				HOOGGENOEG		
	Silicified basalt	Unsilicified basalts			Chert		
Sample code	**AT6***	**AT7***	**AT8***	**AT9***	**H3B**	**H2B**	**AH14**
Description	sil. pb.	unsil. mb.	unsil. pb.	unsil. mb.	gr. chert	bl. chert	gr. chert
Depth (m)	-5	-18	-30	-55	0.7	0.5	0.2
δ^{30}Si (‰)	**0.23**	**-0.33**	**-0.01**	**-0.30**	**1.05**	**0.80**	**0.60**
δ^{18}O (‰)	**10.79**	**9.86**	**10.44**	**8.94**	**16.70**	**17.00**	**15.84**
Major elements (%)							
SiO_2	58.90	47.84	50.23	48.89	92.34	97.05	90.09
TiO_2	1.66	1.69	1.52	1.96	0.38	0.06	0.36
Al_2O_3	12.65	12.04	10.73	13.23	3.94	0.88	4.84
Fe_2O_3	16.84	17.90	18.13	19.47	0.31	0.31	0.84
MnO	0.91	0.24	0.43	0.28	0.00	0.02	0.05
MgO	4.74	6.44	4.62	4.82	0.36	0.01	0.27
CaO	1.02	10.24	9.87	7.39	0.05	0.06	0.06
Na_2O	0.72	2.41	2.51	3.66	<d.l.	<d.l.	0.08
K_2O	0.06	0.16	0.14	0.21	1.39	0.24	1.65
$P2O_5$	0.20	0.12	0.12	0.00	<d.l.	<d.l.	0.01
LOI	2.94	0.81	2.28	0.73	1.35	0.75	1.54
Sum	**100.74**	**99.91**	**100.69**	**100.81**	**100.14**	**99.20**	**99.81**
Trace elements (ppm)							
Sc	57.8	29.1	34.8	17.0	14.9	6.91	12.9
V	356	289	286	231	107	8.39	164
Cr	571	23.7	526	1.27	77.6	36.2	66.8
Co	174	95.0	116	68.4	292	371	135
Ni	245	107	198	41.4	18.1	77.9	34.5
Cu	248	368	137	258	4.54	11.8	0.255
Zn	116.6	21.3	121	62.8	1.27	5.26	1.54
Ga	16.1	14.3	13.1	13.8	5.85	1.11	6.40
Rb	3.08	0.973	1.87	1.38	2.22	3.56	2.30
Sr	48.4	165	161	117	1.57	3.06	1.10
Y	20.4	15.3	13.0	16.6	0.547	0.698	1.02
Zr	80.7	65.6	58.0	80.6	22.4	9.8	20.3
Nb	9.98	8.33	7.18	9.90	1.53	1.16	2.70
Cs	0.119	0.033	0.142	0.126	0.108	0.112	0.039
Ba	8.72	32.7	61.0	27.4	50.2	14.3	71.6
La	9.01	8.30	5.88	6.98	0.332	0.674	0.258
Ce	30.0	18.9	14.3	21.5	0.863	1.66	0.817
Pr	4.08	2.97	2.18	3.30	0.098	0.163	0.103
Nd	20.1	14.6	10.7	16.5	0.404	0.731	0.396
Sm	5.19	3.14	2.56	3.88	0.108	0.139	0.156
Eu	1.95	1.15	0.880	1.39	0.041	0.074	0.087
Gd	5.57	3.44	2.43	3.69	0.104	0.146	0.146
Dy	4.68	3.11	2.58	3.46	0.095	0.105	0.179
Ho	0.842	0.596	0.493	0.656	0.023	0.027	0.039
Er	2.16	1.67	1.39	1.79	0.069	0.067	0.113
Yb	1.84	1.51	1.27	1.65	0.061	0.080	0.104
Lu	0.261	0.226	0.171	0.240	0.014	0.008	0.018
Hf	2.07	1.85	1.60	2.03	0.662	0.254	0.771
Ta	1.52	0.828	1.05	0.841	4.53	4.62	2.02
Pb	0.963	0.135	0.540	0.557	< d.l.	0.072	0.053
Th	0.749	0.488	0.416	0.556	0.167	0.257	0.140
U	0.159	0.105	0.113	0.170	0.136	0.166	0.802
Sum REE	85.7	59.7	44.9	65.1	2.2	3.9	2.4
Eu/Eu*	1.68	1.62	1.64	1.71	1.78	2.39	2.70
Y/Ho	24.2	25.6	26.4	25.3	23.9	26.2	25.9
Al_2O_3/TiO_2	7.62	7.12	7.06	6.75	10.37	14.67	13.44

Table 1S (Continued)

	HOOGGENOEG (continued)							
	Chert-vein		Silicified basalts					
Sample code	**H1B**	**AH15**	**AH13***	**AH16**	**AH12***	**AH11***	**AH18***	**AH18R**
Description	bl. chert-vein	bl. chert-vein	sil. pb.	sil. b.	sil. mb.	sil. pb.	sil. pb. center	sil. pb. rim
Depth (m)	-1	-2	-1.5	-5	-7	-19	-30	-30
δ^{30}Si (‰)	**0.48**	**0.50**	**0.41**	**0.60**	**0.62**	**0.39**	**-0.02**	**-0.07**
δ^{18}O (‰)	**17.10**	**16.41**	**14.90**	**15.56**	**15.39**	**14.30**	**12.24**	**12.29**
Major elements (%)								
SiO_2	98.46	98.94	70.26	76.30	72.54	73.42	54.70	46.58
TiO_2	0.04	0.02	0.90	0.86	0.87	0.83	0.87	1.40
Al_2O_3	0.35	0.21	12.36	11.44	11.25	11.01	10.90	17.04
Fe_2O_3	0.12	0.12	1.21	0.62	1.02	2.73	11.33	10.07
MnO	0.01	0.01	0.03	0.02	0.04	0.05	0.16	0.14
MgO	0.10	0.12	1.99	1.13	1.73	1.71	3.21	3.15
CaO	0.29	0.27	2.22	1.19	2.40	1.50	7.20	6.86
Na_2O	<d.l.	<d.l.	<d.l.	<d.l.	<d.l.	<d.l.	<d.l.	<d.l.
K_2O	0.12	0.07	4.28	3.92	3.93	3.42	1.96	4.72
$P2O_5$	<d.l.	<d.l.	0.07	0.08	0.07	0.06	0.06	0.04
LOI	0.94	0.64	6.40	4.41	5.44	4.86	9.54	10.15
Sum	**100.43**	**100.40**	**99.60**	**99.99**	**99.16**	**99.48**	**99.79**	**100.07**
Trace elements (ppm)								
Sc	5.54	4.46	26.7	23.7	20.8	21.1	24.1	41.9
V	6.89	5.67	294	285	300	266	294	481
Cr	22.8	16.9	87.6	71.2	110	83.9	87.8	134
Co	461	515	68.8	98.6	41.6	103	65.1	68.9
Ni	42.9	33.8	23.4	27.2	27.7	63.4	74.6	135
Cu	12.4	6.93	5.16	13.8	136	3.78	194	203
Zn	12.8	2.38	0.689	0.740	10.2	0.773	147	130
Ga	0.722	0.760	11.3	12.1	13.7	10.1	11.3	19.0
Rb	1.65	0.396	64.6	73.2	73.5	67.6	48.5	124
Sr	1.54	1.29	6.44	4.30	7.54	3.11	19.0	16.1
Y	0.417	0.313	5.91	5.59	7.70	9.08	10.6	16.0
Zr	4.42	2.89	39.6	37.4	40.6	33.6	126	66.4
Nb	0.879	0.847	2.22	2.24	2.32	1.93	2.24	3.72
Cs	0.204	0.025	0.887	1.44	1.66	1.36	0.968	1.71
Ba	10.3	7.06	135	105	106	91.6	32.2	82.0
La	0.194	0.126	1.67	1.84	2.11	2.15	2.35	2.61
Ce	0.458	0.401	5.45	5.98	6.12	6.84	6.84	7.73
Pr	0.055	0.053	0.707	0.866	0.870	0.947	1.03	1.15
Nd	0.229	0.248	3.61	4.22	4.48	4.85	5.12	6.18
Sm	0.044	0.052	1.01	1.21	1.28	1.39	1.48	2.04
Eu	0.034	0.026	0.350	0.414	0.470	0.395	0.532	0.744
Gd	0.068	0.091	1.15	1.33	1.48	1.54	1.64	2.35
Dy	0.050	0.062	1.04	1.22	1.59	1.73	2.05	2.94
Ho	0.011	0.019	0.230	0.225	0.314	0.353	0.430	0.622
Er	0.032	0.038	0.601	0.594	0.874	1.00	1.20	1.81
Yb	0.046	0.043	0.493	0.569	0.775	1.07	1.50	2.01
Lu	0.008	0.006	0.070	0.074	0.124	0.159	0.223	0.316
Hf	0.121	0.076	1.14	1.03	1.20	0.945	1.07	1.80
Ta	5.96	7.06	1.00	1.27	0.630	1.04	0.338	0.301
Pb	0.126	1.52	0.011	0.014	0.728	0.031	0.661	0.742
Th	0.118	0.065	0.205	0.168	0.206	0.162	0.188	0.309
U	0.790	0.017	0.085	0.060	0.157	0.032	0.045	0.051
Sum REE	1.2	1.2	16.4	18.5	20.5	22.4	24.4	30.5
Eu/Eu*	2.76	1.66	1.49	1.51	1.57	1.24	1.57	1.56
Y/Ho	36.4	16.4	25.7	24.8	24.5	25.7	24.6	25.8
Al_2O_3/TiO_2	8.75	10.50	13.73	13.30	12.93	13.27	12.53	12.17

Table 1S (Continued)

	HOOGGENOEG (continued)				KROMBERG		
	Unsilicified basalts				Chert	Silicified basalt	Chert-vein
Sample code	**AH10***	**AH10R**	**AH17***	**AH17R**	**AK15**	**AK12***	**AK4**
Description	unsil. pb. center	unsil. pb. rim	unsil. pb. center	unsil. pb. rim	bl/w chert	sil. pb.	bl. chert-vein
Depth (m)	-60	-60	-150	-150	2	-0.7	-2
δ^{30}Si (‰)	**-0.44**	**-0.64**	**-0.24**	**-0.41**	**0.55**	**0.81**	**0.40**
δ^{18}O (‰)	**9.00**	**8.56**	**9.37**	**9.62**	**15.40**	**15.30**	**15.10**
Major elements (%)							
SiO_2	43.05	39.68	50.90	53.08	96.39	87.51	97.91
TiO_2	1.25	1.19	0.97	0.95	0.03	0.76	0.04
Al_2O_3	14.62	15.22	12.82	12.75	0.66	8.48	1.06
Fe_2O_3	17.73	19.62	14.76	13.39	2.41	0.14	0.33
MnO	0.23	0.28	0.21	0.18	0.01	0.00	0.00
MgO	9.98	11.16	5.79	4.78	0.24	0.06	0.12
CaO	3.78	3.02	8.88	9.95	0.05	0.04	0.05
Na_2O	0.72	0.03	1.27	0.82	<d.l.	0.04	<d.l.
K_2O	3.45	1.73	0.79	0.63	0.01	2.35	0.03
$P2O_5$	0.06	0.08	0.07	0.06	0.01	0.00	0.01
LOI	5.43	8.27	3.42	3.26	1.32	1.31	0.63
Sum	**100.34**	**100.32**	**99.91**	**99.87**	**101.15**	**100.75**	**100.18**
Trace elements (ppm)							
Sc	41.6	38.3	32.8	32.4	25.2	24.2	10.4
V	465	398	341	337	56.5	195	22.4
Cr	148	134	115	116	91.9	398	69.1
Co	65.2	72.1	60.6	69.2	342	98.6	526
Ni	121	112	80.6	79.0	86.3	46.5	53.5
Cu	243	193	172	145	<d.l.	18.3	5.61
Zn	133	156	88.3	77.0	0.933	0.873	1.30
Ga	18.3	17.9	13.4	14.7	1.11	9.33	1.69
Rb	88.0	37.1	21.7	18.4	0.318	43.2	0.293
Sr	53.8	66.9	200	430	1.44	2.84	2.96
Y	22.5	18.3	18.6	18.3	1.56	2.17	2.03
Zr	58.2	53.2	46.2	47.0	4.14	37.6	7.12
Nb	3.12	2.96	2.36	2.43	0.792	2.22	1.12
Cs	3.49	1.03	0.548	0.463	0.017	0.419	<d.l.
Ba	130	62.8	24.9	18.9	4.50	46.6	7.70
La	1.75	2.14	2.62	3.08	0.186	0.287	1.19
Ce	6.60	7.12	7.47	8.46	0.457	0.798	3.14
Pr	1.15	1.22	1.22	1.28	0.057	0.100	0.288
Nd	6.91	6.88	6.63	7.18	0.251	0.416	1.07
Sm	2.33	2.23	2.12	2.03	0.096	0.156	0.315
Eu	0.744	0.695	0.774	0.933	0.067	0.107	0.143
Gd	3.14	2.97	2.61	2.64	0.311	0.300	0.434
Dy	3.98	3.64	3.30	3.12	0.254	0.494	0.366
Ho	0.841	0.687	0.697	0.669	0.053	0.088	0.089
Er	2.43	1.98	2.11	1.97	0.161	0.224	0.197
Yb	2.68	2.08	1.99	2.06	0.170	0.190	0.212
Lu	0.404	0.318	0.316	0.285	0.022	0.024	0.021
Hf	1.69	1.48	1.29	1.32	0.103	1.02	0.186
Ta	0.248	0.307	0.476	0.667	3.83	1.28	5.36
Pb	0.702	1.32	1.61	2.79	<d.l.	<d.l.	0.072
Th	0.251	0.238	0.200	0.235	0.246	0.176	0.454
U	0.062	0.052	0.054	0.063	0.122	0.073	0.139
Sum REE	33.0	32.0	31.9	33.7	2.1	3.2	7.5
Eu/Eu*	1.25	1.23	1.51	1.84	1.46	2.13	1.75
Y/Ho	26.7	26.6	26.7	27.4	29.5	24.7	22.8
Al_2O_3/TiO_2	11.70	12.79	13.22	13.42	22.00	11.16	26.50

Table 1S (Continued)

	KROMBERG (continued)							
	Silicified basalt	Chert-vein	Chert		Silicified basalts			Unsilici
Sample code	**AK3***	**AK13**	**AK2**	**AK14**	**AK7***	**AK11***	**AK1***	**AK10**
Description	sil. pb.	bl. chert-vein	bl. Chert	bl/w chert	sil. pb.	sil. pb.	sil. pb.	unsil.
Depth (m)	-10	-12	-29	-25	-32	-46	-64	-131
δ^{30}Si (‰)	**0.63**	**0.40**	**-0.15**	**-0.35**	**0.74**	**0.65**	**-0.22**	
δ^{18}O (‰)	**15.55**	**16.20**	**19.50**	**16.50**	**15.09**	**15.58**	**9.99**	
Major elements (%)								
SiO_2	84.82	97.91	100.13	98.04	84.82	81.17	76.75	
TiO_2	1.01	0.05	0.01	0.01	0.85	0.84	1.15	
Al_2O_3	10.82	1.13	0.10	0.12	9.98	10.88	12.72	
Fe_2O_3	0.35	0.35	0.40	1.23	0.41	2.12	1.58	
MnO	0.00	0.00	0.03	0.04	0.00	0.01	0.05	
MgO	0.12	0.11	0.07	0.13	0.18	0.63	0.81	
CaO	0.05	0.08	0.05	0.11	0.05	0.05	0.37	
Na_2O	0.00	<d.l.	<d.l.	<d.l.	0.58	0.19	0.10	
K_2O	0.40	0.09	0.02	0.01	1.32	2.35	3.32	
$P2O_5$	0.03	0.04	0.00	0.04	0.01	0.01	0.06	
LOI	2.46	0.87	1.43	0.93	1.98	2.25	2.80	
Sum	**100.14**	**100.64**	**102.24**	**100.67**	**100.25**	**100.58**	**99.81**	
Trace elements (ppm)								
Sc	28.2	9.8	6.50	8.72	20.2	25.7	27.4	
V	216	31.0	3.11	13.4	228	280	306	
Cr	528	87.4	26.6	62.7	937	463	606	
Co	123	199	370	449	64.8	63.0	62.0	
Ni	72.6	30.5	18.3	37.6	42.7	125	90.9	
Cu	1.56	3.33	2.36	11.6	2.42	19.6	20.1	
Zn	0.850	0.960	0.985	1.30	0.635	3.53	2.00	
Ga	10.3	0.783	0.325	0.678	10.1	14.6	14.0	
Rb	6.83	0.773	0.766	1.42	24.7	57.0	74.9	
Sr	6.41	4.86	3.86	4.96	19.7	22.1	33.0	
Y	9.63	8.27	0.84	2.24	2.01	4.78	13.8	
Zr	52.3	9.66	2.35	2.93	50.0	47.0	62.0	
Nb	2.85	0.753	0.536	0.728	2.53	2.46	3.59	
Cs	0.142	0.025	0.044	0.047	0.455	1.10	1.05	
Ba	14.5	9.13	9.16	8.63	28.9	57.1	125	
La	8.10	1.75	0.266	1.61	0.740	1.39	7.73	
Ce	22.3	3.94	0.635	3.69	2.12	4.18	21.8	
Pr	2.50	0.439	0.068	0.419	0.265	0.541	2.85	
Nd	10.4	1.88	0.317	1.93	1.28	2.38	13.6	
Sm	2.77	0.624	0.117	0.532	0.336	0.694	3.56	
Eu	1.25	0.318	0.030	0.227	0.186	0.281	1.05	
Gd	2.35	1.32	0.159	0.650	0.364	1.01	3.31	
Dy	2.14	1.81	0.122	0.392	0.430	1.24	2.82	
Ho	0.403	0.300	0.034	0.211	0.083	0.264	0.572	
Er	1.15	0.710	0.081	0.195	0.228	0.612	1.63	
Yb	0.950	0.455	0.082	0.132	0.230	0.576	1.58	
Lu	0.149	0.059	0.018	0.015	0.033	0.084	0.232	
Hf	1.47	0.204	0.074	0.064	1.39	1.27	1.63	
Ta	1.04	2.88	4.18	5.07	1.02	0.715	0.615	
Pb	1.51	<d.l.	0.028	0.048	<d.l.	0.201	0.083	
Th	0.339	0.532	0.088	0.141	0.309	0.336	0.630	
U	0.177	0.119	0.075	0.092	0.112	0.134	0.362	
Sum REE	54.5	13.6	1.9	10.0	6.3	13.2	60.8	
Eu/Eu*	2.29	1.48	1.00	1.77	2.46	1.51	1.43	
Y/Ho	23.9	27.6	24.9	10.6	24.2	18.1	24.2	
Al_2O_3/TiO_2	10.71	22.60	10.00	12.00	11.74	12.95	11.06	

Major element concentrations were determined by X-ray fluorescence (XRF) spectrometry on fused discs of whole-rock powders. Both, major and trace elements were analysed at the University of Mainz, Germany.

Trace elements (Fig 1S), including rare earth elements (REE), were determined on glass beads by LA-ICP-MS formed by fusion whole-rock powders on an iridium strip heater. Due to the high silica content of chert samples (up to 97 wt. %) the samples were diluted with high purity MgO. Furthermore a higher fusion temperature and a prolonged melting duration were required to achieve homogenous melting of the powdered sample (Nehring et al., 2008). Samples with more than 70 wt% SiO_2 were fused at 1800 °C. Even the most siliceous samples yielded homogeneous clear, translucent glass beads at 1800 °C.

The analysis of the trace elements was conducted on an Agilent 7500ce quadrupole ICP-MS coupled with a NewWave Research UP-213 laser, following the protocol of Nehring et al. (2008). ^{43}Ca was used as internal standard for the reference materials and most samples, whereas ^{29}Si was used as internal standard for samples with less than 1 wt. % CaO. Certified glass reference material NIST SRM 612 served as the external standard and was measured at the beginning and at the end of each sample run. The elemental concentrations of NIST SRM 612 were taken from Pearce et al. (1997), except for Zr for which the preferred value given in the GeoReM database (Jochum et al., 2005) was used. The USGS reference glass BCR−2G was measured after every twelfth measurement. Reproducibility for the trace element concentrations was better than 5%. Data reduction was carried out using “Glitter” software. The average detection limits for the rare earth elements (REE) range from 3.7 (Lu) to 24.7 (Sm) ngg^{-1}. The samples were analyzed with a 100µm spot. Argon gas was used for the sample chamber.

Silicon stable isotopes are shown in a three isotope plot (Fig. 2S) to illustrate the data quality.

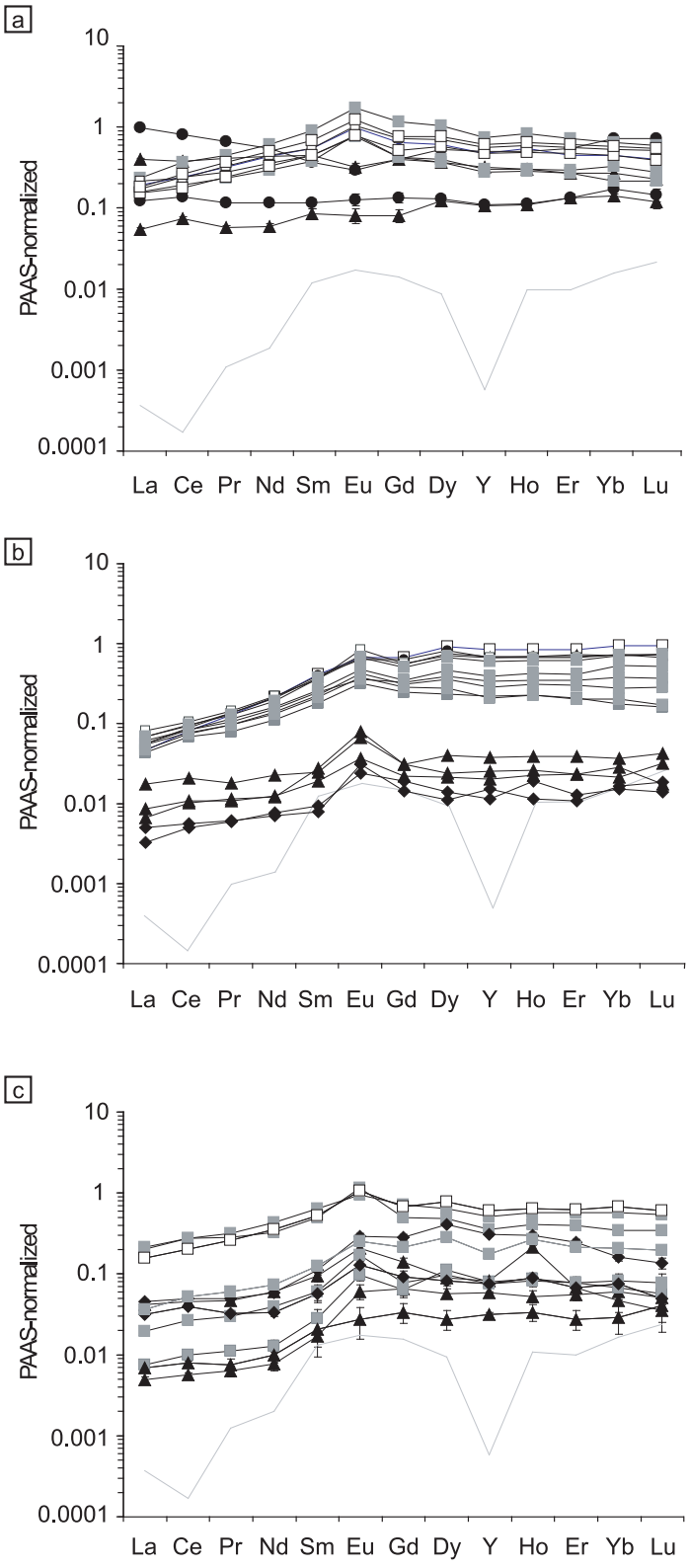

Fig. 1S: PAAS-normalized (Post-Archaean Australian Shales, Taylor and Mc Lennan, 1985) REE + Y pattern of (a) Theespruit Formation, (b) Hooggenoeg Formation and (c) Kromberg Formation. Grey curve represents the detection limit. The error bar is shown or included in the symbol size. The symbols refer to different rock types: white squares = unsilicified basalts; grey squares = silicified basalts; black triangles = chert; black diamonds = chert vein; black circles = felsic schist

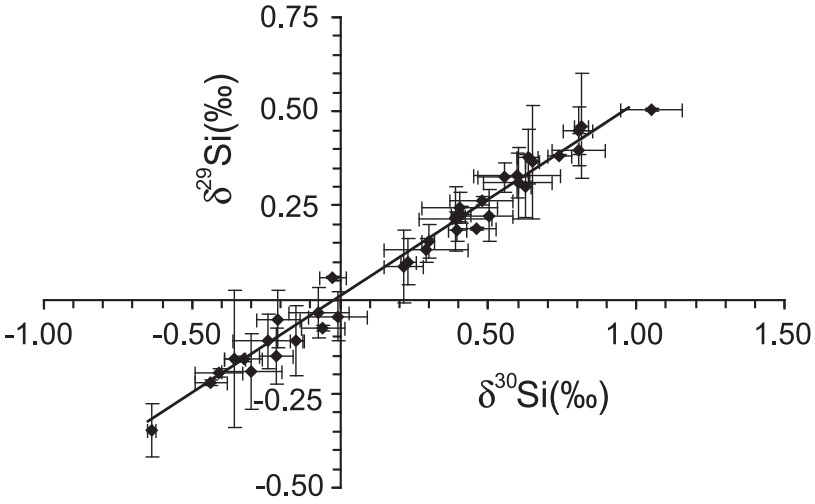

Fig. 2S: Three isotope plot, demonstrating that all data follow the mass-dependent equilibrium fractionation array ($\delta^{29}Si = \delta^{30}Si * 0.5178$) for Si. Error bars represent the standard deviation between the replicates.

6.2.S Calculations

6.2.1.S Calculation 1: Water-rock interaction

In order to investigate the role of water-rock interaction we calculated a hypothetical alteration curve with different water-rock ratios, referring to the oxygen and hydrogen isotope study of plutonic granitic rocks hydrothermally altered by meteoric water (Taylor, 1978). To calculate the mass fractions (φ) in water□silicon (C_{water}^{Si} and C_{bas}^{Si}) and oxygen (C_{water}^{0} and C_{bas}^{0}) concentrations we used the following equations (Albarède, 1995):

$$\varphi_{water}^{Si}=Q(C_{water}^{Si}/C_{bas}^{Si})/(Q(C_{water}^{Si}/C_{bas}^{Si})+1) \quad (1) \text{ and}$$
$$\varphi_{water}^{O}=Q(C_{water}^{O}/C_{bas}^{O})/(Q(C_{water}^{O}/C_{bas}^{O})+1) \quad (2)$$

whereby Q indicates several mass proportions of water (f_w) and rock (f_r) in the system ($Q=f_w/f_r$). The following equations include the Si and O isotope fractionation factor between quartz and water ($\Delta_{Qtz\text{-}H2O}$):

$$\delta^{30}Si_r=\varphi_{water}^{Si}(\delta^{18}Si_{water} + \Delta^{30}Si_{Qtz\text{-}H2O})+(1-\varphi_{water}^{Si})\delta^{18}Si_{bas} \quad (3) \text{ and}$$
$$\delta^{18}O_r=\varphi_{water}^{O}(\delta^{18}O_{water} + \Delta^{18}O_{Qtz\text{-}H2O})+(1 - \varphi_{water}^{O})\delta^{18}O_{bas} \quad (4)$$

Note that the calculation is performed for a constant temperature. For the calculation we need the following parameters: the fractionation of Si between quartz and water ($\Delta^{30}Si_{Qtz\text{-}H2O}$), the fractionation of O between quartz and water ($\Delta^{18}O_{Qtz\text{-}H2O}$), as well as the end-member compositions. We assume $\Delta^{30}Si_{Qtz\text{-}H2O} \approx -2.2‰$, based on the fractionation model of van den Boorn et al. (2010), as this values represents the difference in $\delta^{30}Si$ between their most negative chert sample (-2.4‰) and Phanerozoic hydrothermal fluids (-0.2‰). In

Table 2S: Results of the mixing calculation (Calculation 2S) shown in Fig. 4a/b for the selected values of chert fractions in the mixture.

a) Kromberg and Hooggenoeg					b) Theespruit				
f_{ch}	φ_{chert}^{Si}	$\delta^{30}Si_{mix}$	φ_{chert}^{O}	$\delta^{18}O_{mix}$	f_{ch}	φ_{chert}^{Si}	$\delta^{30}Si_{mix}$	φ_{chert}^{O}	$\delta^{18}O_{mix}$
0.00	0.00	-0.39	0.00	9.70	0.00	0.00	-0.17	0.00	9.51
0.05	0.09	-0.28	0.06	10.09	0.05	0.09	-0.12	0.06	9.63
0.10	0.18	-0.18	0.12	10.48	0.10	0.17	-0.08	0.12	9.75
0.15	0.26	-0.09	0.18	10.86	0.15	0.24	-0.03	0.17	9.87
0.20	0.33	-0.01	0.23	11.23	0.20	0.31	0.01	0.23	9.99
0.25	0.40	0.06	0.29	11.59	0.25	0.37	0.04	0.28	10.10
0.30	0.46	0.13	0.34	11.95	0.30	0.44	0.08	0.34	10.22
0.35	0.51	0.20	0.40	12.29	0.35	0.49	0.11	0.39	10.33
0.40	0.57	0.26	0.45	12.63	0.40	0.55	0.14	0.44	10.44
0.45	0.62	0.32	0.50	12.97	0.45	0.60	0.17	0.49	10.54
0.50	0.66	0.37	0.55	13.30	0.50	0.64	0.20	0.54	10.65
0.55	0.71	0.42	0.60	13.62	0.55	0.69	0.22	0.59	10.75
0.60	0.75	0.46	0.65	13.93	0.60	0.73	0.25	0.64	10.86
0.65	0.79	0.51	0.69	14.24	0.65	0.77	0.27	0.69	10.96
0.70	0.82	0.55	0.74	14.54	0.70	0.81	0.29	0.73	11.06
0.75	0.86	0.59	0.79	14.84	0.75	0.84	0.31	0.78	11.15
0.80	0.89	0.62	0.83	15.13	0.80	0.88	0.33	0.82	11.25
0.85	0.92	0.66	0.87	15.41	0.85	0.91	0.35	0.87	11.34
0.90	0.95	0.69	0.92	15.69	0.90	0.94	0.37	0.91	11.44
0.95	0.97	0.72	0.96	15.96	0.95	0.97	0.39	0.96	11.53
1.00	1.00	0.75	1.00	16.23	1.00	1.00	0.40	1.00	11.62

general, Δ is temperature-dependent and varies with pressure. We assumed $\Delta^{18}O_{Qtz\text{-}H2O}$ to be at least 20‰ representing a temperature of 100°C (Matsuhisa et al., 1979; Méheut et al., 2007), which is reasonable as higher temperatures are rather unlikely (see Chapter 6.5.4.).

The Si-O isotope ratios and concentrations of the basalt is the same as used in the calculation 2 (Fig. 4b). For the silicon and oxygen isotope value of the seawater, values of $\delta^{30}Si$=+4‰ and $\delta^{18}O$=-0.92‰ (Perry, 1967) were used. $\delta^{30}Si$=+1.1‰ (De La Rocha et al., 2000) for the seawater isotope value is not likely, since the fluid must be more positive than the chert precipitates. Following van den Boorn et al. (2010), adopting a maximum fractionation value of about –2.2 or –3 per mil, a higher Si isotope value of about +4‰ appear more realistic considering the cherts from this study have positive $\delta^{30}Si$ values. An oxygen concentration of seawater (C_{water}^{O}) of 89% (Taylor, 1978) was assumed. The estimation of the seawater Si concentration of the (C_{water}^{Si}) was problematic. We would expect a much larger content of amorphous silica than 49 ppm (cf. Gunnarson and Arnorsson, 2000). We assume a seawater SiO_2 concentration of 500 ppm (cf. Gunnarson and Arnorsson, 2000) which leads to a Si concentration of 230ppm, i.e. 0.023 wt %.

6.2.2.S Calculation 2: two end-member component mixing

We applied the ratio-concentration relationships in binary mixing (Albarède, 1995) to model a two-component mixing between basalt and chert. The calculation of the mass fractions of silicon and oxygen in chert, respectively is described by:

$$\varphi_{chert}^{Si}=(C_{ch}^{Si} f_{ch})/(C_{bas}^{Si} f_{bas}+C_{ch}^{Si} f_{ch}) \quad (5) \text{ and}$$

$$\varphi_{chert}^{O}=(C_{ch}^{O} f_{ch})/(C_{bas}^{O} f_{bas}+C_{ch}^{O} f_{ch}) \quad (6)$$

Using these equations (5) and (6), the φ_{chert}^{Si} and φ_{chert}^{O} values are calculated assuming several fractions of f and using the silicon concentrations of basalt (C_{bas}^{Si}) and chert (C_{ch}^{Si}) end-member and the oxygen concentrations of basalt (C_{bas}^{O}) and chert (C_{ch}^{O}) (noted in the Fig. 4).

With $\varphi_{bas}^{Si} + \varphi_{ch}^{Si} = 1$, the atomic binary mixing equations are then:

$$\delta^{30}Si_{mix}=\delta^{30}Si_{bas}*(1-\varphi_{ch}^{Si})+(\delta^{30}Si_{ch})*\varphi_{ch}^{Si} \quad (7) \text{ and}$$

$$\delta^{18}O_{mix}=\delta^{18}O_{bas}*(1-\varphi_{ch}^{O})+(\delta^{18}O_{ch})*\varphi_{ch}^{O} \quad (8)$$

Taking the φ -values and the end-member Si and O isotope signature (see Fig. 4a/b), the ratios in the hybrid rocks are computed for a few hybrid ratios with the equations (7) and (8) (supplementary Table 2S, Fig. 4a/b). Average values are used for the calculation of both end-members (basalt and chert), the in order to avoid extreme values, which might give an erroneous mixing trend.

Section IV

Development of granitoids in the Archaean

Chapter 7

Potential changes in the source of granitoids in the Archaean: the Si isotope perspective*

Abstract

We present silicon isotope measurements in conjunction with major and trace element analyses on different generations of "sodic" and "potassic" intrusive units from 3.55 to 3.10 Ga from the Barberton Mountain Land, South Africa.

"Sodic" plutons have a tonalitic to trondhjemitic composition, whereas "potassic" intrusive units are granitic. Additionally, K-rich plutons typically show differences to the Na-rich plutons, as indicated by major and trace element compositions (e.g. K_2O/Na_2O ratios close to 1.0 and higher Rb/Sr ratio) and more fractionated rare earth element pattern (REE), as "potassic" plutons show a small negative Europium anomaly and higher Yb_N at lower La/Yb_N.

An overall slight increase in $\delta^{30}Si$ with time in different generations of plutons is recorded by the K-rich plutons that yield the highest Si-isotope composition. The silicon (Si) isotope variation is likely dependent on the temperature of the source region of the granitoids, with K-rich, heavy $\delta^{30}Si$ granitoids emerging at lower temperatures. Owing to similarity in the Si-isotope signatures of Barberton K-rich granites to modern granitoids, we confirm that K-rich intrusive units of different origin shows no clear difference, from the present day back to 3.1 Ga.

*In parts adapted from: K. Abraham, A. Hofmann, S.F. Foley, D. Cardinal and André L (submitted). Potential changes in the source of Granitoids in the Archaean: the Si isotope perspective. 5th International Archaean Symposium, extended Abstract.

7.1. Introduction

Earth´s oldest crust constitutes rocks of the tonalite-trondhjemite-granodiorite (TTG) series tectonically interleaved with, or intrusive into, greenstone belts (Condie, 1981). The petrogenesis of TTGs, their geodynamic environment, their rate of formation, and lack of importance in post-Archaean times is still a matter of debate. In order to investigate the different hypotheses for their origin we combine silicon isotopes with major and trace element analyses on different generations of intrusive units from 3.55 to 3.10 Ga from the Barberton Mountain Land, South Africa.

In contrast to the Archaean, today's continental crust is more potassic in composition and shows differences in trace element characteristics (*e.g.* the enrichment of incompatible elements and a significant Eu anomaly). Processes that lead to this changeover from "sodic" to more "potassic" crust are the subject of considerable interest. With the investigation of the variations in Si isotope composition among the different generations of plutons in the Barberton Mountain Land (BML) we investigate the capability of silicon isotopes to trace this change to potassium rich plutonism. The BML is particularly suitable in this regard, because of its pristine character. Furthermore, the BML represents one of relatively few localities around the world (also Singhbhum craton, India), where the emplacement of K-rich plutons started earlier (~3.1 Ga) than in other places (~2.6 Ga).

Silicon isotopes could give further constraints on essential questions regarding the source of granitoids by discriminating between possible sources. The proposed geodynamic processes for the origin of TTGs are either melting of a subducted slab or melting of the lower part of thick, mafic crust in an intra-plate setting. Comparison of the isotope signatures of the TTG amongst different reservoirs provides further information about the possible contribution of sediments (cherts) and silicified basalts of the Archaean ocean floor, or from the mantle, and thus about the sources of TTG genesis.

Results from experimental petrology indicate that TTG rocks are produced by partial melting of a mafic source within the garnet stability field. The role of water during this process, determining whether the source consists of amphibolite (Foley et al., 2002) or eclogite (Rapp et al., 2003), can be tested by silicon isotopes, since Si isotopic variations originating from interaction with water have a much larger range than those of magmatic processes.

However, knowledge about mineral/melt Si isotope fractionation is very limited. Therefore we performed Si isotope analyses on different parts of migmatites from Finland (Nehring et al., 2009) to estimate a preliminary range of Si isotope fractionation during partial melt processes.

7.2. Geology

Nine samples were taken from four different generations of plutons (Figure 1) from the Barberton Mountain Land, South Africa. In general, the intrusive units can be subdivided in two major types of igneous rocks (Lowe and Byerly, 2007): The "sodic" TTG group (tonalite-trondhjemite-granodiorite) and the later "potassic" GMS group (granite-monzonite-syenite). The former rocks were generated in the interval between 3.5 and 3.2 Ga (Lowe and Byerly, 2007), whereas the latter formed at about 3.1 Ga (Kamo and Davis, 1994).

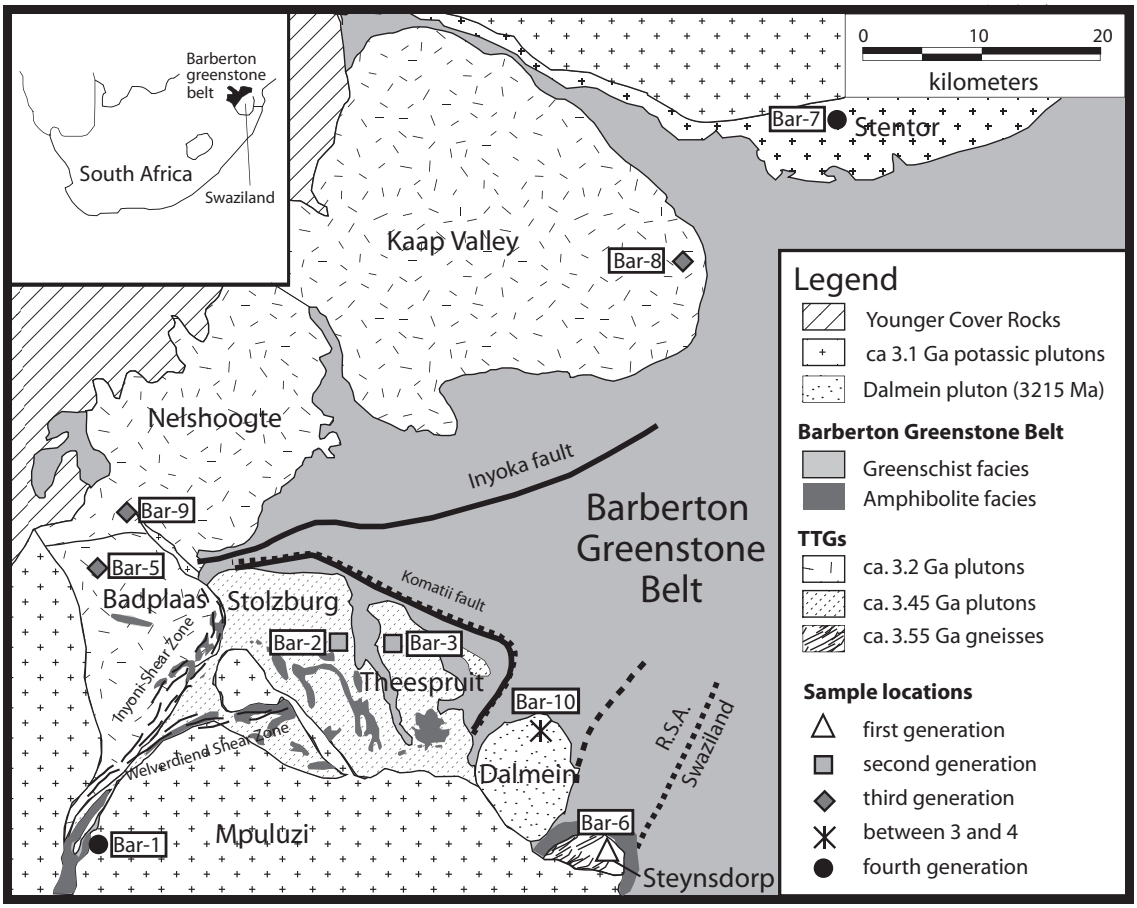

Figure 1. Simplified geological map of the Barberton Mountain Land (BML; South Africa), showing the sample locations (adapted from Moyen et al., 2007).

The emplacement of the different generations of pluton is considered to have been broadly coeval with the main deformation events (D1 to D4) recorded during the formation of the Barberton Mountain Land. A short description of the nine different plutons (Fig. 1) and their relation to the evolutionary stages of the BML is outlined below.

Some data suggest that even older tectono-magmatic cycles may have preceded the D1-Deformation due to the formation of foliation and gneissic textures in the *Steynsdorp Pluton* (3509 ± 8/7 Ma) (Kisters and Anhaeusser, 1995, Kröner et al., 1996; Kisters et al., 2003).The first accretion event (D1-Deformation) represents the earliest well-documented deformation event in the history of the Barberton Greenstone Belt (BGB). During the D1-event (3445 ± 4 and 3416 ± 7 Ma; de Wit, 1994), the Onverwacht oceanic rocks were suggested to be delaminated at an intra-oceanic subduction-like environment onto an active arc-like terrain (de Wit et al., 1987; de Ronde and de Wit, 1994; Cloete, 1999). This deformation event culminated in felsic magmatic activity in the form of the intrusion of the trondhjemitic suite (*Stolzburg and Theespruit Plutons*).

The D2-Deformation probably extended from about 3230 to 3225 Ma and represents a major period of convergent tectonism, with collisional suturing and the amalgamation of the BGB and Ancient Gneiss Complex terrains (de Wit, 1991; de Ronde and de Wit, 1994). The collision events coincide with intrusions of the TTG-granitoids, e.g. the *Badplaas Pluton* (3290-3240 Ma, Kisters et al., 2006) the *Nelshoogte Pluton* (3236 Ma ± 1, de Ronde and Kamo, 2000) and the *Kaap Valley Pluton* (3228 ± 1 Ma, Kamo and Davis, 1994). The *Dalmein Pluton* has a well-constrained age of 3216+2/-1 Ma (Kamo and Davis, 1994). It is regarded as late member of the 'ancient tonalites' suite.

The D3-Deformation was accompanied by the intrusion of GMS granitoids, such as *Stentor* and *Mpuluzi Batholiths* (3107 ± 5 and 3105 Ma, Kamo and Davis, 1994). The D3-event is broadly characterized by strike-slip and thrust faults. The D3-shear zones were interpreted as a consequence of a transtensional deformation-event (de Ronde and de Wit, 1994; Kamo and Davis, 1994). We refer to Moyen et al. (2007) and references therein for a more detailed geological overview of the study area.

7.3. Results

Major element and Si isotope compositions for TTG and GMS of the Barberton Mountain Land are presented in Table 1. Trace element compositions are shown in Table 2. X-ray fluorescence (XRF) (major elements) and ICP-MS (trace elements) analyses were performed at the University of Mainz, Germany, and followed standard procedures (Nehring et al., 2008).

Table 1. Major element concentrations and silicon isotope composition of Barberton plutonites

Sample	**Bar-6**	**Bar-2**	**Bar-3**	**Bar-9**	**Bar-5**	**Bar-8**	**Bar-10**	**Bar-7**	**Bar-1**
Description	trondhjemite	trondhjemite	trondhjemite	trondhjemite	trondhjemite	tonalite	trondhjemite	granite	granite
Age (Ga)	3.55	3.45	3.45	3.236	3.26	3.226	3.216	3.107	3.105
Locality	Steynsdorp	Stolzburg	Theespruit	Nelshoogte	Badplaas	Kaap Valley	Dalmein	Stentor	Mpuluzi
Generation	first	second	second	third	third	third	between 3/4	fourth	fourth
Stable isotopes (‰)									
δ^{30}Si	**-0.17**	**-0.10**	**-0.11**	**-0.12**	**0.05**	**-0.08**	**0.02**	**0.02**	**-0.04**
n	2	2	2	2	2	2	2	2	2
stand dev δ^{30}Si	0.02	0.02	0.08	0.11	0.07	0.04	0.11	0.14	0.06
average δ^{30}Si of pluton generation	**-0.17**		**-0.11**			**-0.05**	**0.02**		**-0.01**
Major elements (wt.%)									
SiO_2	71.78	73.64	71.09	71.80	70.59	64.12	70.40	74.15	69.08
TiO_2	0.31	0.15	0.23	0.27	0.24	0.51	0.31	0.15	0.51
Al_2O_3	14.79	14.50	15.21	14.99	15.84	15.52	14.85	13.94	14.52
Fe_2O_3	2.55	1.25	1.96	2.16	2.20	4.40	2.33	1.59	3.31
MnO	0.04	0.02	0.03	0.03	0.03	0.06	0.05	0.04	0.07
MgO	0.56	0.30	0.87	0.69	0.72	2.70	0.75	0.18	0.60
CaO	2.36	1.66	2.20	2.85	3.05	4.50	1.90	0.88	1.49
Na_2O	4.70	5.13	5.50	4.98	5.28	4.65	4.99	4.49	4.03
K_2O	2.16	2.62	2.01	1.28	0.81	1.16	2.72	3.77	4.46
P_2O_5	0.07	0.03	0.06	0.08	0.08	0.16	0.15	0.03	0.16
LOI	0.51	0.26	0.58	0.53	0.98	2.25	1.15	0.47	0.93
Sum	**99.83**	**99.55**	**99.75**	**99.66**	**99.80**	**100.04**	**99.62**	**99.70**	**99.18**

Table 2: Trace element composition of Barberton TTG and GMS

Sample	**Bar-6**	**Bar-2**	**Bar-3**	**Bar-9**	**Bar-5**
Description	trondhjemite	trondhjemite	trondhjemite	trondhjemite	trondhjemite
Age (Ga)	3.55	3.45	3.45	3.236	3.26
Locality	Steynsdorp	Stolzburg	Theespruit	Nelshoogte	Badplaas
Generation	first	second	second	third	third
Trace elements (ppm)					
Li	162	30.2	44.1	41.5	19.1
Be	1.70	1.22	1.82	0.60	0.80
Sc	4.93	3.29	4.48	3.51	3.79
V	16.4	6.60	16.3	20.4	13.9
Cr	8.62	4.82	14.4	7.38	2.93
Co	109	98.3	114	101	113
Ni	8.71	4.90	23.3	10.7	3.55
Cu	13.6	8.38	11.6	11.7	8.37
Zn	59.2	10.5	34.0	28.7	16.1
Ga	21.0	16.1	19.4	17.1	15.9
Ge	0.95	0.42	0.62	0.79	0.78
Rb	53.2	51.7	75.4	37.2	28.4
Sr	301	502	495	498	521
Y	13.8	2.20	6.21	2.56	2.59
Zr	106	44.8	111	106	91.0
Nb	8.98	2.67	6.01	2.17	2.48
Mo	0.45	0.22	0.32	0.34	0.24
Cs	3.30	1.45	2.46	1.52	0.71
Ba	391	1165	387	164	122
La	23.6	9.29	18.9	24	14.2
Ce	47.2	18	33.8	45.6	27.4
Pr	4.86	1.94	3.33	4.30	2.66
Nd	17.8	6.81	11.3	14.3	9.14
Sm	3.22	1.11	1.99	1.97	1.40
Eu	0.78	0.35	0.51	0.62	0.48
Gd	2.72	0.76	1.56	1.10	0.92
Dy	2.40	0.42	1.11	0.57	0.56
Ho	0.50	0.08	0.22	0.10	0.09
Er	1.33	0.19	0.58	0.27	0.26
Yb	1.29	0.17	0.66	0.24	0.22
Lu	0.20	0.03	0.10	0.05	0.03
Hf	2.87	1.45	3.42	2.64	2.34
Ta	n.a.	n.a.	n.a.	n.a.	n.a.
Pb	8.99	1.55	8.22	3.11	2.12
Th	5.87	1.74	6.33	2.59	2.03
U	1.10	0.49	2.08	1.68	0.30
K_2O/Na_2O	0.46	0.51	0.37	0.26	0.15
Na_2O/CaO	1.99	3.09	2.50	1.75	1.73
#Mg	0.18	0.19	0.31	0.24	0.25
Sr/Y	21.7	228	79.7	195	201
$(La/Yb)_N$	13.1	38.8	20.5	73.0	45.6
Eu*	0.78	1.10	0.85	1.17	1.21

Table 2 (continued)

Sample	**Bar-8**	**Bar-10**	**Bar-7**	**Bar-1**
Description	tonalite	trondhjemite	granite	granite
Age (Ga)	3.226	3.216	3.107	3.105
Locality	Kaap Valley	Dalmein	Stentor	Mpuluzi
Generation	third	between	fourth	fourth
Trace elements (ppm)				
Li	24.8	34.4	19.7	69.1
Be	0.95	2.07	2.94	2.36
Sc	8.16	4.61	3.91	8.19
V	76.6	25.0	5.85	25.1
Cr	68.5	9.09	2.47	9.12
Co	70.8	108	112	87.5
Ni	53.3	7.25	2.73	6.13
Cu	19.7	7.30	14.5	35.4
Zn	29.0	11.1	16.3	56.0
Ga	17.7	18.1	17.5	23.0
Ge	0.71	0.71	0.65	1.54
Rb	32.8	91.1	127	230
Sr	499	479	244	236
Y	7.27	12.3	12.0	33.8
Zr	59.9	128	150	318
Nb	3.68	10.8	10.4	46.6
Mo	0.27	0.25	0.25	0.46
Cs	2.23	1.79	3.97	5.35
Ba	204	574	913	1190
La	22.4	51.3	62.0	168
Ce	45.4	103	121	337
Pr	4.58	10.2	12.4	32.5
Nd	16.3	33.8	42.4	104
Sm	2.70	5.25	6.82	15.6
Eu	0.88	1.37	1.35	1.72
Gd	2.16	3.72	4.44	10.6
Dy	1.46	2.36	2.56	7.61
Ho	0.29	0.48	0.46	1.35
Er	0.70	1.15	1.10	3.24
Yb	0.67	1.11	1.07	2.69
Lu	0.09	0.17	0.17	0.38
Hf	1.67	3.37	4.69	7.44
Ta	n.a.	n.a.	n.a.	n.a.
Pb	2.42	3.05	8.06	8.90
Th	2.65	8.88	18.1	15.5
U	0.60	2.42	2.58	3.06
K_2O/Na_2O	0.25	0.55	0.84	1.11
Na_2O/CaO	1.03	2.63	5.10	2.70
#Mg	0.38	0.24	0.10	0.15
Sr/Y	68.6	39.0	20.3	6.97
$(La/Yb)_N$	24.1	33.3	41.7	44.8
Eu*	1.08	0.90	0.70	0.39

7.3.1. Major and trace elements

The Barberton TTG group rocks are trondhjemitic or tonalitic in composition and show no discernible temporal variation in their major element compositions. The two granites of the GMS group can be distinguished from the TTG group by their potassium content (average K_2O: TTG = 1.8 wt. %; GMS = 4.1 wt. %). In general, modern granitoids are typically granodioritic or granitic in composition with K_2O/Na_2O ratios close to 1.0, whereas Archaean TTG granitoids show no K-enrichment during magmatic differentiation and are more sodic with K_2O/Na_2O ratios lower than 1. The higher K_2O-content in the GMS group give K_2O/Na_2O ratios (average K_2O/Na_2O = 0.97) similar to modern granitoids, whereas the Archaean TTG show typically low K_2O/Na_2O ratios (average K_2O/Na_2O = 0.36).

In a normative An-Ab-Or diagram (Fig. 2) (O'Connor, 1965; Barker, 1979) the sodic character of the TTG and the potassic character of the GMS is clear. SiO_2 contents range from 64.1 to 74.2 wt. %. Generally, the MgO content is very low in all plutonites (average MgO = 0.6 wt. %), except for the Kaap Valley plutonite, which has a higher MgO concentration (average MgO = 2.7wt. %). TTGs are poor in ferromagnesian (Fe_2O_3*+MgO+MnO+TiO_2<5 wt. %), with an average Mg# (MgO/(MgO+FeO)) of 0.26 and average Ni and Cr contents of 16 ppm. In contrast, the Kaap Valley plutonite has a much higher Ni+Cr content of 122ppm. Additionally, GMS group rocks show typical differences to the TTG with respect to their trace element composition (e.g. GMS have higher Rb/Sr ratios to TTG).

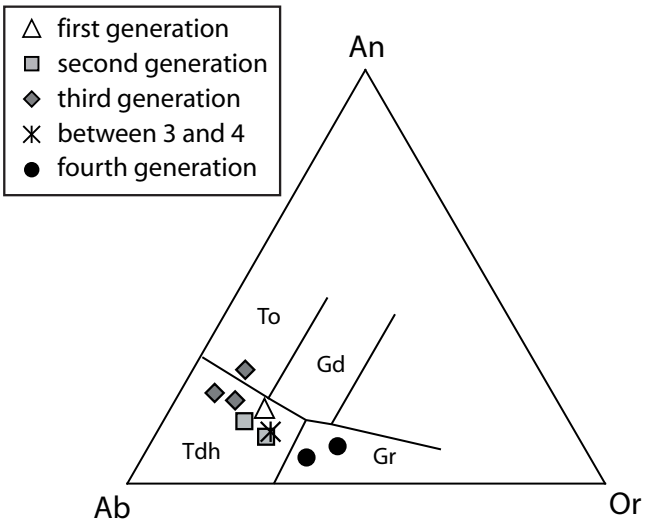

Fig. 2: O`Connor (1965) An-An-Or-diagram showing the fields (from Barker, 1979) of tonalites (To), trondhjemites (Tdh), granodiorites (Gd) and granites (Gr). TTG group rocks are typically distributed near the triple junction of the tonalitic, trondhjemitic and granodioritic fields. TGGs of this study are all trondhjemitic or tonalitic in composition. The two samples of GMS group plot in the granite field, consistent with their potassic character.

The multi-element diagram of Fig. 3 shows trace element variations normalized to the primitive mantle values of Sun and McDonough (1989). As is common for TTG-like rocks, this plot shows considerable enrichment in large ion lithopihle elements (LILEs), a negative Nb anomaly and no significant enrichment in Dy, Y and Yb. Ti displays a negative anomaly in some rocks. Compared to TTG rocks, GMS rocks exhibit significantly higher enrichment

for all the elements shown in Fig 3. Trace element pattern for TTG rocks are similar to those of GMS, except for the Sr content, which varies considerably between samples. The Sr-content can be controlled by plagioclase, either as a residual or fractionating phase.

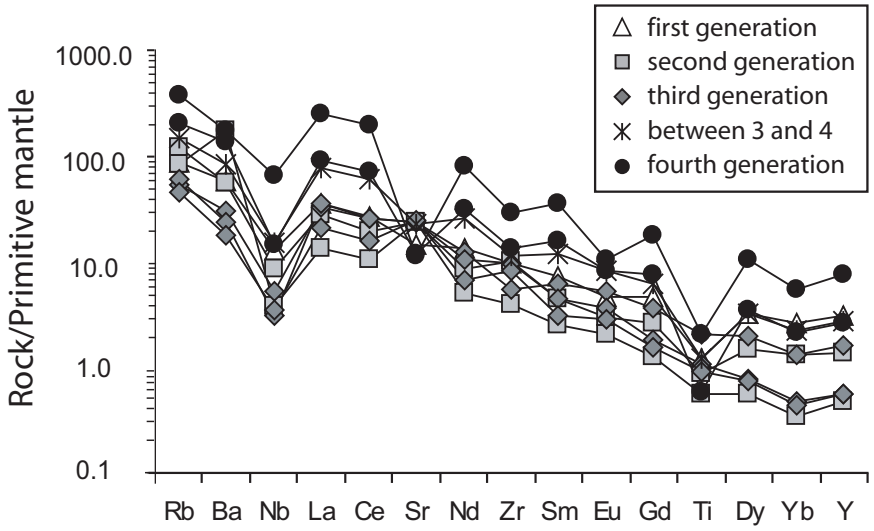

Fig. 3: Primitive mantle normalized trace element pattern for TTG and GMS group plutonites (symbols as in Figure 2), GMS are strongly fractionated. Patterns of TTG are similar to those of GMS, with the exception of Sr-content. The enrichment of trace elements Rb, Ba and the LILEs, a negative Nb anomaly is typical for crustal rocks. The overall similarity between both groups suggests similar processes operated during their petrogenesis. Normalising parameters from Sun and McDonough (1989).

Fig. 4 shows rare earth element (REE) patterns for samples from TTG and GMS plutons from Barberton. TTGs display strongly fractionated REE patterns, which are generally steeper (with higher $(La/Yb)_N$ up to 70, Figure 5) than GMS pattern. Depletion in the heavy REE with respect to chondritic concentrations is usually interpreted as a source-related feature owing to preferential partitioning of these elements into coexisting garnet in the restite.

GMS shows a small negative europium anomaly (Eu* values of 0.39–0.70), likely suggesting a degree of plagioclase fractionation. The Dalmein pluton yields trace element and REE compositions intermediate between the TTG and GMS groups.

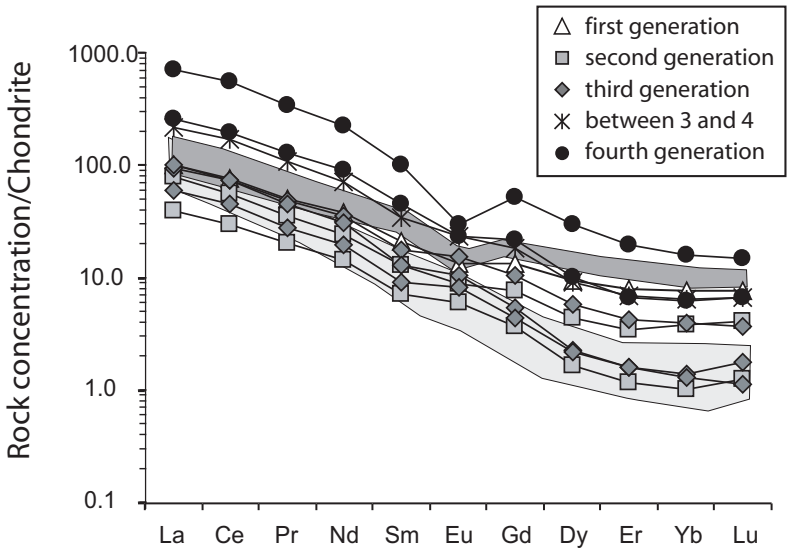

Fig. 4: Chrondrite normalized REE pattern for TTG and GMS. Pale grey field represents the REE pattern for Archaean TTGs and the dark grey field shows typical REE patterns of post-Archaean granitoids (data from Martin, 1993). Normalization factors from Sun and McDonough, 1989).

Figure 5 illustrates the chondrite-normalised La/Yb ratios ($(La/Yb)_N$) of the Barberton granitoids. It highlights the fact that the TTG have low Yb_N values and evolved $(La/Yb)_N$ ratios, typical of Archaean TTGs (Martin, 1986). In contrast, GMS have intermediate $(La/Yb)_N$ and show higher Yb_N.

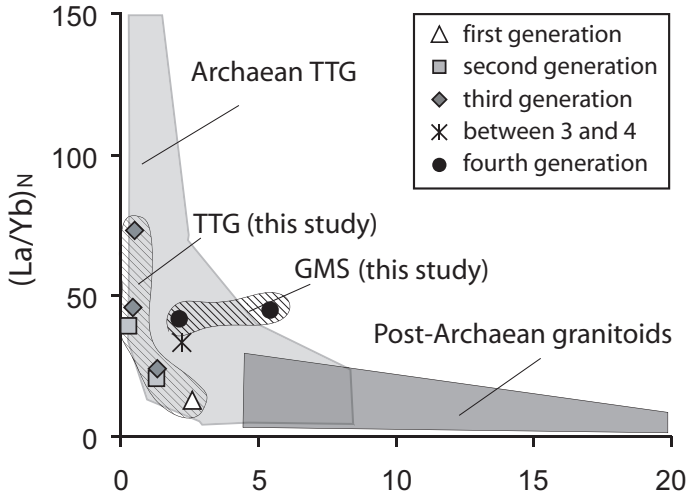

Fig. 5: $La_N/Yb_N - Yb_N$ diagram for the TTG and GMS rocks. TTG group rocks follow a low Yb_N trend with increasing La_N/Yb_N for different generations, with low La_N/Yb_N in the first generation. Archaean TTGs (pale grey field) and post-Archaean granitoids (for and the dark grey field) are shown for comparison (data from Martin, 1993). GMS plot near the Archaean TTG field; in contrast to TTG these show higher Yb_N at intermediate La_N/Yb_N.

Preliminary results of major and trace elements and Si isotope composition of migmatites from Finland are shown in Table 3. Leucosomes, melanosomes and mesocratic parts of two different migmatites from Finland were investigated. Migmatite are in parts described by Nehring et al. (2009) (Jonsa location, sample 76*).

Table 3: major and trace element composition and Si isotope concentration of migmatites from Finland

Sample	**061-04 L**	**061-04 ME**	**061-04 M**	**076-04 L**	**076-04 a**	**076-04 M**
Description	leucosome	mesosome	melanosome	leucosome	mesosome	melanosome
Locality	Pällikäs	Pällikäs	Pällikäs	Jonsa	Likomäki	Jonsa
Age (Ga)	2.68-2.63	~3.2 (?)	~3.2 (?)	2.68-2.63	~ 2.7	2.75-2.7
Stable isotopes (‰)						
δ^{30}Si	**-0.25**	**-0.11**	**-0.44**	**-0.27**	**-0.28**	**-0.50**
n	2	3	3	4	5	3
stand dev δ^{30}Si	0.04	0.09	0.06	0.11	0.11	0.06
Major elements (wt.%)						
SiO_2	62.27	54.71	44.86	66.20	51.64	51.85
Al_2O_3	22.56	22.65	13.40	13.32	15.66	14.63
Fe_2O_3	0.33	4.22	14.64	11.79	8.99	12.63
MnO	0.01	0.06	0.22	0.54	0.16	0.17
MgO	0.04	2.11	10.18	2.68	7.92	6.03
CaO	4.18	8.07	10.67	4.28	11.61	9.58
Na_2O	7.87	5.84	2.46	1.64	2.51	3.07
K_2O	1.36	0.61	0.89	0.21	0.23	0.72
TiO_2	0.03	0.58	1.20	0.13	0.43	0.85
P_2O_5	0.02	0.14	0.45	0.03	0.05	0.10
Cr_2O_3	0.00	0.00	0.05	0.00	0.00	0.00
NiO	d.l.	0.00	0.02	d.l.	0.01	0.00
LOI	0.52	0.34	0.67	0.01	0.46	0.27
Sum	**99.19**	**99.34**	**99.71**	**100.83**	**99.67**	**99.91**
Trace elements (ppm)						
Sc	23.0	13.0	45.0	24.0	37.0	36.0
V	148	72.0	286	61.0	161	235
Cr	72.0	34.0	324	4.00	16.0	6.00
Ni	44.0	25.0	173	3.00	49.0	22.0
Rb	16.0	13.0	24.0	3.00	3.00	5.00
Sr	900	1142	243	172	252	290
Y	21.0	10.0	38.0	84.0	13.0	16.0
Zr	120	31.0	52.0	67.0	44.0	85.0
Nb	3.68	3.19	5.41	0.44	4.00	3.09
Ba	142	172	83.0	106	69.0	147
La	14.2	9.12	16.3	5.00	4.99	10.0
Ce	47.3	20.9	60.8	4.85	11.7	29.8
Pr	6.64	2.97	9.8	0.36	1.56	3.31
Nd	29.8	13.8	47.9	1.77	6.55	14.4
Sm	6.52	2.75	10.4	0.71	1.53	3.12
Eu	1.65	1.10	2.68	0.32	0.57	0.89
Gd	5.20	2.21	8.35	2.31	1.50	3.13
Dy	3.61	1.67	6.10	9.5	1.60	2.93
Er	1.77	0.83	3.05	16.0	0.95	1.64
Yb	1.52	0.77	2.84	23.8	0.97	1.46
Lu	0.23	0.10	0.38	9.43	0.16	0.22
Hf	2.81	0.48	1.34	1.27	0.68	2.42
Ta	0.17	0.08	0.28	0.05	0.09	0.18
Th	n.a.	0.08	0.32	n.a.	0.05	n.a.
U	n.a.	0.08	0.44	0.02	0.05	0.11

7.3.2 Silicon stable isotope variations

Silicon isotope variations are presented in per mil variation relative to the NBS28 quartz standard. Details about the preparation procedure and the analytical method can be found in Abraham et al., 2008. Overall, the plutons show very limited variation ($\delta^{30}Si$ = -0.17‰ to +0.05‰, average $\delta^{30}Si$ = -0.06‰, n = 9). The isotope composition of the Barberton plutons is comparable with granitoids analyzed so far, which range between -0.8‰ and +0.4‰ (average $\delta^{30}Si$ = -0.10‰, n = 44; Douthitt, 1982, Ding et al., 1996). André et al. (2006) identified slightly heavier $\delta^{30}Si$ values ($\delta^{30}Si$ = -0.04‰ to +0.41‰, average $\delta^{30}Si$= +0.23‰, n = 5) in high-grade early Archaean tonalitic crustal gneisses (Amîtsoq, Isua). A small but progressive temporal increase in $\delta^{30}Si$ between the different pluton generations in Barberton (average $\delta^{30}Si$ values from the first to the fourth generation, $\delta^{30}Si$ = -0.17‰, $\delta^{30}Si$ = -0.11‰, $\delta^{30}Si$ = -0.05‰ and $\delta^{30}Si$ = +0.01‰, respectively) is apparent, but is not much larger than the average standard deviation between the replicates (0.071‰).

Preliminary results for leucosomes, melanosomes and mesocratic parts of two different migmatites from Finland indicate a small range of fractionation during the melting process: $\Delta_{leuco\text{-}melano}{}^{30}Si$ = 0.23‰ and $\Delta_{leuco\text{-}melano}{}^{30}Si$ = 0.33‰, showing that the leucocratic melt is isotopically heavier than the restite (Table 3).

7.4. Discussion

Our knowledge about silicon isotopes in felsic igneous rocks is still very limited due to the small number of studies conducted to date (Douthitt, 1982; Ding et al., 1996, Andrè et al., 2006). The different processes that account for Si isotope fractionations during granitoid genesis are summarized here.

7.4.1. Si isotope fractionation during magmatic differentiation, partial melting and fractional crystallization

In general, the isotope fractionation during magmatic differentiation is expected to be small because of the high temperatures. Grant (1954) suggested on the basis of theoretical calculations that equilibrium Si isotope fractionation should depend on the degree of polymerization of the silicate unit. This is confirmed by observations on natural rocks, since felsic igneous rocks (~0‰) show slightly heavier isotope composition than mafic rocks (-0.3‰) (Douthitt, 1982, Ding et al., 1996). Due to the fact that $\delta^{30}Si$ generally increases with silicon contents of rocks, it was assumed that with progressive magmatic differentiation the isotope signature should evolve to higher values. However, recent theoretical calculations on equilibrium isotopic fractionation of oxygen and silicon for several minerals, displaying

various degrees of polymerization of silicate tetraedra (Méheut et al., 2009), indicate that the fractionation factor of Si in equilibrium does not strictly follow the degree of polymerisation of silicate tetraedra previously suggested.

There is only limited knowledge about Si isotope fractionation during partial melting. Given that migmatites and felsic igneous rocks fall in the same $\delta^{30}Si$ range, it has been hypothesized that the $\delta^{30}Si$-values remain unchanged during the formation of migmatites (Ding et al., 1996, André et al., 2006). However, our preliminary results on migmatites of Finland suggest that there is a variation (max. $\Delta^{30}Si = 0.33‰$) for the partial melting process.

Fractional crystallization of minerals can lead to a change in isotope composition of the melt. In general, the equilibrium isotope fractionation between silicate minerals pairs in igneous rocks (feldspar-hornblende, quartz-feldspar, and feldspar-pyroxene) generates only small isotope fractionations of 0.2-0.5‰ (Ding et al., 1996), so that the resulting variation is expected to be small. This result is justified by theoretical calculations (Méheut et al., 2009). As deduced by Epstein and Taylor (1970), the isotope fractionation sequence, meaning the preference for ^{30}Si, among coexisting mineral phases is (pyroxene, biotite, hornblende) < (plagioclase, K-feldspar) < (quartz, cristobalite). The fractional crystallization of mafic minerals would lead to an evolution to higher values in the residual (quartz- and plagioclase-rich) melt. It is known that trondhjemite can result from fractional crystallization of a tonalite parental magma. Operation of this process would lead to relatively higher $\delta^{30}Si$ in trondhjemites and lower $\delta^{30}Si$ in tonalites within the different Barberton TTG plutons.

7.4.2. The water content and the involvement of sediment in the source

The resemblance of Archaean K-rich granites (3.1 Ga) with Middle Paleozoic (0.45 to 0.34 Ga) granites from Australia (Douthitt, 1982) and young (< 0.5 Ga) granitoids from China (Ding et al., 1996), suggests that the processes which would lead to a large fractionation of silicon isotopes, such as the influence of water during magma genesis or the assimilation of other material (sediments such as clays with strong negative ^{30}Si values) are affecting late Archaean and Phanerozoic granitoids equally. Douthitt (1982) detected no difference between S-type (supracrustal source) and I-type (igneous source) granitoids, which hints at no significant effect of the involvement of sedimental material on the Si isotope signature.

7.4.3. Si isotope fractionation during diffusion

The experimentally determined thermal Si isotopic fractionation in molten basalt is $\Omega_{Si} = 0.6$, whereby the parameter Ω_i defines the isotopic fractionation in per mil per 100 °C per atomic mass unit (Richter et al., 2009). Thus, in a temperature gradient, the cold end-member of the molten basalt would become enriched in $\delta^{30}Si$, with a surprisingly large degree of isotope fractionation.

7.4.4. Temperature differences in the source of granitoids

Magmatic differentiation and fractional crystallization of tonalitic parental magmas causes enrichment in sodium. Thus K_2O-rich granites must emerge from different source rocks to tonalites. It is generally known that granitic melts form at lower temperatures (650 °C to 700°C) than tonalitic melts (Wyllie, 1977). The enrichment of ^{30}Si by diffusion in cold melts (Richter et al., 2009) fits very well with the different formation temperatures. The overall increase in ^{30}Si from early ($\delta^{30}Si = -0.17$) to late granitoids ($\delta^{30}Si = +0.01$) in Barberton and the concomitant K_2O-enrichment may reflect different formation temperatures for the different granitoid generations. This means that K-rich melt, which emerges at colder temperatures shows higher isotope composition than Na-rich melt. The slightly higher isotope composition of 3.8 Ga Amîtsoq gneisses (average $\delta^{30}Si = +0.23‰$, n = 5), might be attributed to higher strain or other formation conditions during the early Archaean.

7.5. Conclusion

There is an overall slight increase in $\delta^{30}Si$ with time in different generations of plutons in the BML. The Si isotope variation characterizes different temperature conditions in the source of granitoids, with K-rich, heavy $\delta^{30}Si$ granitoids emerging at lower temperatures. We confirm that similarity in the Si-isotope signatures of K-rich granites of different origins shows no clear difference and that this similarity extends back to 3.1 Ga.

References

Albarède, F., 1995. Introduction to Geochemical Modeling. Cambrigde University Press, New York, 543 pp.

Albarède, F., Beard, B.L., 2004. Analytical methods for non-traditional isotopes, in: Johnson, C.M., Beard, B.L., Albarède, F. (Eds.), Geochemistry of Non-Traditional Stable Isotopes. Reviews in Mineralogy and Geochemistry, Mineralogical Society of America, Washington, D.C., 55, pp. 113-152.

Albarède, F., Telouk, P., Blichert-Toft, A., Boyet, M., Agranier, A., Nelson, B., 2004. Precise and accurate isotopic measurements using multiple-collector ICPMS. Geochim. Cosmochim. Acta 68, 2725-2744.

Alleman, L.Y., Cardinal, D., Cocquyt, C., Plisnier, P.D., Descy, J.-P., Kimirei, I., Sinyianza, D., André, L., 2005. Silicon isotopic fractionation in Lake Tanganyika and its tributaries. Journal of Great Lakes Research 31, 509-519.

Allenby, R.J., 1954. Determination of the isotopic ratios of silicon in rocks. Geochim. Cosmochim. Acta 5, 40-48.

André, L., Cardinal, D., Alleman, L.Y., Moorbath S., 2006. Silicon isotopes in ~3.8 Ga West Greenland rocks as clues to the Eoarchean supracrustal Si cycle. Earth Planet. Sci. Lett. 245, 162-173.

Anhaeusser, C.R., 1976. The geology of the Sheba Hills area of the Barberton Mountain Land, South Africa, with particular reference to the Eureka Syncline. Trans. Geol. Soc. S. Afr. 79, 253-280.

Anhaeusser, C.R., 1983. The geology of the Schapenburg greenstone remnant and surrounding Archaean granitic terrane south of Badplaas, eastern Transvaal. Spec. Publ. Geol. Soc. S. Afr. 9, 31-44.

Anhaeusser, C.R., 2006. A re-evaluation of Archean intracratonic terrane boundaries on the Kaapvaal Craton, South Africa: Collisional suture zones? in: Reimold, W.U., Gibson, R.L. (Eds.), Processes on the Earth. Spec. Pap. Geol. Soc. Am. 405, pp. 193-210.

Armstrong, R.A., Compston, W., de Wit, M.J., Williams, I.S., 1990. The stratigraphy of the 3.5–3.2 Ga Barberton Greenstone Belt revisited: a single zircon ion microprobe study Earth Planet. Sci. Lett. 101, 90-106.

Arndt, N.T., Coltice, N., Helmstaedt, H., Gregoire, M., 2009. Origin of Archean subcontinental lithospheric mantle: Some petrological constraints. Lithos 109, 61-71.

Awramik, S.M., Schopf, J.W., Walter, M.R., 1983. Filamentous fossil bacteria from the Archean of Western Australia. Precambrian Res. 20, 357-374.

Barghoorn, E.S., Tyler, S.A., 1965. Microorganisms of middle Precambrian age from the Animikie series. Current aspects of exobiology, Ontario, Canada, 3, 93-118.

Barker, F., 1979. Trondhjemites: definition, environment and hypotheses of origin, in: Barker, F. (Ed.), Trondhjemites, Dacites and Related Rocks. Elsevier, Amsterdam, pp. 1-12.

Baroni, S., Gironcoli, S., Dal Corso, A., Giannozzi, P., 2001. Phonons and related crystal properties from density-functional perturbation theory. Rev. Mod. Phys. 73, 515-562.

Basile-Doelsch, I., 2006. Si stable isotopes in the Earth‘s surface: A review. J. Geochem. Expl. 88, 252-256.

Basile-Doelsch, I., Meunier, J.D., Parron, C., 2005. Another continental pool in the terrestrial silicon cycle. Nature 433, 399-402.

Bau, M., Möller, P., 1993. Rare earth element systematics of the chemically precipitated component in early Precambrian iron formations and the evolution of the terrestrial atmosphere-hydrosphere-lithosphere system. Geochim. Cosmochim. Acta 57, 2239-2249.

Beaty, D.W., Taylor, H.P., 1982. Some petrologic and oxygen isotopic relationships in the Amulet Mine, Noranda, Quebec, and their bearing on the origin of Archean massive sulfide deposits. Jr. Econ. Geol. 77, 95-108.

Belshaw, N.S., Freedman, P.A., O´Nions, R.K., Frank, M., Guo, Y., 1998. A new variable dispersion double-focusing plasma mass spectrometer with performance illustrated for Pb isotopes. Int. J. Mass Spectrom. 181, 51-58.

Berner, R.A., 1997. Paleoclimate - The rise of plants and their effect on weathering and atmospheric CO_2. Science 276, 544-546.

Bohrmann, G., Abelmann, A., Gersonde, R., Hubberten, H., Kuhn, G., 1994. Pure siliceous ooze, a diagenetic environment for early chert formation. Geology 22, 207-210.

Bolhar, R., Kamber, B.S., Moorbath, S., Fedo, C.M., Whitehouse M.J., 2004. Characterisation of early Archaean chemical sediments by trace element signatures, Earth Planet. Sci. Lett. 222, 43-60.

Brandl, G., Cloete, M., Anhaeusser, C.R., 2006. Archean greenstone belts, in: Johnson, M.R., Anhaeusser, C.R., Thomas, R.J. (Eds.), The Geology of South Africa. Geological Society of South Africa, Johannesburg/Council for Geoscience, Pretoria, pp. 9-56.

Brzezinski, M.A., Jones, J.L., Beucher, C.P., Demarest, M.S., Berg, H.L., 2006. Automated determination of silicon isotope natural abundance by the acid decomposition of cesium hexafluosilicate. Anal. Chem. 78, 6109-6114.

Buick, R., Dunlop, J.S.R., 1990. Evaporitic sediments of Early Archean age from the Warrawoona Group, North-Pole, Western-Australia. Sedimentology 37, 247-277.

Byerly, G.R., Kröner, A., Lowe, D.R., Todt, W., Walsh, M.M., 1996. Prolonged magmatism and time constraints for sediment deposition in the early Archaean Barberton Greenstone belt: evidence from the Upper Onverwacht and Fig Tree Groups. Precambrian Res. 78, 125-138.

Cardinal, D., Alleman, L.Y., de Jong, J., Ziegler, K., André, L., 2003. Isotopic composition of silicon measured by multicollector plasma source mass spectrometry in dry plasma mode. J. Anal. Atom. Spectrom. 18, 213-218.

Cardinal, D., Alleman, L.Y., Dehairs, F., Savoye, N., Trull, T.W., André, L., 2005. Relevance of silicon isotopes to Si-nutrient utilization and Si-source assessment in Antarctic waters. Glob. Biochem. Cycl. 19. doi:10,1029/2004GB002364.

Cardinal, D., Savoye, N., Trull, T.W., Dehairs, F., Kopczynska, E.E., Fripiat, F., Tison, J.-L., André, L., 2007. Silicon isotopes in spring Southern Ocean diatoms: large zonal changes despite homogeneity among size fractions. Marine Chemistry 106, 46-62.

Carignan, J., Cardinal, D., Eisenhauer, A., Galy, A., Rehkämper, M., Wombacher, F., Vigier, N., 2004. A reflection on Mg, Cd, Ca, Li and Si isotopic measurements and related reference materials. Geostand. Geoanal. Res. 28, 139-148.

Chmeleff, J., Horn, I., Steinhoefel, G., von Blanckenburg, F., 2008. In situ determination of precise stable Si isotope ratios by UV-femtosecond laser ablation high-resolution multi- collector ICP-MS. Chem. Geol. 249, 155-166.

Clayton, R.N., Mayeda, T.K., 1963. The use of bromine pentauoride in the extraction of oxygen from oxides and silicates for isotopic analysis. Geochim. Cosmochim. Acta 27, 43-52.

Clayton, R.N., Grossmann, L., Mayeda, T.K., 1973. A component of primitive nuclear composition in carbonaceous chondrites. Science 182, 485-488.

Clayton, R.N., Mayeda, T.K., Hurd, J.M., 1974. Loss of oxygen, silicon, sulfur and potassium from the lunar regolith. Proc. Fifth Lunar Sci. Conf. 1801-1809.

Cloete, M., 1999. Aspects of volcanism and metamorphism of the Onverwacht Group lavas in the southwestern portion of the Barberton Greenstone Belt. Mem. Geological Survey of South Africa 84, 232 pp.

Compston, W., Kröner, A., 1988. Multiple zircon growth within early Archean Tonalitic gneiss from the Ancient Gneiss Complex, Swaziland. Earth Planet. Sci. Lett. 87, 13-28.

Condie, K.C., 1981. Archaean Greenstone Belts, Elsevier, Amsterdam, 434 pp.

Coplen, T.B., Kendall, C., Hopple, J., 1983. Comparison of stable isotope reference samples. Nature 302, 236-238.

De Freitas, A.S.W., McCulloch, A.W., McInnes, A.G., 1991. Recovery of silica from aqueous silicate solutions via trialkyl or tetraalkylammonium silicomolybdate. Canadian Journal of Chemistry 69, 611-614.

De La Rocha, C.L., 2002. Measurement of silicon stable isotope natural abundances via multicollector inductively coupled plasma mass spectrometry (MC-ICP-MS). Geochemistry, Geophysics, Geosystems, 3(8), 10.1029/2002GC000310.

De La Rocha, C.L., 2003. Silicon isotope fractionation by marine sponges and the reconstruction of the silicon isotope composition of ancient deep water. Geology 31, 423-426.

De La Rocha, C.L., Brzezinski, M.A., DeNiro, M.J., 1996. Purification, Recovery, and Laser-Driven Fluorination of Silicon from Dissolved and Particulate Silica for the Measurement of Natural Stable Isotope Abundances. Anal. Chem. 68, 3746-3750.

De La Rocha, C.L., Brzezinski, M.A., DeNiro, M.J., 1997. Fractionation of silicon isotopes by marine diatoms during biogenic silica formation. Geochim. Cosmochim. Acta 61, 5051-5056.

De La Rocha, C.L., Brzezinski, M.A., DeNiro, M.J., Shemesh, A., 1998. Silicon isotope composition of diatoms as an indicator of past oceanic change. Nature 395, 680-683.

De La Rocha, C.L., Brzezinski, M.A., DeNiro, M.J., 2000. A first look at the distribution of stable isotopes of silicon in natural waters. Geochim. Cosmochim. Acta 64, 2467-2477.

De La Rocha, C.L., Bickle, M.J., 2005. Sensitivity of silicon isotopes to whole-ocean changes in the silica cycle. Marine Geology 217, 267-282.

Delstanche, S., Opfergelt, S., Cardinal, D., Elsass, F., Andre, L., Delvaux, B., 2009. Silicon isotopic fractionation during adsorption of aqueous monosilicic acid onto iron oxide. Geochim. Cosmochim. Acta 73, 923-934.

Demarest, M.S., Brzezinski, M.A., Beucher, C.P., 2009. Fractionation of silicon isotopes during biogenic silica dissolution. Geochim. Cosmochim. Acta 73, 5572-5583.

de Ronde, C.E.J., de Wit, M.J., 1994. Tectonic history of the Barberton greenstone belt, South Africa: 490 million years of Archean crustal evolution. Tectonics 13, 983-1005.

de Ronde, C.E.J., Kamo, S.L., 2000. An Archaean Arc-Arc collisional event: a short-lived (ca. 3 Myr) episode, Weltevreden area, Barberton greenstone belt, South Africa. Journal of African Earth Sciences 30, 219-248.

De Vries, S.T., 2004. Early Archaean sedimentary basins: depositional environment and hydrothermal systems. Geologica Ultraiectina 244, 1-160.

de Wit, M.J., 1991. Archaean greenstone belt tectonism and basin development: some insights from the Barberton and Pietersburg greenstone belts, Kaapvaal Craton, South Africa. Journal of African Earth Sciences 13, 45-63.

de Wit, M.J., 1998. On Archean granites, greenstones, cratons and tectonics: does the evidence demand a verdict? Precambrian Res. 91, 181-226.

de Wit, M.J., Fripp, R.E.P., Stanistreet, I.G., 1983. Tectonic and stratigraphic implications of new field observations along the southern part of the Barberton greenstone belt. Spec. Publ. Geol. Soc. S. Afr. 9, 21-30.

de Wit, M.J., Hart, R.J., Wilson, A.H., 1987. Felsic igneous rocks within the 3.3.–3.5 Ga Barberton greenstone belt: high crustal level equivalents to the surrounding tonalite–trondhjemite terrane, emplaced during thrusting. Tectonics 6, 529-549.

de Wit, M.J., Roering, C., Hart, R.J., Armstrong, R.A., de Ronde, C.E.J., Green, R.W.E., Tredoux, M., Peberdy, E., Hart, R.A., 1992. Formation of an Archaean continent. Nature 357, 553-562.

Diener, J.F.A., Stevens, G., Kisters, A.F.M., Poujol, M., 2005. Metamorphism and exhumation of the basal parts of the Barberton greenstone belt, South Africa: Constraining the rates of Mesoarchaean tectonism. Precambrian Res. 143, 87-122.

DiMarco, M.J., Lowe, D.R., 1989a. Shallow-water volcaniclastic deposition in the Early Archean Panorama Formation, Warrawoona Group, eastern Pilbara Block, Western Australia. Sedimentary Geology 64, 43-63.

DiMarco, M.J., Lowe, D.R., 1989b. Stratigraphy and sedimentology of an Early Archean felsic volcanic sequence, eastern Pilbara Block, Western Austraila, with special reference to the Duffer Formation and implications for crustal evolution. Precambrian Res. 44, 147-169.

Ding, T., Jiang, S., Wan, D., Li, Y., Li, J., Song, H., Liu, Z., Yao, X., 1996. Silicon isotope geochemistry. Geological Publishing House, Beijing, China, 125 pp.

Ding, T., Wan, D., Wang, C., Zhang, F., 2004. Silicon isotope compositions of dissolved silicon and suspended matter in the Yangtze River, China. Geochim. Chosmochim. Acta 68, 205-216.

Ding, T., Wan, D., Bai, R., Zhang, Z., Shen, Y., Meng, R., 2005a. Silicon isotope abundance ratios and atomic weights of NBS-28 and other reference materials. Geochim. Chosmochim. Acta 69, 5487-5494.

Ding, T.P., Ma, G.R., Shui, M.X., Wan, D.F., and Li, R.H., 2005b. Silicon isotope study on rice plants from the Zhejiang province, China. Chem. Geol. 218, 41-50.

Douthitt, C.B., 1982. The geochemistry of stable isotopes of silicon. Geochim. Cosmochim. Acta 46, 1449-1458.

Duchac, K.C., Hanor, J.S., 1987. Origin and timing of metasomatic silicification of an early Archean komatiite sequence, Barberton Mountain Land, South Africa. Precambrian Res. 37, 125-146.

Dziggel, A., Stevens, G., Poujol, M., Anhaeusser, C.R., Armstrong, R.A., 2002. Metamorphism of the granite-greenstone terrane south of the Barberton greenstone belt, South Africa: an insight into the tectono-thermal evolution of the 'lower' portions of the Onverwacht Group. Precambrian Res. 114, 221–247.

Engström, E., Rodushkin, I., Baxter, D.C., Ohlander, B., 2006. Chromatographic purification for the determination of dissolved silicon isotopic compositions in natural waters by high-resolution multicollector inductively coupled plasma mass spectrometry. Anal. Chem. 78, 250-257.

Engström, E., Rodushkin, I., Baxter, D.C., Ingri, J., Ohlander, B., 2007. Characterization of the silicon isotopic composition of the terrestrial biogenic output from a boreal forest in Northern Sweden. Geochim. Cosmochim. Acta 71, A256.

Epstein, S., Taylor, H.P.J., 1970. Stable isotopes, rare gases, solar wind, and spallation products. $^{18}O/^{16}O$, $^{30}Si/^{28}Si$, D/H, $^{13}C/^{12}C$ studies of lunar rocks and minerals. Science 167, 533-535.

Farmer, J.D., Des Marais, D.J., 1999. Exploring for a record of ancient Martian life. J. Geophys. Res. 104, 26977-26995.

Faure, F., Mensing, T.M., 2005. Isotopes: Principles and Applications, John Wiley and Sons, New York, 897 pp.

Fitoussi, C., Bourdon, B., Kleine, T., Oberli, F., Reynolds, B.C., 2009. Si isotope systematics of meteorites and terrestrial peridotites: implications for Mg/Si fractionation in the solar nebula and for Si in the Earth's core. Earth Planet. Sci. Lett. 287, 77-85.

Flanagan, F.J., Wright, T.L., Taylor, S.R., Annell, C.S., Christian, R.C., Dinnin J.I., 1976. Basalt, BHVO-1, from Kilauea crater, Hawaii. U.S. Geological Survey Professional Paper 840, 33-39.

Foley, S., Tiepolo, M., Vannucci, R., 2002. Growth of early continental crust controlled by melting of amphibolite in subduction zones, Nature 417, 637-640.

Foley, S.F., Buhre, S.(♥), Jacob, D.E., 2003. Evolution of the Archean crust by shallow subduction and recycling, Nature 421, 249-252.

Folk, R.L., 1980. Petrology of Sedimentary Rocks, Hemphill Publishing Company, Austin, 185 pp.

Fripiat, F., Cardinal, D., Tison, J-L, Worby, A., André L., 2007. Diatom-induced silicon isotopic fractionation in Antarctic sea ice. J. Geophys. Res. 112, G02001, doi:10.1029/2006JG000244.

Galy, A., Belshaw, N.S., Halicz, L., O'Nions, R.K., 2001. High-precision measurement of magnesium isotopes by multiple-collector inductively coupled plasma mass spectrometry. Int. J. Mass Spectrom. 208, 89-98.

Garlick, G.D., Epstein, S., 1967. Oxygen isotope ratios in coexisting minerals of regionally metamorphosed rocks. Geochim. Cosmochim. Acta 31, 181-214.

Georg, R.B., Reynolds, B.C., Halliday, A.N., Zhu, C., 2005. Fractionation of stable Si isotopes during in-situ dissolution of feldspars and formation of secondary clay minerals. EOS Trans AGU Fall Meet. Suppl. 86 (52), Abstract.

Georg, R.B., Reynolds, B.C., Frank, M., Halliday, A.N., 2006a. New sample preparation techniques for the determination of Si isotopic compositions using MC-ICPMS. Chem. Geol. 235, 95-104.

Georg, R.B., Reynolds, B.C., Frank, M., Halliday, A.N., 2006b. Mechanisms controlling the silicon isotopic composition of river waters. Earth Planet. Sci. Lett. 249, 290-306.

Georg, R.B., Halliday, A.N., Schauble, E.A., Reynolds, B.C., 2007a. Silicon in the Earth's core. Nature 447, 1102-1106.

Georg, R.B., Reynolds, B.C., West, A.J., Burton, K.W., Halliday, A.N., 2007b. Silicon isotope variations accompanying basalt weathering in Iceland. Earth Planet. Sci. Lett. 261, 476-490.

Georg, R.B., Basu, A.R., West, A.J., Halliday, A.N., 2007c. Continent ocean fluxes and isotopic compositions of dissolved silicon contributed by groundwater. EOS Trans AGU Fall Meet. Suppl. 88 (52), Abstract.

Georg, R.B., Zhu, B., Reynolds, B.C., Halliday, A.N., 2009a. Stable silicon isotopes of groundwater, feldspars, and clay coatings in the Navajo Sandstone aquifer, Black Mesa, Arizona, USA. Geochim. Cosmochim. Acta 73, 2229-2241.

Georg, R.B., West, A.J., Basu, A.R., Halliday, A.N., 2009b. Silicon fluxes and isotope composition of direct groundwater discharge into the Bay of Bengal and the effect on the global ocean silicon isotope budget, Earth Planet. Sci. Lett. 283, 67-74.

Giletti, B.J., 1986. Diffusion effects on oxygen isotope temperatures of slowly cooled igneous and metamorphic rocks. Earth Planet. Sci. Lett. 77, 218-228.

Glikson, M., Duck, L.J., Golding, S., Hofmann, A., Bolhar, R., Webb, R., Baiano, J., Sly, L., 2008. Microbial remains in some earliest Earth rocks: comparison with a potential modern analogue. Precambrian Res. 164, 187-200.

Gonze, X., Beuken, J.-M., Caracas, R., Detraux, F., Fuchs, M., Rignanese, G.-M., Sindic, L., Verstraete, M., Zerah, G., Jollet, F., Torrent, M., Roy, A., Mikami, M., Ghosez, P., Raty, J.-Y., Allan, D. 2002. First-principles computation of material properties: the ABINIT software project. Comput. Mater. Sci. 25, 478-492.

Grant, F.S., 1954. The geological significance of variations in the abundances of the isotopes of silicon in rocks, Geochim. Cosmochim. Acta 5, 225-242.

Gregory, R.T., Taylor, H.P., 1981. An oxygen isotope profile in a section of Cretaceous oceanic crust, Samail ophiolite, Oman: evidence for $\delta^{18}O$ buffering of the oceans by deep (N5 km) seawater-hydrothermal circulation at mid-ocean ridges. J. Geophys. Res. 86, 2737-2755.

Gunnarsson, I., Arnórsson, S., 2000. Amorphous silica solubility and the thermodynamic properties of H4SiO°4 in the range of 0° to 350 °C at Psat, Geochim. Cosmochim. Acta 64, 2295-2307.

Hall, A.L., 1918. The Geology of the Barberton Gold Mining District, Geological Survey of South Africa, Memoir 9, 347 pp.

Hanor, J.S., Duchac, K.C., 1990. Isovolumetric silicification of early Archean komatiites: geochemical mass balances and constraints on origin. J. Geol. 98, 863-877.

Harris, C., Smith, S., le Roex, A.P., 2000. Oxygen isotope composition of phenocrysts from Tristan da Cunha Gough Island lavas: variation with fractional crystallisation and evidence for assimilation. Contrib. Mineral. Petrol. 138, 164-175.

Hart, S.R., Zindler, A., 1989. Isotope fractionation laws: A test using calcium. International Journal of Mass Spectrometry and Ion process 89, 287-301.

Hattori, I., Umeda, M., Nakagawa, T., Yamamoto, H, 1996. From chalcedonic chert to quartz chert: diagenesis of chert hosted in a Miocene volcanicsedimentary succession, central Japan. Journal of Sedimentary Research 66, 163-174.

Hesse, R., 1989. Silica Diagenesis: Origin of Inorganic and Replacement Cherts. Earth-Science Reviews 26, 253-284.

Heubeck, C., Lowe, D.R., 1994. Late syndepositional deformation and detachment tectonics in the Barberton greenstone belt, South Africa. Tectonics 13, 1514-1536.

Heubeck, C., Lowe, D.R., 1999. Sedimentary petrography and provenance of the Archean Moodies Group, Barberton greenstone belt, in: Lowe, D.R., Byerly, G.R. (Eds.), Geologic Evolution of the Barberton Greenstone Belt, South Africa. Spec. Pap. Geol. Soc. Am. 329, pp. 259-286.

Hoefs, J., 1997. Stable Isotope Geochemistry. Springer-Verlag, Berlin, 201 pp.

Hoffman, S.E., Wilson, M., Stakes, D.S., 1986. Inferred oxygen isotope profile of Archaean oceanic crust, Onverwacht Group, South Africa. Nature 321, 55-58.

Hofmann, A., 2005. The geochemistry of sedimentary rocks from the Fig Tree Group, Barberton greenstone belt: implications for tectonic, hydrothermal and surface processes during mid-Archaean times. Precambrian Res. 143, 23-49.

Hofmann, A., Bolhar, R., 2007. The origin of carbonaceous cherts in the Barberton greenstone belt and their significance for the study of early life in mid-Archaean rocks. Astrobiology 7, 355-388.

Hofmann, A., Wilson, A.H., 2007. Silicified basalts, bedded cherts and other sea floor alteration phenomena of the 3.4 Ga Nondweni greenstone belt, South Africa, in: Van Kranendonk, M.J., Smithies, R.H., Bennett, V. (Eds.), Earth's Oldest Rocks. Developments in Precambrian Geology 15, pp. 571-605.

Hofmann, A., Harris, C., 2008. Silica alteration zones in the Barberton greenstone belt: A window into subseafloor processes 3.5-3.3 Ga ago. Chem. Geol. 257, 221-239.

House, C.H., Schopf, J.W., McKeegan, K.D., Coath, C.D., Harrison, T.M., Stetter, K.O., 2000. Carbon isotopic composition of individual Precambrian microfossils. Geology 28, 707-710.

Huneke, J.C., Armstrong, J.T., Wasserburg, G.J., 1983. Fun with Panurge: High mass resolution ion microprobe measurements of Mg in Allende inclusions. Geochim. Cosmochim. Acta 47, 1635-1650.

Hunter, D.R., 1974. Crustal development in Kaapvaal craton, I. The Archaean. Precambrian Res. 1, 259-294.

Jochum, K.P., Nohl, U., Herwig, K., Lammel, E., Stoll, B., Hofmann, A.W., 2005 GeoReM: a new geochemical database for reference materials and standards (http://georem.mpch-mainz.gwdg.de/). Geostand Geoanal. Res. 29, 333-338.

Johnson, C.M., Beard, B.L., Albaréde, F., 2004. Geochemistry of Non-Traditional Stable Isotopes, Reviews in Mineralogy and Geochemistry, Mineralogical Society of America, Washington, D.C., 55, 454 pp.

Kamo, S.L., Davis, D.W., 1994. Reassessment of Archean crustal development in the Barberton Mountain Land, South Africa, based on U-Pb dating, Tectonics 13, 167-192.

Kasting, J.F., Howard, M.T., Wallmann, K., Veizer, J., Shields, G., Jaffrés, J., 2006. Paleoclimates, ocean depth, and the oxygen isotopic composition of seawater. Earth Planet. Sci. Lett. 252, 82-93.

Kastner, M., Keene, J.B., Gieskes, J.M., 1977. Diagenesis of siliceous oozes: 1. Chemical controls on the rate of opal-A to opal-CT transformation—an experimental study. Geochim. Cosmochim. Acta 41, 1041-1059.

Kato, Y., Nakamura, K., 2003. Origin and global tectonic significance of Early Archean cherts from the Marble Bar greestone belt, Pilbara Craton, Western Australia. Precambrian Res. 125, 191-243.

Kent, R.W., Hardarson, B.S., Saunders, A.D., Storey, M., 1996. Plateaux ancient and modern: geochemical and sedimentological perspectives on Archean oceanic magmatism. Lithos 37, 129-142.

Kisters, A.F.M., Anhaeusser, C.R., 1995. Emplacement features of Archaean TTG plutons along the southern margin of the Barberton greenstone belt, South Africa. Precambrian Res. 75, 1-15.

Kisters, A.F.M., Stevens, G., Dziggel, A., Armstrong, R.A., 2003. Extensional detachment faulting and core complex formation in the southern Barberton granite-greenstone terrain, South Africa: evidence for a 3.2 Ga orogenic collapse. Precambrian Res. 127, 355-378.

Kisters A.F.M., Belcher, R., Poujol, M., Stevens, G., Moyen, J.F., 2006. A 3.2 Ga magmatic arc preserving 50 Ma of crustal convergence in the Barberton terrain, South Africa. EOS tras. AGU Fall Meet. Suppl. 87, (52), Abstract.

Kitajima, K., Maruyama, S., Utsunomiya, S., Liou, J.G., 2001. Seafloor hydrothermal alteration at an Archaean mid-ocean ridge. Journal of Metamorphic Geology 19, 581-597.

Knauth, L.P., 1979. A model for the origin of chert in limestone. Geology 7, 274-277.

Knauth, L.P., 1994. Petrogenesis of chert, in: Heaney, P.J., Prewitt, C.T., Gibbs, G.V. (Eds.), Silica: Physical Behavior, Geochemistry and Materials Applications. Reviews in Mineralogy, Mineralogical Society of America, Washington, D.C., 29, pp. 233-258.

Knauth, L.P., 2005. Temperature and salinity history of the Precambrian ocean: implications for the course of microbial evolution. Palaeogeogr. Palaeoclimatol. Palaeoecol. 219, 53-69.

Knauth, L.P., Lowe, D.R., 1978. Oxygen isotope geochemistry of cherts from the Onverwacht Group (3.4 billion years), Transvaal, South Africa, with implications for secular variations in the isotopic composition of cherts. Earth Planet. Sci. Lett. 41, 209-222.

Knauth, L.P., Lowe, D.R., 2003. High Archean climatic temperature inferred from oxygen isotope geochemistry of cherts on the 3.5 Ga Swaziland Supergroup, South Africa. GSA Bull. 115, 566-580.

Konhauser, K.O., Amskold, L., Lalonde, S.V., Posth, N.R., Kappler, A. Anbar, A., 2007. Decoupling photochemical Fe(II) oxidation from shallow-water BIF deposition. Earth Planet. Sci. Lett. 258, 87-100.

Kröner, A., Todt, W., 1988. Single zircon dating constraining the maximum age of the Barberton greenstone belt, southern Africa. J. Geophys. Res. 93, 329-337.

Kröner, A., Compston, W., Williams, I.S., 1989. Growth of early Archaean crust in the Ancient Gneiss Complex of Swaziland as revealed by single zircon dating. Tectonophysics 161, 271-298.

Kröner, A. Hegner, E., Byerly, G.R., Lowe, D.R., 1992. Possible terrane identification in the early Archaean Barberton greenstone belt, South Africa, using single zircon geochronology. EOS Trans. AGU Fall Meet. Suppl. 73 (616), Abtract.

Kröner, A., Hegner, E., Wendt, J.I., Byerly, G.R., 1996. The oldest part of the Barberton granitoid-greenstone terrain, South Africa: evidence for crust formation between 3.5 and 3.7 Ga. Precambrian Res. 78, 105-124.

Lecuyer, C., Gruau, G., Anhaeusser, C.R., Fourcade, S., 1994. The origin of fluids and the effects of metamorphism on the primary chemical compositions of Barberton komatiites: New evidence from geochemical (REE) and isotopic (Nd, O, H, $^{39}Ar,/^{40}Ar$) data. Geochim. Cosmochim. Acta 58, 969-984.

Lowe, D.R., 1994. Accretionary history of the Archean Barberton Greenstone Belt (3.55–3.22 Ga), southern Africa. Geology 22, 1099-1102.

Lowe, D.R., 1999. Petrology and sedimentology of cherts and related silicified sedimentary rocks in the Swaziland Supergroup, in: Lowe, D.R., Byerly, G.R. (Eds.), Geologic Evolution of the Barberton Greenstone Belt, South Africa. Spec. Pap. Geol. Soc. Am. 329, pp. 83-114.

Lowe, D.R., Byerly, G.R., 1986. Archean flow-top alteration zones formed initially in a low-temperature sulphate-rich environment. Nature 324, 245-248.

Lowe, D.R., Byerly, G.R., 1999. Stratigraphy of the west-central part of the Barberton Greenstone Belt, South Africa, in: Lowe, D.R., Byerly, G.R. (Eds.), Geologic Evolution of the Barberton Greenstone Belt, South Africa. Spec. Pap. Geol. Soc. Am. 329, pp. 1-36.

Lowe, D.R., Fisher-Worrell, G., 1999. Sedimentology, mineralogy, and implications of silicified evaporites in the Kromberg Formation, Barberton Greenstone Belt, South Africa, in: Lowe, D.R., Byerly, G.R. (Eds.), Geologic Evolution of the Barberton Greenstone Belt, South Africa. Spec. Pap. Geol. Soc. Am. 329, pp. 167-188.

Lowe, D.R., Byerly, G.R., 2007. An overview of the geology of the Barberton greenstone belt and vicinity: implications for early crustal development. In: Van Kranendonk, M.J., Smithies, R.H., Bennett, V.C. (Eds.), Earth's Oldest Rocks. Developments in Precambrian Geology, vol. 15. Elsevier, Amsterdam, pp. 481-526.

Loughheed, M.S., 1983. Origin of Precambrian iron formation in the Lake Superior region. GSA Bull. 94, 325-340.

Lugaro, M., Zinner, E., Gallino, R. Amari, S., 1999. Si isotopic ratios in mainstream presolar SiC grains revisited. Astrophysical Journal 527, 369-394.

Mackenzie, F.T., Gees, R., 1971. Quartz: synthesis at Earthsurface conditions. Science 173, 533-535.

Maliva, R.G., Knoll, A.H., Simonson, B.M., 2005. Secular change in the Precambrian silica cycle: Insights from chert petrology. Geological Society of America Bulletin 117, 835-845.

Martin, H., 1986. Effect of steeper Archean geothermal gradient on geochemistry of subduction-zone magma. Geology 14, 753-756.

Martin, H., 1993. The mechanisms of petrogenesis of the Archaean continental crust-comparison with modern processes. Lithos 30, 373-388.

Matsuhisa, Y., Goldsmith, J.R., Clayton, R.N., 1979. Oxygen isotopic fractionation in the system quartz-albite-anorthite-water. Geochim. Cosmochim. Acta 43, 1131-1140.

Mattey, D., Lowry, D., Macpherson, C., 1994. Oxygen isotope composition of mantle peridotite. Earth Planet. Sci. Lett. 128, 231-241.

Méheut, M., Lazzeri, M., Balan, E., Mauri, F., 2007. Equilibrium isotopic fractionation in the kaolinite, quartz, water system: Prediction from first-principles density-functional theory. Geochim. Cosmochim. Acta 71, 3170-3181.

Méheut, M., Lazzeri, M., Balan, E., Mauri, F., 2009. Structural control over equilibrium silicon and oxygen isotopic fractionation: A first-principles density-functional theory study. Chem. Geol. 258, 28-37.

Melander, L., Saunders, W.H., 1980. Reaction Rates of Isotopic Molecules, John Wiley and Sons, New York, 144 pp.

Molini-Velsko, C., Mayeda, T.K., Clayton, R.N., 1986. Isotopic composition of silicon in meteorites. Geochim. Cosmochim. Acta 50, 2719-2726.

Montaser, A., McLean, J.A., Liu, H., Mermet, J.-M., 1998. An introduction to ICP spectrometries for elemental analysis, in: Montaser, A. (Ed.), Inductively Coupled Plasma Mass Spectrometry. Wiley-VCH, New York, pp. 1-31.

Morris, R.C., 1993. Genetic modelling for banded iron-formation of the Hamersley Group, Pilbara Craton, Western Australia. Precambrian Res. 60, 243-286.

Moyen, J.F., Stevens, G., Kisters, A.F.M., Belcher, R.W., 2007. TTG plutons of the Barberton Granitoid-Greenstone Terrain, South Africa, in: Van Kranendonk M.J., Smithies R.H., Bennett V.C. (Eds.), Earth´s Oldest Rocks, Developments in Precambrian Geology, 15, pp. 607-667, Elsevier, Amsterdam.

Muehlenbachs, K., Clayton, R.N., 1972. Oxygen isotope studies of fresh and weathered submarine basalts. Can. J. Earth Sci. 9, 172-184

Muehlenbachs, K, 2009. Temperature gradients in the marine Archean exogenic cycle derived from the alteration of seafloor basalts, Barberton Greenstone Belt, South Africa. Geological Society of America Abstracts with Programs, Vol. 41, No. 7, p. 529.

Nehring, F., Jacob, D.E., Barth, M.G., Foley, S.F., 2008. Laser-ablation ICP-MS analysis of siliceous rock glasses fused on an iridium strip heater using MgO dilution. Microchim. Acta 160, 153-163.

Nehring, F., Foley, S.F., Hölttä, P., Van den Kerkhof, A.M., 2009. Internal differentiation of the Archean continental crust: fluid-controlled partial melting of granulites and TTG-amphibolite associations in Central Finland, Journal of Petrology 50, 3-35.

Nijman, W., de Bruijne, K.C.H., Valkering, M.E., 1999. Growth fault control of Early Archaean cherts, barite mounds and chert-barite veins, North Pole Dome, Eastern Pilbara, Western Australia. Precambrian Res. 95, 247-274.

O‘Connor, J.T., 1965. A classification for quartz-rich igneous rocks based on feldspar ratios. U.S. Geol. Surv. Prof. Pap., 525-B, 79-84.

Oliver, N.H.S., Cawood, P.A., 2001. Early tectonic dewatering and brecciation on the overturned sequence at Marble Bar, Pilbara Craton, Western Australia: dome-related or not? Precambrian Res. 105, 1-15.

O´Neil, J.R., 1986. Theoretical and experimental aspects of isotope fractionation, in: Valley, J.W., Taylor, H.P., O´Neil, J.R. (Eds.), Stable Isotope in High Temperature Geological Processes. Reviews in Mineralogy, Mineralogical Society of America, Washington, D.C., 16, pp. 1-40.

Opfergelt, S., Cardinal, D., Henriet, C., André, L., Delvaux, B., 2006a. Silicon isotopic fractionation by banana (*Musa* spp.) grown in a continuous nutrient flow device. Plant and Soil 285, 333-345.

Opfergelt, S., Cardinal, D., Henriet, C., André, L., Delvaux, B., 2006b. Silicon isotope fractionation between plant parts in banana: In situ vs. in vitro. J. Geochem. Expl. 88, 224-227.

Opfergelt, S., Delvaux, B., André, L., Cardinal, D., 2008. Plant silicon isotopic signature might reflect soil weathering degree. Biogeochemistry 91, 163-175.

Opfergelt, S., de Bournonville, G., Cardinal, D., André, L., Delstanche, S., Delvaux, B., 2009. Impact of soil weathering degree on silicon isotopic fractionation during adsorption onto iron oxides in basaltic ash soils, Cameroon. Geochim. Cosmochim. Acta 73, 7226-7240.

Opfergelt, S., Cardinal, D., André, L., Delvigne, C., Bremond, L., Delvaux, B., 2010. Variations of δ^{30}Si and Ge/Si with weathering and biogenic input in tropical basaltic ash soils under monoculture. Geochim. Cosmochim. Acta 74, 225-240.

Orberger, B., Rouchon, V., Westall, F., de Vries, S.T., Pinti, D.L., Hashizume, K., 2006. Micro-facies and origin of some Archean Cherts (Pilbara, Australia). Spec. Pap. Geol. Soc. Am. 405, pp. 133-156.

Paris, I., Stanistreet, I.G., Hughes, M.J., 1985. Cherts of the Barberton greenstone belt interpreted as products of submarine exhalative activity. J. Geol. 93, 111-129.

Pearce, J.A., Norry, M.J., 1979. Petrogenetic implications of Ti, Zr, Y and Nb variations in the volcanic rocks. Contrib. Mineral. Petrol. 69, 33-47.

Pearton, T.N., 1982. Gold and antimony mineralization in altered komatiites of the Murchison greenstone belt, South Africa, in: Arndt, N.T., Nisbet, E.G. (Eds.), Komatiite, Allen and Unwin, London, pp. 459-475.

Perry, E.C., 1967. The oxygen isotope chemistry of ancient cherts. Earth Planet. Sci. Lett. 3, 62-66.

Perry, E.C., Lefticariu, L., 2003. Formation and geochemistry of Precambrian cherts, in: Holland, H., Turekian, K. (Eds.), Treatise on geochemistry, V. 7, Sediments, diagenesis, and sedimentary rocks, F.T. Mackenzie (Volume ed.), Elsevier, pp. 99-113.

Pinti, D.L., Mineau, R., Clement, V., 2009. Hydrothermal alteration and microfossil artefacts of the 3,465-million-year-old Apex chert. Nature Geoscience 2, 640-643.

Posth, N.R., Hegler, F., Konhauser, K.O., Kappler, A., 2009. Alternating Si and Fe deposition caused by temperature fluctuations in Precambrian oceans. Nature Geoscience 1, 703-708.

Ramsay, J.G., 1963. Structural investigations in the Barberton Mountain Land, eastern Transvaal. Trans. Geol. Soc. S. Afr., 66, 353-401.

Rapp, R., Shimizu, N., Norman, M.D., 2003. Growth of early continental crust by partial melting of eclogite, Nature 425, 605-609.

Reed, N.M., Cairns, R.O., Hutton, R.C., Takaku, Y., 1994. Characterization of Polyatomic Ion Interferences in Inductively Coupled Plasma Mass Spectrometry Using a High Resolution Mass Spectrometer. J. Anal. Atom. Spectrom. 9, 881-896.

Rehkämper, M., Wombacher, F., Aggarwal, J.K., 2004. Stable Isotope Analysis by Multiple Collector ICP-MS, in: de Groot, P.A. (Eds.), Handbook of Stable Isotope Analytical Techniques. Elsevier, Amsterdam, pp. 692-725.

Reynolds, J.H., Verhoogen, J., 1953. Natural variations in the isotopic constitution of silicon. Geochim. Cosmochim. Acta 3, 224-234.

Reynolds, B.C., Frank, M., Halliday, A.N., 2006. Silicon isotope fractionation during nutrient utilization in the North Pacific. Earth Planet. Sci. Lett. 244, 431-443.

Reynolds, B.C., Aggarwal, J., André, L., Baxter, D., Beucher, C., Brzezinski ,M.A., Engström, E., Georg, B., Land, M., Leng, M.J., Opfergelt, S., Rodushkin, I., Sloane, H.J., Van den Boorn, S.H.J.M., Vroon, P.Z., Cardinal, D., 2007. An inter-laboratory comparison of Si isotope reference materials. J. Anal. Atom. Spectrom. 22, 561-568.

Richter, F.M., Watson, E.B., Mendybaev, R, Dauphas, N., Georg B., Watkins, J., Valley, J., 2009. Isotopic fractionation of the major elements of molten basalt by chemical and thermal diffusion. Geochim. Cosmochim. Acta 73, 4250-4263.

Robert, F., 1988. Carbon and oxygen isotope variations in Precambrian cherts. Geochim. Cosmochim. Acta 52, 1473-1478.

Robert, F., Chaussidon, M., 2006. A palaeotemperature curve for the Precambrian oceans based on silicon isotopes in cherts. Nature 443, 969-972.

Rouchon, V., Orberger, B., 2008. Origin and mechanisms of K-Si metasomatism of ca.3.4-3.3 Ga volcaniclastic deposits and implications for Archean seawater evolution: Examples from cherts of Kitty's Gap (Pilbara Craton, Australia) and Msauli (Barberton Greenstone Belt, South Africa). Precambrian Res. 165, 169-189.

Russell, W.A., Papanastassiou, D.A., Tombrello, T.A., 1978. Ca isotope fractionation on the Earth and other solar system materials. Geochim. Cosmochim. Acta 42, 1075-1090.

Savage, P.S, Georg, R.B., Armytage, R.M.G., Williams H.M., Halliday, A.N., 2010. Silicon isotope homogeneity in the mantle. Accepted in Earth Planet. Sci. Lett.

Schauble, E.A., 2004. Applying stable isotope fractionation theory to new systems, in: Non-Traditional Stable Isotopes. Johnson, C.M., Beard, B.L., Albarède, F. (Eds.), Reviews in Mineralogy and Geochemistry, Mineralogical Society of America, Washington, D.C., 55, pp. 65-111.

Schopf, J.W., 1993. Microfossils of the Early Archean Apex Chert: new evidence of the antiquity of life. Science 260, 640-646.

Schopf, J.W., Kudryavtsev, A.B., Agresti, D.G., Wdowiak, T.J., Czaja, A.D., 2002. Laser-Raman imagery of Earth s earliest fossils. Nature 416, 73-76.

Shahar, A., Young, E.D., 2007. Astrophysics of CAI formation as revealed by silicon isotope LA-MC-ICPMS of an igneous CAI. Earth Planet. Sci. Lett. 257, 497-510.

Shields, G.A., Kasting, J.F., 2007. Palaeoclimatology: evidence for hot early oceans? Nature 447, doi:10.1038/nature05830.

Siever, R., 1992. The silica cycle in the Precambrian, Geochim. Cosmochim. Acta 56, 3265-3272.

Simonson, B.M., 1987. Early silica cementation and subsequent diagenesis in arenites from four Early Proterozoic iron formations of North America. J. Sedim. Petrol. 57, 494-511.

Simonson, B.M., Hassler, S.W., 1996. Was the deposition of large Precambrian iron formations linked to major marine transgressions? J. Geol. 104, 665-676.

Smith, H.S., O´Neil, J.R., Erlank, A.J., 1984. Oxygen isotope compositions of minerals and rocks and chemical alteration patterns in pillow lavas from the Barberton greenstone belt, South Africa, in: Kröner, A., (Eds.), Archaean Geochemistry. Springer, pp. 115-137.

Sobolev, A.V., Hofmann, AW., Kuzmin, DV., Yaxley, G.M., Arndt, N.T., Chung, S.L., Danyushevsky, L.V., Elliott, T., Frey, F.A., Garcia, M.O., Gurenko, A.A., Kamenetsky, V.S., Kerr, A.C., Krivolutskaya, N.A., Matvienkov, V.V., Nikogosian, I.K., Rocholl, A., Sigurdsson, I.A., Sushchevskaya, N.M., Teklay, M., 2007. The amount of recycled crust in sources of mantle-derived melts. Science 316, 412-417.

Steinhoefel, G., Horn, I., von Blanckenburg, F., 2009. Micro-scale tracing of Fe and Si isotope signatures in banded iron formation using femtosecond laser ablation. Geochim. Cosmochim. Acta 73, 5343-5360.

Stone, J., Hutcheon, I.D., Epstein, S., Wasserburg, G.J., 1991. Silicon, carbon, and nitrogen isotopic studies of silicon carbide in carbonaceous and enstatite chondrites, in: Taylor, H.P., O´Neil, J.R., Kaplan, I.R., (Eds.), Stable isotope geochemistry. A tribute to Samuel Epstein, Special Pub.3, Geochemical Society. pp. 487-504.

Stumm, W., Wollast, R., 1990. Coordination Chemistry of Weathering: Kinetics of the Surface-Controlled Dissolution of Oxide Minerals, Rev. Geophys., 28, 53-69.

Sugitani, K., Horiuchi, Y., Adachi, M., Sugisaki, R., 1996. Anomalously lowAl_2O_3/TiO_2 values for Archean cherts from the Pilbara block, western Australia—possible evidence for extensive chemical weathering on the early earth. Precambrian Res. 80, 49-76.

Sugitani, K., Yamamoto, K., Adachi, M., Kawabe, I., Sugisaki, R., 1998. Archean cherts derived from chemical, biogenic and clastic sedimentation in a shallow restricted basin: examples from the Gorge Creek Group in the Pilbara Block. Sedimentology 45, 1045-1063.

Sun, S.-S., McDonough, W.F., 1989. Chemical and isotopic systematics of oceanic basalts: implications for mantle compositions and processes, in: Saunders, A.D., Norry, M.J. (Eds.), Magmatism in ocean basins, Geol. Soc. London. Special Publication, 42, pp. 313-345.

Taylor, H.P., Jr., 1978. Oxygen and hydrogen isotope studies of plutonic granitic rocks. Earth Planet. Sci. Lett. 38, 177-210.

Taylor, H.P.J., Epstein, S., 1962. Relationship between $^{18}O/^{16}O$ ratios in coexisting minerals of igneous and metamorphic rocks. Part I: Principles and experimental results. Geological Society of America Bulletin, 73, 461-480.

Taylor, S.R., McLennan, S.M., 1985. The Continental Crust, its Composition and Evolution. Blackwell Scientific Publications, Oxford.

Terabayashi, M., Masada, Y., Ozawa, H., 2003. Archean ocean-floor metamorphism in the North Pole area, Pilbara Craton, Western Australia. Precambrian Res. 127, 167-180.

Tilles, D., 1961. Natural variations in isotopic abundances of silicon. J. Geophys. Res. 66, 3003-3014.

Treguer, P., Nelson, D.M., Van Bennekom, A.J., DeMaster, D.J., Leynaert, A., Queguiner, B., 1995. The silica balance in the world ocean: A reestimate. Science 268, 375-379.

Van den Boorn, S.H.J.M., Vroon, P.Z., van Belle, C.C., van der Wagt, B., Schwieters, J., van Bergen, M.J., 2006. Determination of silicon isotope ratios in silicate materials by high-resolution MC-ICP-MS using a sodium hydroxide sample digestion method. J. Anal. Atom. Spectrom. 734-742.

Van den Boorn, S.H.J.M., Van Bergen, M.J., Nijman, W., Vroon, P.Z., 2007. Dual role of seawater and hydrothermal fluids in Early Archean chert formation: Evidence from silicon isotopes. Geology 35, 939-942.

Van den Boorn, S.H.J.M, van Bergen, M.J., Vroon, P.Z., de Vries, S.T, Nijman, W., 2010. Silicon isotope and trace element constraints on the origin of ~3.5 ga cherts: implications for early Archaean marine environments. Geochim. Cosmochim. Acta 74, 1077-1103.

Vanhaecke, F., Moens, L., 2004. Overcoming spectral overlap in isotopic analysis via single- and muli-collector ICP-mass spectrometry. Anal. Bioanal Chem., 378, 232-240.

Van Kranendonk, M.J., 2006. Volcanic degassing, hydrothermal circulation and the flourishing of early life on Earth: A review of the evidence from c. 3490-3240 Ma rocks of the Pilbara Supergroup, Pilbara Craton, Western Australia. Earth Sci. Rev. 74, 197-240.

Van Kranendonk, M.J., Pirajno, F., 2004. Geological setting and geochemistry of metabasalts and alteration zones associated with hydrothermal chert-barite deposits in the ca. 3.45 Ga Warrawoona Group. Pilbara Craton, Australia. Geochemistry: Exploration, Environment, Analysis 4, 253-278.

Varela, D.E., Pride, C.J., Brzezinski, M.A., 2004. Biological fractionation of silicon isotopes in Southern Ocean surface waters. Glob. Biochem. Cycl. 18, GB1047, doi:10.1029/2003GB002140.

Viljoen, M.J., Viljoen, R.P., 1969. An introduction to the geology of the Barberton granite-greenstone terrain. Spec. Publ. Geol. Soc. S. Afr. 2, 9-28.

Walker, T.R., 1960. Carbonate replacement of detrital crystalline silicate minerals as a source of authigenic silica in sedimentary rocks. Geol. Soc. Am. Bull. 9, 145-152.

Wasserburg, G.J., Jacobsen, S.B., DePaolo, D.J., McCulloch, M.T., 1981. Precise determination of Sm/Nd ratios, Sm and Nd isotopic abundances in standard solutions. Geochim. Cosmochim. Acta 45, 2311-2323.

Weyer, S., Schwieters, J.B., 2003. High precision Fe isotope measurements with high mass resolution MC-ICPMS. Int. J. Mass Spectrom. 226, 355-368.

Winter, B.L., Knauth, L.P., 1992. Stable isotope geochemistry of cherts and carbonates from the 2.0-Ga Gunflint Iron Formation—implications for the depositional setting, and the effects of diagenesis and metamorphism. Precambrian Res. 59, 283-313.

Wyllie, P.J., 1977. Crustal anatexis: an experimental review. Tectonophysics 13, 41-71.

Young, E.D., Galy, A., Nagahara, H., 2002. Kinetic and equilibrium mass dependent isotope fractionation laws in nature and their geochemical and cosmochemical significance. Geochim. Cosmochim. Acta 66, 1095-1104.

Ziegler, K., Chadwick, O.A., White, A.F., Brzezinski, M.A., 2005a. δ^{30}Si systematics in a granitic saprolite, Puerto Rico. Geology 33, 817-820.

Ziegler, K., Chadwick, O.A., Brzezinski, M.A., Kelly, E.F., 2005b. Natural variations of δ^{30}Si ratios during progressive basalt weathering, Hawaiian Islands. Geochim. Cosmochim. Acta 69, 4597-4610.

Zinner, E., Tang, M., Anders, E., 1987. Large isotopic anomalies of Si, C, N and noble gases in interstellar silicon carbide from the Murray meteorite. Nature 330, 730-732.

Zinner, E., Tang, M., Anders, E., 1989. Interstellar SiC in the Murchison and Murray meteorites; isotopic composition of Ne, Xe, Si, C, and N. Geochim. Cosmochim. Acta 53, 3273-3290.

Acknowledgement

Related publications

Articles

Abraham, K., Opfergelt, S., Fripiat, F., Cavagna, A-J., de Jong, T.M.J., Foley, S.F., André, L., Cardinal, D., 2008. δ^{30}Si and δ^{29}Si determinations on BHVO-1 and BHVO-2 reference materials with a new configuration on a Nu Plasma Multi Collector ICP-MS. Geostandards and Geoanalytical Research, Issue 2, Vol 32, 193-202.

Abraham, K, Hofmann, A., Foley, S.F., Cardinal, D., Harris, C., Barth, M.G., André L. Coupled silicon-oxygen isotopic evidences for the origin of silicification in mafic volcanic rocks of the Barberton Greenstone Belt, South Africa. Submitted to Earth and Planetary Science Letters.

Abraham, K., Hofmann, A., Foley, S.F., Cardinal, D., André, L. Potential changes in the source of Granitoids in the Archaean: the Si isotope perspective. In preparation and submitted as extended Abstract (see below).

Conference proceedings

Abraham, K., Opfergelt, S., Cavagna, A-J., Planchon, F., Fripiat, F., André, L., de Jong, T.M.J., Cardinal, D., 2007. Solving interference on ^{30}Si with a Nu Plasma MC-ICP-MS. Geophysical Research Abstracts, Vol. 9, 08363; SRef-ID: 1607-7962/gra/EGU2007-A-08363; European Geoscience Union 2007.

Abraham, K., Opfergelt, S., Cardinal, D., Hofmann, A., Foley, S., André, L. 2007. Si isotopes as a clue for understanding Eoarchean sillicifications. 17th Annual V.M. Goldschmidt Conference (Cologne), Abstract: A3.

Abraham, K., Cardinal, D., Hofmann, A., Foley, S.F., Harris, C., André, L., 2009. The origin of Palaeoarchaean silicification inferred from coupled Si-O isotopes. 19th Annual V.M. Goldschmidt Conference (Davos), Abstract: A4.

Abraham, K., Hofmann, A., Foley, S.F., Cardinal, D., André, L. Potential changes in the source of Granitoids in the Archaean: the Si isotope perspective. 5th International Archaean Symposium, extended Abstract.